

D. First Addendum to Chapter XI (Addendum D). Lift forces on a cylindrical particle in plane Poiseuille flow of Newtonian and shear thinning fluids

Wang and Joseph [2003] have extended the analyses of the slip velocities and the lift on particles in plane Poiseuille flow from Newtonian fluids to shear thinning fluids. Explicit formulas for the lift force have been derived in terms of the slip velocity and angular slip velocity by correlating the data from numerical experiments.

▪ **The lift force on a particle in a shear flow**

Different analytical expressions for the lift force on a particle in a shear flow can be found in the literature. Auton [1987] gave a formula for the lift on a particle in an inviscid fluid in which uniform motion is perturbed by a weak shear. Bretherton [1962] found an expression for the lift per unit length on a cylinder (two-dimensional sphere) in an unbounded linear shear flow at small values of Reynolds number. Saffman [1965, 1968] gave an expression for the lift on a sphere in an unbounded linear shear flow. Saffman's equation is in the form of the slip velocity multiplied by a factor, which can be identified as a density multiplied by a circulation as in the famous formula $\rho U \Gamma$ for aerodynamic lift. A number of formulas like Saffman's exist and a review of such formulas can be found in McLaughlin [1991]. Formulas like Saffman's cannot explain the experiments by Segrè and Silberberg [1961, 1962]. They studied the migration of dilute suspensions of neutrally buoyant spheres in pipe flows and found the particles migrate away from both the wall and the centerline and accumulate at a radial position of about 0.6 times the pipe radius. There is nothing in formulas like Saffman's to account for the migration reversal near 0.6 of the radius.

The effect of the curvature of the undisturbed velocity profile was found to be important to understand the Segrè and Silberberg effect. Ho and Leal [1974] analyzed the motion of a neutrally buoyant particle in both simple shear flows and plane Poiseuille flows. They found that for Couette flow, the equilibrium position is the centerline; whereas for Poiseuille flow, it is 0.6 of the channel half-width from the centerline, which is in good agreement with Segrè and Silberberg.

Choi and Joseph [2001], Patankar, Huang, Ko and Joseph [2001] and Joseph and Ocando [2002] studied particle lift in plane Poiseuille flows by direct numerical simulation. They showed that multiple equilibrium states exist for heavy particles in plane Poiseuille flows. These equilibrium states can be stable or unstable and the distinction leads to division of the channel into alternating stability regions in the following order: wall – stable – unstable – stable – unstable – centerline (see Fig. B.3).

Joseph and Ocando [2002] analyzed the role of the slip velocity and the angular slip velocity on migration and lift. They showed that the discrepancy $\Omega_s - \Omega_{se}$, where Ω_{se} is the angular slip velocity at equilibrium position, is the quantity that changes sign across the equilibrium position. Thus, this discrepancy can be used to account for the migration from both the wall and the centerline to the equilibrium position.

Power law correlations are frequently observed in studies of solid-liquid flows. A famous example is the Richardson-Zaki correlation, which is obtained by processing the

data of fluidization experiments. The Richardson-Zaki correlation describes the complicated dynamics of fluidization by drag and is widely used for modeling the drag force on particles in solid-liquid mixtures. Correlations can also be drawn from numerical data; for example, power law correlations for single particle lift and for the bed expansion of many particles in slurries were obtained by processing simulation data (Patankar *et al.* [2001]; Choi and Joseph [2001]; Patankar, Ko, Choi, and Joseph [2001]). The prediction of power laws from numerical data suggests that the same type correlations could be obtained from experimental data as was done by Patankar, Joseph, Wang, Barree, Conway and Asadi [2002] and Wang, Joseph, Patankar, Conway and Barree [2003]. The existence of such power laws is an expression of self-similarity, which has not yet been predicted from analysis or physics. The flow of dispersed matter appears to obey those self-similar rules to a large degree (Barenblatt [1996]).

Most of studies on migration and lift are for Newtonian fluids. However, in many of the applications the fluids used are not Newtonian and shear thinning is the most important non-Newtonian property. Papers treating the migration of particles in shear flows of shear thinning fluids were done by Huang, Feng, Hu and Joseph [1997], Huang, Hu and Joseph [1998] and especially by Huang and Joseph [2000]. All these authors used the Carreau-Bird viscosity function (B.1) but only Huang and Joseph [2000] studied the case when there is shear thinning but no normal stresses.

In this addendum, we extend previous studies of lift on a cylindrical particle in plane Poiseuille flows of Newtonian fluids to shear thinning fluids. We show that the pattern of the stability regions in shear thinning fluids is the same as that in Newtonian fluids. The effects of shear thinning on the distribution of the stability regions are discussed. We verify that the angular slip velocity discrepancy changes sign across the equilibrium position for both neutrally buoyant particles and heavy particles. We derive power law correlations for the lift force in terms of the slip velocity and angular slip velocity discrepancy and demonstrate that these correlations can be made completely explicit.

▪ **Governing equations**

The 2D computational domain is shown in Fig. B.1. l and W are the length and width of the channel respectively, and d is the diameter of the particle. The simulation is performed with a periodic boundary condition in the x-direction. The solutions are essentially independent of the channel length l for sufficiently large l . The geometric parameters are $W/d = 12$, $l/d = 22$. The values of these parameters are taken from Patankar *at al.* [2001] where they justified that the solutions are essentially independent of the selected geometric parameters.

A constant pressure gradient $-\bar{p}$ is applied which gives rise to Poiseuille flow and the direction of the gravity force is perpendicular to the flow direction. In simulations in periodic domains the fluid pressure P is split as follows:

$$P = p + \rho_f \mathbf{g} \cdot \mathbf{x} - \bar{p} \mathbf{e}_x \cdot \mathbf{x} \Rightarrow -\nabla P = -\nabla p - \rho_f \mathbf{g} + \bar{p} \mathbf{e}_x$$

where \mathbf{e}_x is the unit vector in x-direction, \mathbf{x} is the position vector of any point in the domain and \mathbf{g} is the gravitational acceleration. p is periodic and solved in simulations.

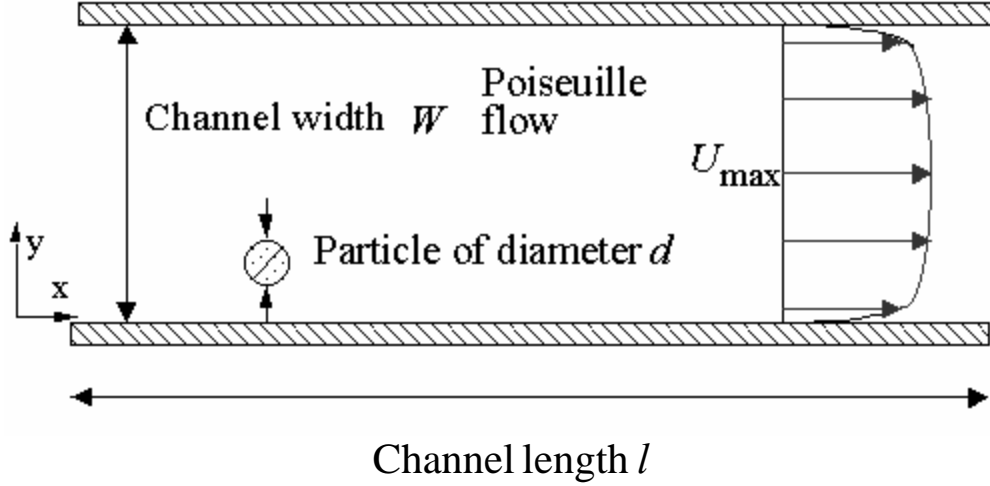


Figure B.1: The 2D rectangular computational domain.

We use the Carreau-Bird model for the shear thinning effects:

$$\frac{\eta - \eta_\infty}{\eta_0 - \eta_\infty} = [1 + (\lambda_3 \dot{\gamma})^2]^{\frac{n-1}{2}} \quad (\text{B.1})$$

where $\dot{\gamma}$ is the shear rate defined in terms of the second invariant of the rate of strain tensor \mathbf{D} . The shear thinning index n is in the range of 0 – 1 and $\eta_0, \eta_\infty, \lambda_3$ are prescribed parameters. We use $\eta_0 = 1.0 \text{ g} \cdot \text{cm}^{-1} \cdot \text{s}^{-1}$, $\eta_\infty / \eta_0 = 0.1$ and $\lambda_3 = 1.0 \text{ s}$ throughout our simulations.

We consider cylindrical particles of diameter d with the mass per unit length $m = \rho_p \pi d^2 / 4$ and the moment of inertia per unit length $I = \rho_p \pi d^4 / 32$. A dimensionless description of the governing equations can be constructed by introducing scales: the particle size d for length, V for velocity, d/V for time, V/d for angular velocity and $\eta_0 V / d$ for stress and pressure. We choose

$$V = \frac{\bar{p} W^2}{12 \eta_0} \quad (\text{B.2})$$

which is the average velocity of the undisturbed Poiseuille flow in Newtonian fluids. V can be related to the shear rate at the wall $\dot{\gamma}_w = \bar{p} W / (2 \eta_0)$:

$$V = 2 \dot{\gamma}_w \frac{W}{12} = 2 \dot{\gamma}_w d.$$

Hat variables are dimensionless in the following part. The dimensionless governing equations are

$$\hat{\nabla} \cdot \hat{\mathbf{u}} = 0, \quad R \left(\frac{\partial \hat{\mathbf{u}}}{\partial \hat{t}} + (\hat{\mathbf{u}} \cdot \hat{\nabla}) \hat{\mathbf{u}} \right) = -\hat{\nabla} \hat{p} + \frac{d}{W} \mathbf{e}_x + \hat{\nabla} \cdot [\Theta (\hat{\nabla} \hat{\mathbf{u}} + \hat{\nabla} \hat{\mathbf{u}}^T)] \quad (\text{B.3})$$

for the velocity $\hat{\mathbf{u}}$ and pressure \hat{p} of the fluid and

$$\frac{\rho_p}{\rho_f} R \frac{d \hat{\mathbf{U}}_p}{d \hat{t}} = -G \mathbf{e}_y + \frac{d}{W} \mathbf{e}_x + \frac{4}{\pi} \oint \left\{ -\hat{p} \mathbf{1} + \Theta (\hat{\nabla} \hat{\mathbf{u}} + \hat{\nabla} \hat{\mathbf{u}}^T) \right\} \cdot \mathbf{n} d \hat{\Gamma}, \quad (\text{B.4})$$

$$\frac{\rho_p}{\rho_f} R \frac{d\hat{\Omega}_p}{dt} = \frac{32}{\pi} \oint (\hat{\mathbf{x}} - \hat{\mathbf{X}}) \times \left([-\hat{p}\mathbf{1} + \Theta(\hat{\nabla}\hat{\mathbf{u}} + \hat{\nabla}\hat{\mathbf{u}}^T)] \cdot \mathbf{n} \right) d\hat{\Gamma} \quad (\text{B.5})$$

for the velocity $\hat{\mathbf{U}}_p$ and angular velocity $\hat{\Omega}_p$ of the particle whose center of mass has the coordinate $\hat{\mathbf{X}}$. In equations (B.3) – (B.5) we use

$$R = \frac{\rho_f V d}{\eta_0}, \quad G = \frac{(\rho_p - \rho_f) g d^2}{\eta_0 V} \quad \text{and} \quad \Theta = \frac{\eta_\infty}{\eta_0} + \left(1 - \frac{\eta_\infty}{\eta_0}\right) \left[1 + (2\lambda_3 \dot{\gamma}_w)^2 \dot{\gamma}^2\right]^{\frac{n-1}{2}}.$$

The no-slip condition is imposed on the particle boundaries:

$$\hat{\mathbf{u}} = \hat{\mathbf{U}}_p + \hat{\Omega}_p \times (\hat{\mathbf{x}} - \hat{\mathbf{X}}). \quad (\text{B.6})$$

Following is a list of the dimensionless parameters:

$$\begin{aligned} \rho_p / \rho_f, & \quad \text{density ratio;} \\ d/W, & \quad \text{aspect ratio;} \\ \eta_\infty / \eta_0, & \quad \text{viscosity ratio;} \\ \Lambda^2 = (2\lambda_3 \dot{\gamma}_w)^2, & \quad \text{shear rate parameter;} \\ n, & \quad \text{shear thinning index;} \\ R = \frac{\rho_f V d}{\eta_0} = \frac{2\rho_f \dot{\gamma}_w d^2}{\eta_0} = \frac{\rho_f W d^2 \bar{p}}{\eta_0^2}, & \quad \text{Reynolds number;} \\ G = \frac{(\rho_p - \rho_f) g d^2}{\eta_0 V} = \frac{d}{W} \frac{(\rho_p - \rho_f) g}{\bar{p}}, & \quad \text{gravity parameter.} \end{aligned}$$

Instead of G , we use the gravity Reynolds number $R_G = R \cdot G = \frac{\rho_f (\rho_p - \rho_f) g d^3}{\eta_0^2}$.

W/d and η_∞ / η_0 are constant in our simulations; λ_3 is also constant, so Λ^2 would not provide more information. Thus ρ_p / ρ_f , R , n and R_G are the four dimensionless parameters at play. The Reynolds number R and shear thinning index n together, characterize an undisturbed Poiseuille flow. We define an average Reynolds number $\bar{R} = \rho_f u_0 d / \eta_0$ where u_0 is the average velocity of the undisturbed Poiseuille flow. In table B.1, we list the average Reynolds numbers \bar{R} for flows characterized by (n, R) pairs. \bar{R} increases significantly with n decreasing at a fixed R .

n	R	\bar{R}
1.0	20	20.00
0.9	20	24.28
0.8	20	30.48
0.7	20	39.70
1.0	40	40.00
0.9	40	51.84
0.8	40	69.97
0.7	40	97.89
1.0	80	80.00

0.9	80	110.72
0.8	80	160.06
0.7	80	237.60

Table B.1: Average Reynolds numbers \bar{R} for flows characterized by (n, R) pairs.

▪ Undisturbed flow

We refer Poiseuille flow without particles as undisturbed flow. The dimensionless momentum equation in the x-direction for the undisturbed flow is

$$-\frac{d}{W} = \frac{d}{d\hat{y}} \left(\Theta \frac{d\hat{u}}{d\hat{y}} \right). \quad (\text{B.7})$$

An analytical solution for the Poiseuille flow of a Carreau-Bird fluid is not known. However, a numerical solution can be achieved by an iterative method. First $\hat{\gamma}^0(\hat{y})$ is assumed to be the shear rate of the Poiseuille flow of a Newtonian fluid and $\Theta(\hat{\gamma}^0(\hat{y}))$ is obtained. A new shear rate profile $\hat{\gamma}^1(\hat{y})$ is then computed and the steps are repeated until $\hat{\gamma}(\hat{y})$ converges. The velocity $\hat{u}(\hat{y})$ is obtained by integrating the shear rate.

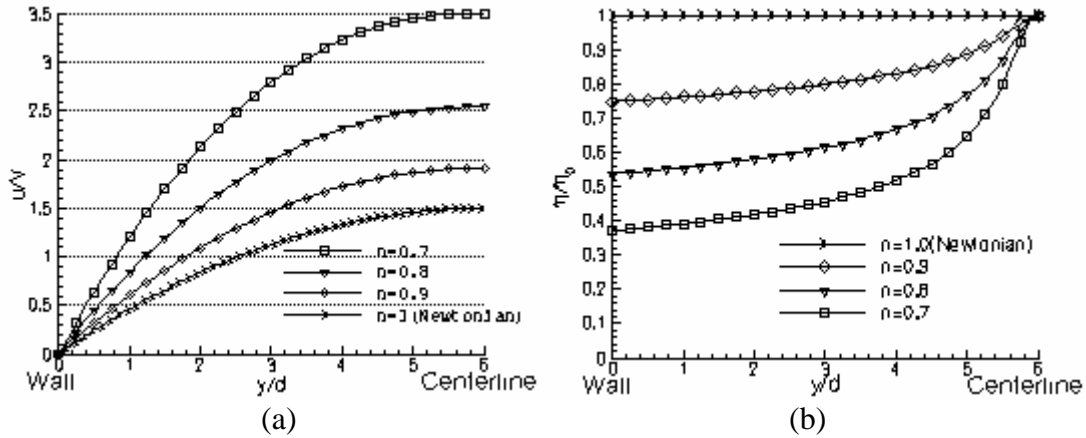


Figure B.2. The dimensionless velocity $u/V = u/(2\dot{\gamma}_w d)$ profiles (a) and the dimensionless viscosity η/η_0 profiles (b) of the Poiseuille flows with $R = 40$ and $n = 0.7, 0.8, 0.9$ and 1.0 (Newtonian fluid). Due to the symmetry of the profiles, only a half of the channel is plotted.

The velocity and viscosity profiles of the Poiseuille flows with $R = 40$ and $n = 0.7, 0.8, 0.9$, and 1.0 (Newtonian fluid) are plotted in Fig. B.2. The velocity profiles are qualitatively similar to the parabolic profiles seen in flows of Newtonian fluids. At a fixed R , the maximum velocity in the channel increases significantly as n decreases. The viscosity profiles have their minimums at the wall (corresponding to the maximum $\dot{\gamma}$), and their maximums at the centerline (corresponding to zero $\dot{\gamma}$).

▪ Stable and unstable equilibrium regions

An equilibrium is achieved for a freely moving and rotating cylindrical particle with a given density in a Poiseuille flow when the particle migrates to a position y_e of steady

rectilinear motion in which the acceleration and angular acceleration vanish and the hydrodynamic lift just balances the buoyant weight. Two types of simulations are performed, **unconstrained simulation** and **constrained simulation**. In unconstrained simulations, a particle is allowed to move and rotate freely to migrate to its equilibrium position. The initial translational and angular velocities of the particle are prescribed and initial-value problems are solved to obtain the equilibrium state. In constrained simulations, the position of the particle in the y-direction y_p is fixed and the particle is allowed to move in x-direction and rotate. The solution of the flow evolves dynamically to a steady state at which the lift force per unit length L on the particle is computed. Such a steady state will be an equilibrium at $y=y_p$ if the density of the particle is selected so that L just balances the buoyant weight per unit length, satisfying:

$$\hat{L} \stackrel{def}{=} \frac{L}{\rho_f g \pi d^2 / 4} = \frac{\rho_p}{\rho_f} - 1 \tag{B.8}$$

where \hat{L} is a dimensionless lift force and represents the ratio between the hydrodynamic lift force L and the buoyant force $\rho_f g \pi d^2 / 4$.

From the steady state values which evolve in constrained simulations, we are able to obtain \hat{L} on the particle at any position y/d in the channel. We can divide the curve of \hat{L} vs. y/d from the wall to the centerline into four branches by three “turning points” (see Fig. B.3). The “turning point” is defined as the position where the slope of the \hat{L} vs. y/d curve is zero. On the first and third branches of steady solutions, the slope of \hat{L} vs. y/d curve is negative, and the equilibrium points on these branches are stable. On the second and fourth branches of steady solutions, the slope of \hat{L} vs. y/d curve is positive, and the equilibrium points are unstable. We will indicate the unstable branches by dotted lines in the figures.

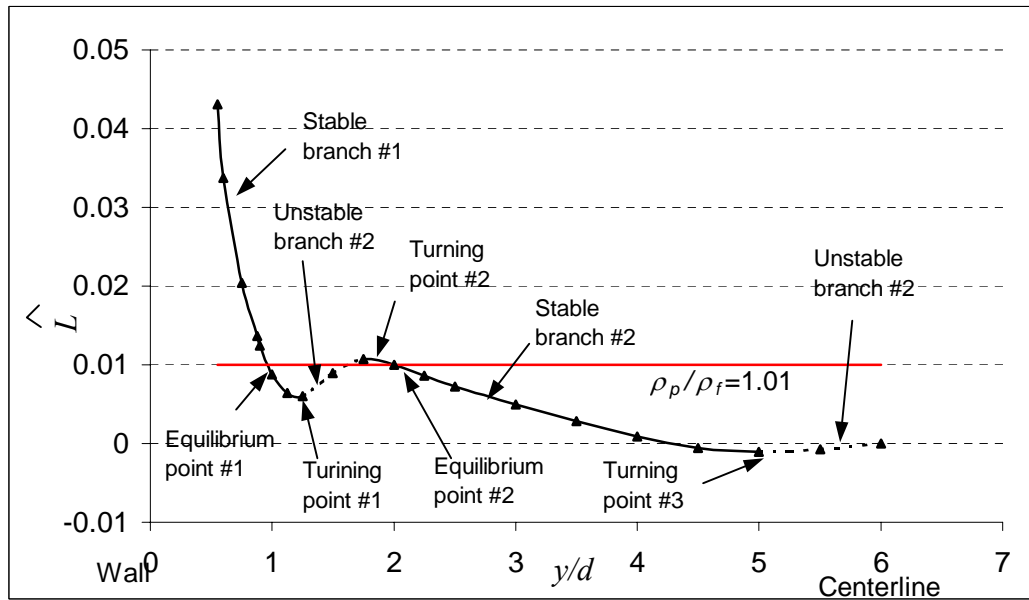


Figure B.3. A plot of \hat{L} vs. y/d for a flow with $n=0.8$ and $R = 20$ from constrained simulations. The stable and unstable branches and three turning points are illustrated.

Unstable branches are indicated by dotted lines. Two stable equilibrium points for a particle with $\rho_p/\rho_f = 1.01$ are shown.

From the \hat{L} vs. y/d curve, the equilibrium position for a particle with a certain ρ_p can be determined. The lift force required to balance the buoyant weight of a particle can be computed from (B.8). If we draw a line on which \hat{L} equals to this required lift force, the points of intersections between this line and the \hat{L} vs. y/d curve are the equilibrium points for this particle. For heavier-than-fluid particles with intermediate densities, there exist multiple stable equilibrium positions from the wall to the centerline (see Fig. B.3 where two stable equilibrium points for a particle with $\rho_p/\rho_f = 1.01$ are shown). However, for a neutrally buoyant particle ($\hat{L} = 0$), only one stable equilibrium point exists from the wall to the centerline.

Ho and Leal [1974] studied the equilibrium position of a neutrally buoyant freely moving and rotating sphere between plane bounding walls. They assumed that the walls were so closely spaced that the lift could be obtained by perturbing Stokes flow with inertia. They calculated dimensionless lateral force vs. lateral position curves (equivalent to our \hat{L} vs. y/d curve) for simple shear flow and 2D Poiseuille flow which are shown in Fig. B.4. Comparing the dashed line in Fig. B.4 which is for 2D Poiseuille flow and the \hat{L} vs. y/d curve in Fig. B.3, one can see that both of the two plots imply the centerline is an unstable equilibrium position. However, the dashed line in Fig. B.4 indicates that there are two branches from the wall to the centerline: wall – stable – unstable – centerline, whereas four branches exist according to Fig. B.3. Ho and Leal only considered neutrally buoyant particle and did not include the gravity term in the governing equation used in their calculation. The frame of their work did not enable them to study the multi-equilibrium positions of heavier-than-fluid particles. The results shown in Figs. B.3 and B.4 are not strictly comparable; Ho and Leal studied spheres (3D) between plane walls at indefinitely small R whereas our calculation is for 2D particles at much higher Reynolds numbers.

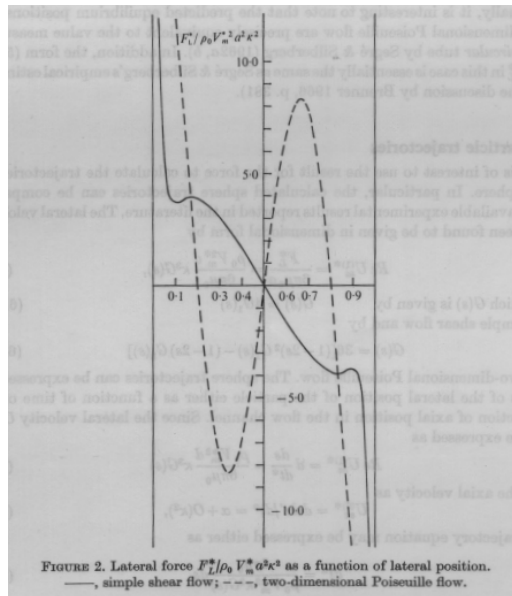


Figure B.4. Lateral force as a function of lateral position, both in dimensionless form. —, simple shear flow; - - -, 2D Poiseuille flow. (Adapted from Ho and Leal 1974)

The distribution of the equilibrium branches is affected by the shear thinning effects. The \hat{L} vs. y/d curves are computed for the flows with $R = 20, 40$ and 80 and $n=0.7, 0.8, 0.9$ and 1.0 (Newtonian fluid). Two groups of typical curves are plotted in Figs. B.5 and B.6.

We find that when the shear thinning effects become stronger, the stable branch near the wall decreases in size; the unstable branch near the wall moves closer to the wall; the stable branch near the centerline increases in size; the unstable branch at the centerline decreases in size. The shrinkage of the unstable branch at the centerline implies that a particle could be lifted to an equilibrium position closer to the centerline if shear thinning effects are stronger. A closer equilibrium position to the centerline could also be achieved when pressure gradient is higher, as shown first in Patankar *et al.* [2001] and confirmed in our simulations. It seems that higher pressure gradient and stronger shear thinning both lead to stronger inertia effects and could lift a particle closer to the centerline. In the range of the Reynolds number and shear thinning index we simulated, the unstable branch at the centerline never vanishes. Patankar *et al.* [2001] reported that in 2D Poiseuille flows of an Oldroyd-B fluid at high Deborah number, the centerline can be a stable equilibrium position and the Segrè and Silberberg effect does not occur. We did not observe the same phenomenon in shear thinning fluids.

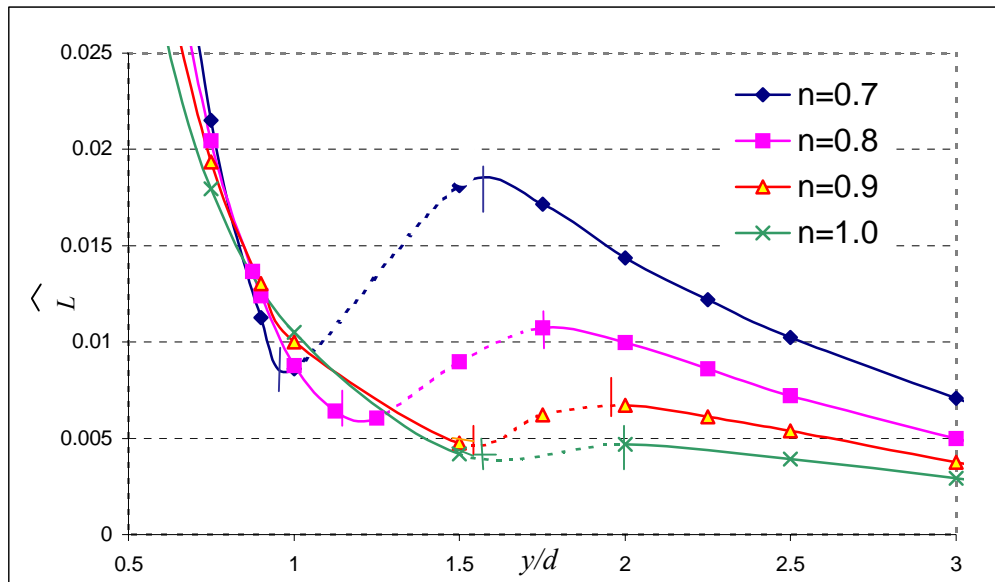


Figure B.5. Near-the-wall part of \hat{L} vs. y/d curves of the Poiseuille flows with $R = 20$ and $n=0.7, 0.8, 0.9$ and 1.0 (Newtonian fluid). The unstable branches are indicated by dotted lines and their starting and ending points are marked by pairs of short vertical lines. With the shear index n decreasing, the stable branch near the wall decreases in size and the unstable branch near the wall moves closer to the wall.

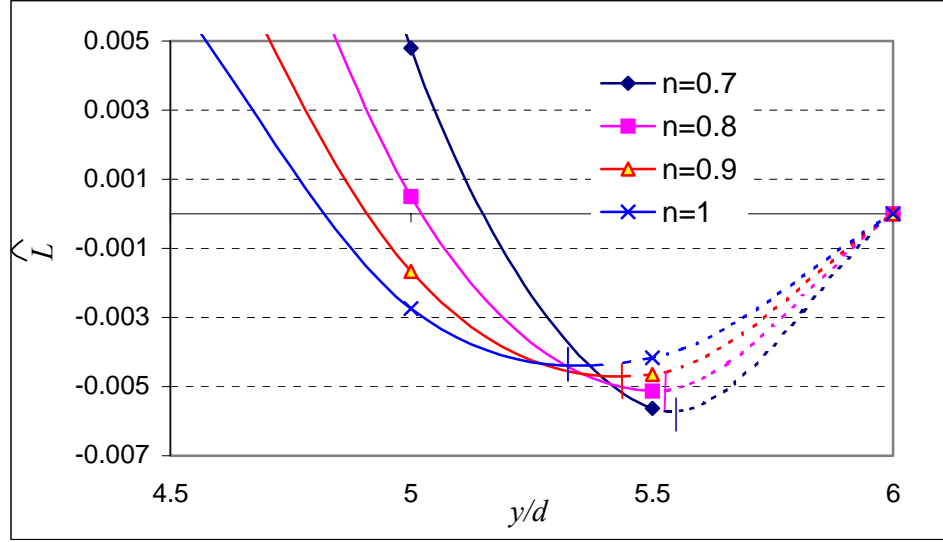


Figure B.6. Near-the-centerline part of \hat{L} vs. y/d curves of the Poiseuille flows with $R = 80$ and $n=0.7, 0.8, 0.9$ and 1.0 (Newtonian fluid). The unstable branches are indicated by dotted lines and short vertical lines are used to mark the starting points of these unstable branches. With the shear index n decreasing, the unstable branch near the centerline decreases in size.

▪ Angular slip velocity discrepancy and net lift force

Joseph and Ocando [2002] studied slip velocities and particle lift in 2D Poiseuille flows of Newtonian fluids. The slip velocity is $U_s = U_f - U_p$ and the angular slip velocity is $\Omega_s = \Omega_p - \Omega_f$, where U_f and $\Omega_f = -\dot{\gamma}/2$ are the translational velocity and angular velocity of the undisturbed Poiseuille flow at the position of the particle and $\dot{\gamma}$ is the local shear rate. The net lift force is:

$$L_n = L - (\rho_p - \rho_f)\pi d^2 g / 4 \Rightarrow \hat{L}_n = \hat{L} - \left(\frac{\rho_p}{\rho_f} - 1\right). \quad (\text{B.9})$$

Joseph and Ocando found that the angular slip velocity discrepancy $\Omega_s - \Omega_{se}$, where Ω_{se} is the angular slip velocity at equilibrium, changes sign across the equilibrium position. Furthermore, they showed that across a stable equilibrium position, the net lift force L_n has the same sign as the discrepancy $\Omega_s - \Omega_{se}$; whereas across an unstable equilibrium position, the net lift force L_n has the opposite sign as the discrepancy $\Omega_s - \Omega_{se}$. In this section, we verify that these conclusions hold in shear thinning fluids using constrained simulations.

We fix a particle at positions slightly above ($y_p > y_e$) and below ($y_p < y_e$) its equilibrium positions and compute the steady state lift force and angular slip velocity Ω_s . For a neutrally buoyant particle, both stable and unstable equilibrium positions are investigated; for a heavy particle, both of its two stable equilibrium positions are investigated. Table B.2 shows the results for a neutrally buoyant particle and table B.3 shows those for a heavy particle.

y_e/d	4.35		6.0	
$\Omega_{se}/(2\dot{\gamma}_w)$	1.25×10^{-2}		0.0	
fixed y_p/d	4.33	4.36	5.95	6.05
$L/(\rho_p g \pi d^2/4)$	8.2×10^{-5}	-1.4×10^{-5}	-7.9×10^{-5}	7.7×10^{-5}
$(\Omega_s - \Omega_{se})/(2\dot{\gamma}_w)$	2.5×10^{-6}	-4.5×10^{-4}	5.8×10^{-5}	-5.3×10^{-5}

Table B.2. The steady state values of L and $\Omega_s - \Omega_{se}$ in dimensionless form at fixed positions slightly above ($y_p > y_e$) and below ($y_p < y_e$) the equilibrium positions of a neutrally buoyant particle in the flow with $n=0.7$ and $R=20$. The stable equilibrium position is $y_e/d=4.35$ with $\Omega_{se}/(2\dot{\gamma}_w)=1.25 \times 10^{-2}$. For the particle fixed below ($y_p/d = 4.33$), $\Omega_s - \Omega_{se} > 0$ and $L > 0$; for the particle fixed above ($y_p/d = 4.36$), $\Omega_s - \Omega_{se} < 0$ and $L < 0$. The unstable equilibrium position is the centerline with $y_e/d=6.0$ and $\Omega_{se}/(2\dot{\gamma}_w)=0$. For the particle fixed below ($y_p/d = 5.95$), $\Omega_s - \Omega_{se} > 0$ but $L < 0$; for the particle fixed above ($y_p/d = 6.05$), $\Omega_s - \Omega_{se} < 0$ but $L > 0$.

y_e/d	0.918		2.26	
$\Omega_{se}/(2\dot{\gamma}_w)$	7.16×10^{-2}		4.95×10^{-2}	
fixed y_p/d	0.9	1.0	2.25	2.5
$L_n/(\rho_p g \pi d^2/4)$	1.88×10^{-3}	-6.4×10^{-3}	2.58×10^{-4}	-3.26×10^{-3}
$(\Omega_s - \Omega_{se})/(2\dot{\gamma}_w)$	4.88×10^{-4}	-1.44×10^{-3}	1.50×10^{-5}	-5.50×10^{-3}

Table B.3. The steady state values of the net lift force L_n and $\Omega_s - \Omega_{se}$ in dimensionless form at fixed positions above ($y_p > y_e$) and below ($y_p < y_e$) the equilibrium positions of a heavy particle ($\rho_p/\rho_f=1.024$) in the flow with $n=0.9$ and $R=40$. Two stable equilibrium positions exist: $y_e/d=0.918$ with $\Omega_{se}/(2\dot{\gamma}_w)=7.16 \times 10^{-2}$ and $y_e/d=2.26$ with $\Omega_{se}/(2\dot{\gamma}_w)=4.95 \times 10^{-2}$. For either one of the equilibrium positions, $\Omega_s - \Omega_{se} > 0$ and $L_n > 0$ when the particle is fixed below; $\Omega_s - \Omega_{se} < 0$ and $L_n < 0$ when the particle is fixed above.

Table B.2 and B.3 verify the conclusions about the discrepancy $\Omega_s - \Omega_{se}$, summarized as following: $\Omega_s - \Omega_{se} < 0$ when $y_p > y_e$; $\Omega_s - \Omega_{se} > 0$ when $y_p < y_e$. With a stable equilibrium as the reference state, negative $\Omega_s - \Omega_{se}$ leads to negative L_n , positive $\Omega_s - \Omega_{se}$ leads to positive L_n ; with an unstable equilibrium position as the reference state, negative $\Omega_s - \Omega_{se}$ leads to positive L_n , positive $\Omega_s - \Omega_{se}$ leads to negative L_n . ($L_n=L$ in the case of a neutrally buoyant particle.) These conclusions are for the lift force and slip velocity in steady flows and do not hold generally for a free particle with accelerations.

▪ Lift correlations

Motivated by the conclusion that $\Omega_s - \Omega_{se}$ has the same sign as L_n across a stable equilibrium position, we seek the correlations between L_n and the product $U_s(\Omega_s - \Omega_{se})$. Such correlations may be constructed by analogy with the classical lift formula $L = C_U \Gamma$ of aerodynamics. The proper analogs of U and Γ in the present context are U_s and $\Omega_s - \Omega_{se}$ as first proposed in Joseph and Ocando [2002]. We proceed as follows to obtain the correlations. First we compute L , U_s and Ω_s as functions of y by constrained simulations in a steady flow with Reynolds number R and shear thinning index n . Then we correlate dimensionless parameters based on L and $U_s(\Omega_s - \Omega_{se})$ to power law formulas. These steps

are repeated for different flows identified by (R, n) pairs and lead to correlations for each flow. The coefficients in such correlations are functions of R and n which can be obtained by data fitting analyses. Finally we obtain correlations between dimensionless L and $U_s(\Omega_s - \Omega_{se})$ with coefficients expressed as functions of R and n .

Figure B.7 shows the relative values of L , U_s and Ω_s in the steady flow with $R=20$ and $n=0.9$.

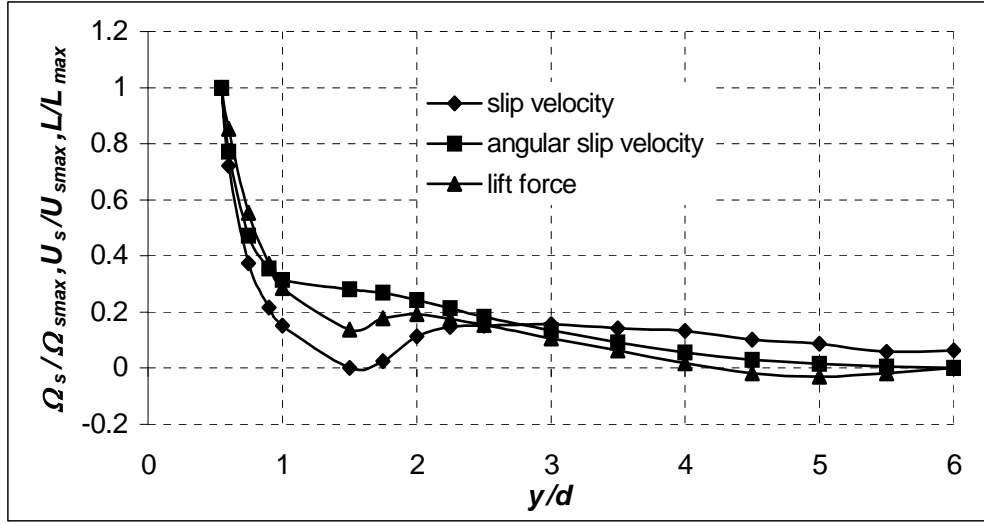


Figure B.7. The relative values of L , U_s and Ω_s in the steady flow with $R=20$ and $n=0.9$.

Local dimensionless parameters are used to express the correlations. The local dimensionless net force is:

$$\lambda(y) = \frac{4\rho_f d [L(y) - (\rho_p - \rho_f)g\pi d^2 / 4]}{\pi\eta(y)^2} = \frac{4\rho_f d}{\pi\eta(y)^2} L_n(y). \quad (\text{B.10})$$

Two local Reynolds numbers are based on U_s and $\Omega_s - \Omega_{se}$ respectively:

$$R_U(y) = \frac{\rho_f U_s(y) d}{\eta(y)}, \quad R_\Omega(y) = \frac{\rho_f [\Omega_s(y) - \Omega_{se}] d^2}{\eta(y)}. \quad (\text{B.11})$$

The product of R_U and R_Ω is defined as F :

$$F(y) = R_U \cdot R_\Omega = \frac{\rho_f^2 U_s(y) [\Omega_s(y) - \Omega_{se}] d^3}{\eta(y)^2}. \quad (\text{B.12})$$

To compute $F(y)$ from (B.12), it is necessary to specify the equilibrium angular slip velocity $\Omega_{se} = \Omega_s(y_e)$ where y_e is the position at which the lift equals the buoyant weight. The \hat{L} vs. y/d curve (Fig. B.3) shows that each and every value of y/d on the stable branches is a possible equilibrium position ($y=y_e$) for some particle ρ_p . You may cover the range of possible y_e by varying the weight of the particle. Once y_e is selected, Ω_{se} is given as $\Omega_s(y_e)$. The dependence of Ω_{se} and L_n on ρ_p makes the correlations between $\lambda(y)$ and $F(y)$ particle-density dependent. However, the steady state values of L do not depend

on particle density. If we derive the correlations between $\lambda(y)$ and $F(y)$ for one ρ_p , the lift force is essentially obtained and can be applied to particles with different densities. We present the correlations with the single equilibrium position of a neutrally buoyant particle as the reference. There are two advantages of this choice: the complexity of multi-equilibrium positions of a heavy particle is avoided; the correlations are in simple forms which are a power law for the stable branch near the wall and a linear relation for the stable branch near the centerline.

For a neutrally buoyant particle, a single equilibrium position exists at $y = y_e^N$ (the superscript is for “neutral”) with $L(y_e^N) = 0$ and $\Omega_s(y_e^N) = \Omega_{se}^N$. Thus the dimensionless parameters have the following form:

$$\lambda(y) = \frac{4\rho_f dL(y)}{\pi\eta(y)^2} \quad \text{and} \quad F(y) = \frac{\rho_f^2 U_s(y) [\Omega_s(y) - \Omega_{se}^N] d^3}{\eta(y)^2}.$$

The correlations are in the following form,

$$\lambda(R, n, y/d) = a(R, n) F(R, n, y/d)^{m(R, n)} \quad \text{on the stable branch near the wall;} \quad (\text{B.13})$$

$$\lambda(R, n, y/d) = k(R, n) F(R, n, y/d) \quad \text{on the stable branch near the centerline.} \quad (\text{B.14})$$

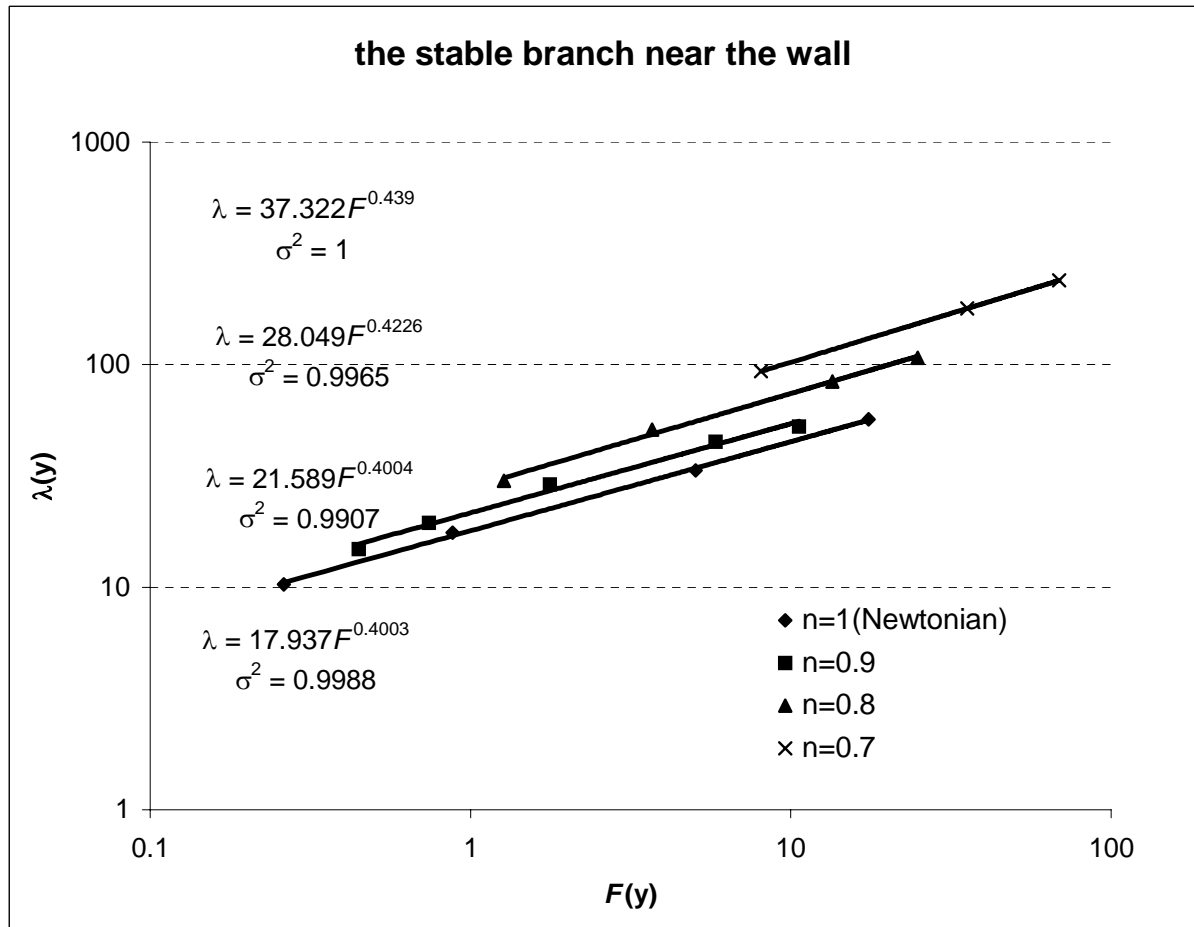


Figure B.8. The power law correlations between $\lambda(y)$ and $F(y)$ on the stable branch near the wall for the flows with $R=20$ and $n=0.7, 0.8, 0.9$ and 1 (Newtonian fluid).

We obtain the correlations for flows with $n=0.7, 0.8, 0.9$ and 1.0 (Newtonian fluid). In Fig. B.8, the correlations on the stable branch near the wall are plotted for the flows with $R=20$. The power law correlations along with the correlation coefficients σ^2 are shown in the figure. In Fig. B.9, two examples of the linear correlation between $\lambda(y)$ and $F(y)$ on the stable branch near the centerline are plotted for the flows with ($R=20, n=0.7$) and ($R=80, n=0.8$). It can be seen that our correlations describe the data faithfully.

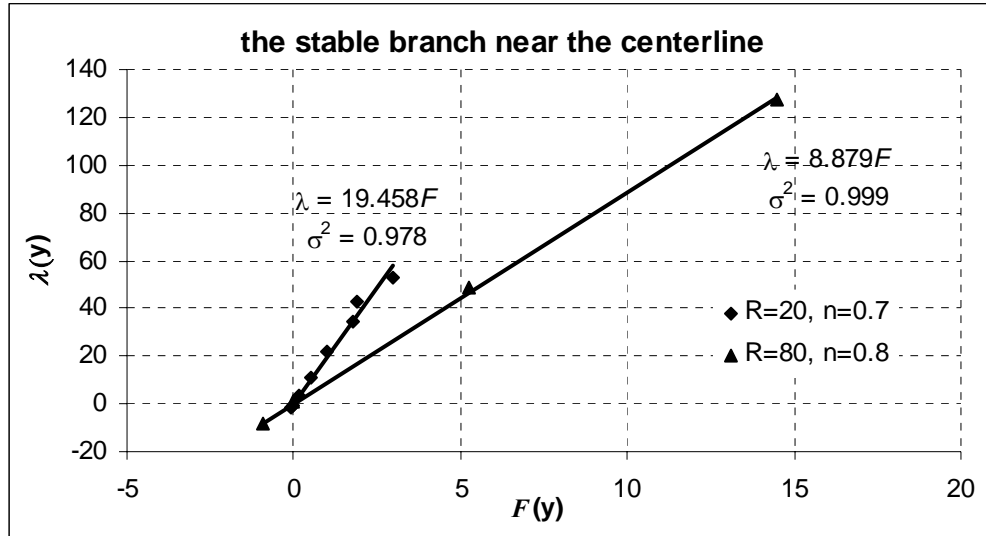


Figure B.9. The linear correlation between $\lambda(y)$ and $F(y)$ on the stable branch near the centerline for the flows with ($R=20, n=0.7$) and ($R=80, n=0.8$).

The prefactor a , the exponent m and the slope k in (B.13) and (B.14) are functions of R and n . In table B.4, the coefficients a , k and m are listed along with R , n , and the average Reynolds number \bar{R} which can be viewed roughly as a parameter for the combined effects of R and n . Coefficients a , m and k are also plotted against \bar{R} in Figs. B.10-B.12.

n	R	\bar{R}	a	m	k
1	20	20	17.937	0.4003	53.171
0.9	20	24.28	21.589	0.4004	34.685
0.8	20	30.48	28.049	0.423	27.348
0.7	20	39.7	37.322	0.439	19.458
1	40	40.0	27.288	0.410	30.739
0.9	40	51.84	36.38	0.427	25.591
0.8	40	69.97	40.808	0.481	22.166
0.7	40	97.89	9.664	0.774	11.759
1	80	80.0	38.009	0.448	24.35
0.9	80	110.72	53.729	0.450	21.066
0.8	80	160.06	9.570	0.779	8.879
0.7	80	237.6	2.710	0.898	7.698
1	120	120	43.83	0.472	21.54
1	160	160	41.48	0.496	16.39

Table B.4. The prefactor a , the exponent m and the slope k as functions of the shear index n and the Reynolds number R .

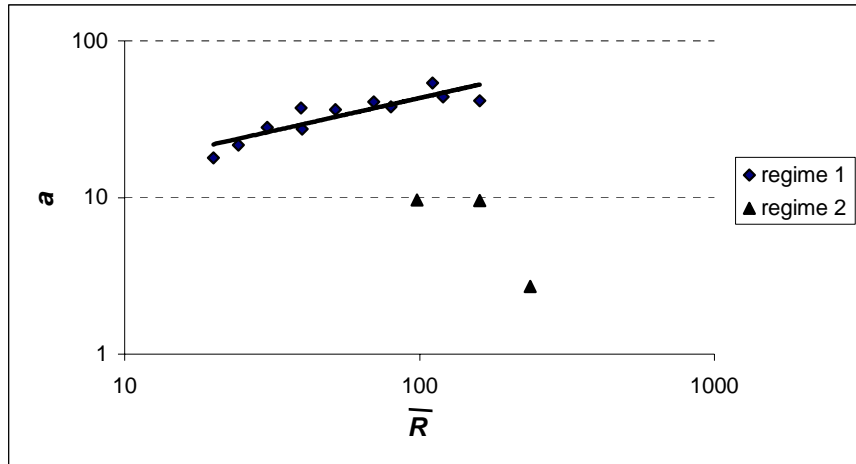


Figure B.10. The prefactor a vs. the average Reynolds number \bar{R} .

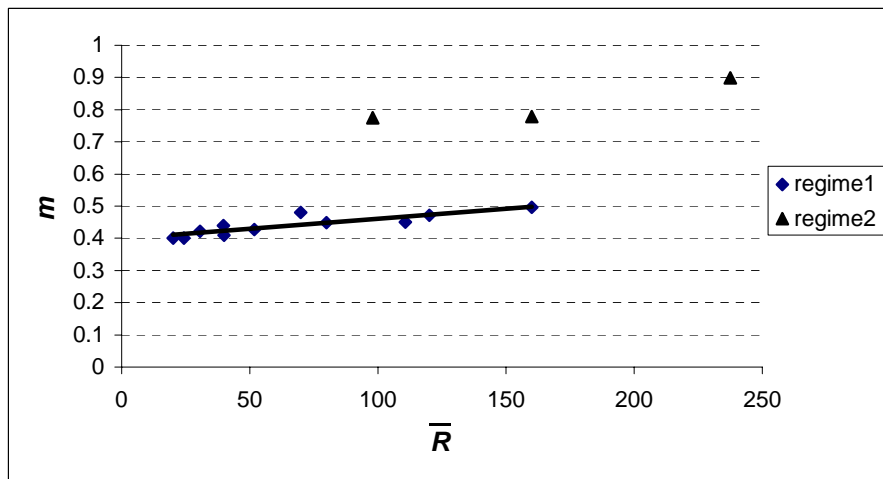


Figure B.11. The exponent m vs. the average Reynolds number \bar{R} .

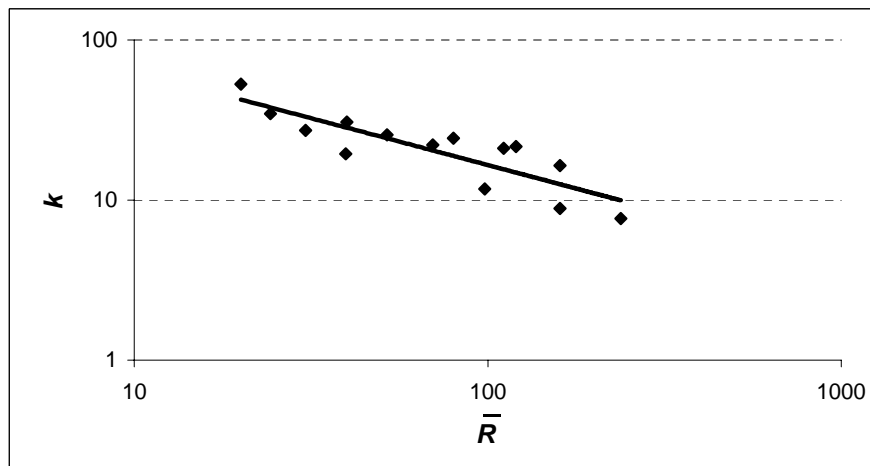


Figure B.12. The slope k vs. the average Reynolds number \bar{R} .

Figures B.10 and B.11 reveal that the power law correlation (B.13) on the stable branch near the wall has two regimes. Flows of Newtonian fluids and weak shear thinning flows fall into regime1 where the prefactor a increases with \bar{R} increasing and the exponent m is in the range of 0.4 – 0.5. Regime2 has three flows ($n=0.7$, $R=40$), ($n=0.7$, $R=80$) and ($n=0.8$, $R=80$) and can be identified as a strong shear thinning regime where the prefactor a decreases with \bar{R} increasing and the exponent m is in the range of 0.77 – 0.9. From the values of the exponent m , we can tell that in regime2 the dependence of the lift force on the product of slip velocities is stronger than that in regime1. It is noted that the two flows ($n=1.0$, $R=160$) and ($n=0.8$, $R=80$) have very close values of \bar{R} but substantially different coefficients a , m and k (see table B.4); this indicates that particle lift in strong shear thinning flows is different with that in flows of Newtonian fluids at high Reynolds number. Figure B.12 exhibits one regime of the linear correlation (B.14) where the slope k decreases with \bar{R} increasing. Figures B.10-B.12 also suggest that power law or linear functions of \bar{R} could be used to approximate the prefactor a and the exponent m in regime1 and the slope k . However, the error of such approximations would be considerable. The reason of such error is that a , k , and m depend on both n and R ; one single parameter \bar{R} cannot fully describe the dependence of the coefficients on the flow.

We cannot fully determine the coefficients a , m and k as functions of R and n because of insufficient data. If we focus on flows of Newtonian fluids ($n=1$), R is the only active parameter and we expect to get satisfactory $a(R)$, $k(R)$ and $m(R)$ approximations by data fitting analyses. The coefficients a , k , and m in flows of Newtonian fluids are listed as functions of R in table B.5.

R	a	m	k
20	17.94	0.400	53.17
40	27.29	0.410	30.74
80	38.01	0.448	24.35
120	43.83	0.472	21.54
160	41.48	0.496	16.39

Table B.5. The prefactor a , the exponent m and the slope k as functions of the Reynolds number R for flows of Newtonian fluids. Data are consistent with those in table B.4.

Data fitting analyses yield:

$$a = 5.34R^{0.428}, \quad \sigma^2=0.94; \quad (\text{B.15})$$

$$m = 0.0007R + 0.386, \quad \sigma^2=0.99; \quad (\text{B.16})$$

$$k = 232.5R^{-0.515}, \quad \sigma^2=0.96. \quad (\text{B.17})$$

Inserting (B.15), (B.16) and (B.17) into the correlations (B.13) and (B.14), we obtain correlations which apply to flows of Newtonian fluids with a Reynolds number in the range of 20 – 160.

$$\begin{cases} \lambda(\mathbf{y}) = 5.34R^{0.428} F(\mathbf{y})^{(0.0007R+0.386)} & \text{on the stable branch near the wall;} & (\text{B.18}) \\ \lambda(\mathbf{y}) = 232.5R^{-0.515} F(\mathbf{y}) & \text{on the stable branch near the centerline.} & (\text{B.19}) \end{cases}$$

Replacing $\lambda(y)$ and $F(y)$ in (B.18) and (B.19) with their dimensional forms and rearrange, we obtain the equations in the following form

$$\left\{ \begin{array}{l} L = 4.20R^{0.428} \rho_f^{0.0014R - 0.227} \eta_0^{-0.0014R + 1.227} \left[U_s (\Omega_s - \Omega_{se}^N) \right]^{0.0007R + 0.386} d^{0.0021R + 0.159} \\ \qquad \qquad \qquad \text{on the stable branch near the wall;} \end{array} \right. \quad (\text{B.20})$$

$$\left\{ \begin{array}{l} L = 182.6R^{-0.515} \rho_f U_s (\Omega_s - \Omega_{se}^N) d^2 \\ \qquad \qquad \qquad \text{on the stable branch near the centerline.} \end{array} \right. \quad (\text{B.21})$$

Note that for Newtonian fluids, $\eta(y)$ reduces to η_0 .

Although correlations (B.20) and (B.21) are derived using the equilibrium of a neutrally buoyant particle as the reference, they can be applied to heavy particles. To demonstrate this, we first obtain U_s and Ω_s for heavy particles at their equilibrium states from unconstrained simulations; these values are then inserted into (B.20) and (B.21) to calculate the lift forces which should match the values of the buoyant weight of the heavy particles. Two examples are shown in table B.6: a particle with $\rho_p/\rho_f=1.016$ in a flow with $R=40$ and a particle with $\rho_p/\rho_f=1.045$ in a flow with $R=80$. In both cases two stable equilibrium positions exist. The lift force for y_e close to the wall is computed using (B.20) and the lift force for y_e close to the centerline is computed using (B.21). It can be seen that the computed dimensionless lift forces are close to the values of the dimensionless buoyant weight (ρ_p/ρ_f-1) of the particles. In this way we demonstrate that the correlations derived for neutrally buoyant particles can be applied to heavy particles.

R	Ω_{se}^N (s ⁻¹)	ρ_p/ρ_f	ρ_p/ρ_f-1	y_e/d	Ω_s (s ⁻¹)	U_s (cm/s)	\hat{L}
40	0.2094	1.016	0.016	1.093	1.5765	0.2869	0.018
				2.377	1.1837	0.5393	0.014
80	0.4255	1.045	0.045	0.9476	4.332	0.4526	0.046
				2.705	2.737	0.8241	0.047

Table B.6. Computation of the lift forces on heavy particles using the correlations (B.20) and (B.21). The computed dimensionless lift forces are close to the values of the dimensionless buoyant weight (ρ_p/ρ_f-1) of the particles.

Correlations (B.20) and (B.21) apply to 2D motion of a particle in a Poiseuille flow. They may be compared to well-known lift expressions for a particle in a linear shear flow with shear rate $\dot{\gamma}$. The comparisons are at best tentative because the linear shear neglects the effects of shear gradients and because the lift expressions in linear shear flows are for indefinitely small Reynolds number perturbing Stokes flow on an unbounded domain. Bretherton [1962] found that the lift per unit length on a cylinder (2D sphere) at small values of $R = \dot{\gamma}a^2 / \nu$ is given by

$$L = \frac{21.16\eta U_s}{(0.679 - \ln(\sqrt{R/4}))^2 + 0.634}. \quad (\text{B.22})$$

Saffman [1965] derived an expression for the lift on a sphere in a linear shear flow

$$L = 6.46\rho_f^{0.5}\eta^{0.5}U_s\dot{\gamma}^{0.5}a^2 + \text{lower order terms} \quad (\text{B.23})$$

where a is the radius of the sphere. The lower order terms are:

$$-U_s a^3 \rho_f \left[\pi \Omega_s - \left(\pi - \frac{22}{8} \right) \frac{1}{2} \dot{\gamma} \right] \quad (\text{B.24})$$

For a neutrally buoyant particle at equilibrium, $L = 0$ and from (B.22) and (B.23), $U_s = 0$. The Bretherton and Saffman formulas thus predict that the slip velocity is zero for a neutrally buoyant particle at equilibrium in an unbounded linear shear flow. Patankar *et al.* [2001] argued that zero slip velocity is always one solution for a neutrally buoyant particle freely moving in an unbounded linear shear flow, but it may not be the only solution and it can be unstable under certain conditions not yet understood. Feng, Hu and Joseph [1994] showed that a neutrally buoyant particle migrates to the centerline in a Couette flow where $U_s = 0$. Ho and Leal [1974] found a neutrally buoyant sphere equilibrates at the centerline in a Couette flow. The difference is that Feng *et al.* [1994] studied 2D particles in flows at finite Reynolds numbers; while Ho and Leal [1974] studied 3D spheres in flows at indefinitely small Reynolds numbers. From our simulations for 2D Poiseuille flows, $U_s \neq 0$ at the equilibrium position of a neutrally buoyant particle (see Fig. B.7); whereas $\Omega_s = \Omega_{se}$ at equilibrium gives rise to zero lift.

We find that our expression for the lift on the stable branch near the centerline (B.21) is similar to the leading term in Saffman's expression for the lift. If we make following changes in equation (B.21): $R = \frac{\rho_f V d}{\eta_0} \rightarrow R = \frac{\rho_f \dot{\gamma} d^2}{\eta}$, the power of R $(-0.515) \rightarrow (-0.5)$, and use $d = 2a$, equation (B.21) becomes:

$$L = 365.2 \rho_f^{0.5} \eta^{0.5} U_s \dot{\gamma}^{-0.5} (\Omega_s - \Omega_{se}^N) a \quad (\text{B.25})$$

Comparing (B.25) and the leading term in (B.23), we note that both expressions are linear in U_s ; both have a similar dependence on ρ_f , η , and a after noting that (B.25) is for the lift force per unit length. However, the dependence on $\dot{\gamma}$ and $\Omega_s - \Omega_{se}$ is greatly different.

Another formula for the lift on a particle in an inviscid fluid in which uniform motion is perturbed by a weak shear was derived by Auton [1987] and a more recent satisfying derivation of the same result was given by Drew and Passman [1999]. They find that in a plane flow,

$$L = \frac{4}{3} \pi a^3 \rho U_s \Omega_f \quad (\text{B.26})$$

where $\Omega_f = -\dot{\gamma}/2$. Our correlation (B.21) reduces to the following form at $R = 22510$,

$$L = \frac{4}{3} \pi a^2 \rho_f U_s (\Omega_s - \Omega_{se}^N). \quad (\text{B.27})$$

Extension to such a high Reynolds number is obviously beyond the range where our correlations are valid. In addition, (B.26) is for 3D spheres and not strictly comparable to our correlations for 2D cylinders. Therefore, the same constant in (B.26) and (B.27) is only intended to qualitatively demonstrate that our correlation at high Reynolds number can match Auton's expression which is for inviscid fluid. The key difference between our correlation and Auton's expression is that we use $\Omega_s - \Omega_{se}^N$ in (B.27), in contrast to Ω_f in (B.26).

Our correlations provide explicit expressions for the lift force on a particle in terms of the slip velocity U_s and the angular slip velocity discrepancy $\Omega_s - \Omega_{se}$. We emphasize that

the relative angular motion is characterized by $\Omega_s - \Omega_{se}$ rather than Ω_s or Ω_f . By using the discrepancy, we are able to account for the Segrè and Silberberg effect. Our correlations cover the whole channel except the unstable regions. We believe that our correlations capture the essence of the mechanism of the lift force.

Correlations (B.20) and (B.21) are derived for L , U_s and Ω_s in steady flows, i.e., they apply to particles with zero acceleration. For a migrating particle, correlations (B.20) and (B.21) are not valid, although they might give good approximations when the acceleration of the particle is small. The application of such correlations is to determine parameters of a particle at equilibrium, e.g., the equilibrium position, translational velocity and angular velocity. For this end, correlations which relate U_s and Ω_s to prescribed parameters are needed. We will show derivation of such correlations is feasible in the next section.

▪ Correlations for slip velocity and angular slip velocity

To make correlations (B.20) and (B.21) completely explicit, we need correlations which relate U_s and Ω_s to R and y/d in steady flows of Newtonian fluids. We illustrate the procedure for Ω_s . In Fig. B.13, the steady state values of $\Omega_s/(2\dot{\gamma}_w)$ obtained in constrained simulations are plotted against y/d for five values of R . If these data are plotted on a log-log plot of $\Omega_s/(2\dot{\gamma}_w)$ versus R , we obtain straight lines one for each value of y/d from the wall to the centerline (five of which are shown in Fig. B.14), leading to power law correlations:

$$\frac{\Omega_s(y/d, R)}{2\dot{\gamma}_w} = b(y/d)R^{r(y/d)} \Rightarrow \Omega_s(y/d, R) = b(y/d)R^{r(y/d)} \frac{R\eta_0}{\rho_f d^2}. \quad (\text{B.28})$$

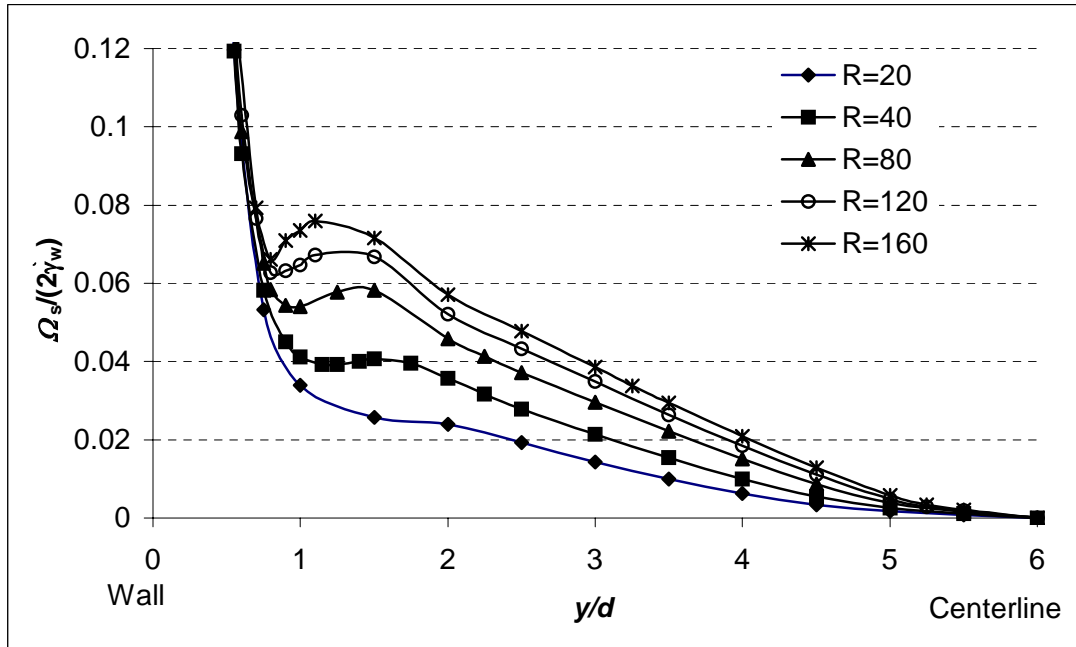


Figure B.13. The steady state values of the dimensionless angular slip velocity $\Omega_s/(2\dot{\gamma}_w)$ in flows of Newtonian fluids as a function of y/d .

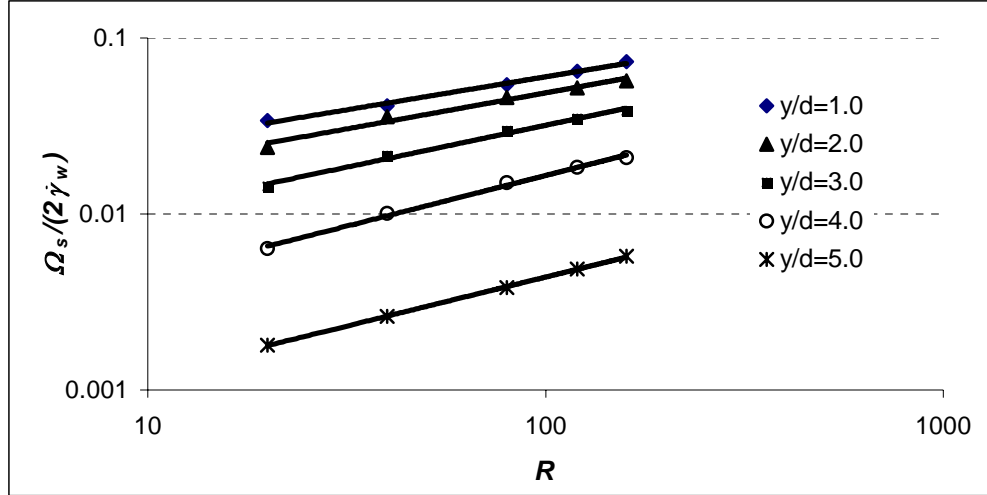


Figure B.14. Power law correlations between $\Omega_s/(2\dot{\gamma}_w)$ and R at five values of y/d .

The prefactor b and exponent r in these power law correlations, which are functions of y/d , are plotted in Fig. B.15. With more data points, these functions could be fitted to splines, making (B.28) completely explicit.

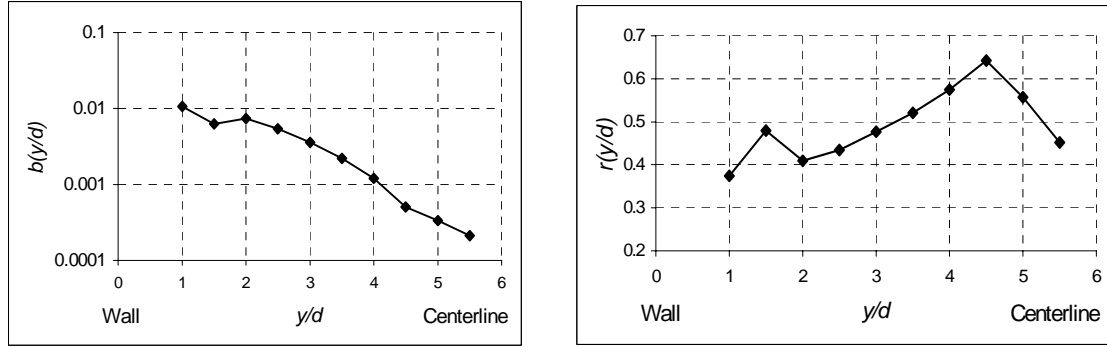


Figure B.15. The prefactor b and exponent r in correlation (B.28) as functions of y/d .

A similar procedure for U_s leads to

$$\frac{U_s(y/d, R)}{2\dot{\gamma}_w d} = c(y/d)R^{q(y/d)} \Rightarrow U_s(y/d, R) = c(y/d)R^{q(y/d)} \frac{R\eta_0}{\rho_f d}. \quad (\text{B.29})$$

As for b and r in (B.28), c and q could be fit to splines if more data points were available. Unlike correlation (B.28) which can be found at values of y/d from the wall to the centerline, correlation (B.29) can only be found at values of y/d on stable branches of steady solutions. It does not correlate well with the data for the unstable branches; in fact for some values of R , U_s is slightly negative at some values of y/d on the unstable branch near the wall, which is incompatible with a power law in the form (B.29).

In addition to (B.28) and (B.29), we also need a correlation between Ω_{se}^N , the angular slip velocity of a neutrally buoyant particle at equilibrium, and R , in order to make (B.20) and (B.21) completely explicit. Table B.7 shows that $\Omega_{se}^N/(2\dot{\gamma}_w)$ is essentially constant independent of R . Using the average of these values, we obtain:

$$\frac{\Omega_{se}^N(R)}{2\dot{\gamma}_w} = 5.21 \times 10^{-3} \Rightarrow \Omega_{se}^N(R) = 5.21 \times 10^{-3} \frac{R\eta_0}{\rho_f d^2}. \quad (\text{B.30})$$

R	20	40	80	120	160
$\Omega_{se}^N / (2\dot{\gamma}_w)$	5.06×10^{-3}	5.24×10^{-3}	5.32×10^{-3}	5.24×10^{-3}	5.21×10^{-3}

Table B.7. The dimensionless angular slip velocity of a neutrally buoyant particle at equilibrium is essentially a constant in flows of Newtonian fluids with $R=20 - 160$.

If we now insert (B.28) - (B.30) into (B.20) and (B.21), we obtain completely explicit (assuming sufficient data points for b , r , c and q to be fit to splines) correlations for the lift force:

$$\left\{ \begin{array}{l} L = 4.20R^{0.0014R+1.2} \left\{ c\left(\frac{y}{d}\right)R^{q\left(\frac{y}{d}\right)} \left[b\left(\frac{y}{d}\right)R^{r\left(\frac{y}{d}\right)} - 5.21 \times 10^{-3} \right] \right\}^{0.0007R+0.386} \frac{\eta_0^2}{\rho_f d} \\ \text{on the stable branch near the wall;} \quad (\text{B.31}) \\ L = 182.6R^{1.485} c\left(\frac{y}{d}\right)R^{q\left(\frac{y}{d}\right)} \left[b\left(\frac{y}{d}\right)R^{r\left(\frac{y}{d}\right)} - 5.21 \times 10^{-3} \right] \frac{\eta_0^2}{\rho_f d} \\ \text{on the stable branch near the centerline.} \quad (\text{B.32}) \end{array} \right.$$

These formulas allow us to calculate L for any value of y/d on the stable branches of the \hat{L} vs. y/d curve (Fig. B.3), obviating the need for further numerical simulations.

The equilibrium position y_e/d of a particle of density ρ_p can be found as the value of y/d at which the lift force equals the buoyant weight:

$$L(y_e/d, R) = (\rho_p - \rho_f)g \frac{\pi d^2}{4};$$

the slip velocities at equilibrium can then be calculated by inserting y_e/d into (B.28) and (B.29):

$$\Omega_{se} = \Omega_s(y_e/d, R) = b(y_e/d)R^{r(y_e/d)} \frac{R\eta_0}{\rho_f d^2};$$

$$U_{se} = U_s(y_e/d, R) = c(y_e/d)R^{q(y_e/d)} \frac{R\eta_0}{\rho_f d}.$$

The corresponding translational velocity U_p and angular velocity Ω_p of the particle at equilibrium may then be calculated as $U_p = U_f(y_e) - U_{se}$ and $\Omega_p = \Omega_{se} - \dot{\gamma}(y_e)/2$.

▪ Conclusions

We study lifting of a cylindrical particle in plane Poiseuille flows of shear thinning fluids. It is known that certain regions in a channel are unstable and a particle cannot equilibrate in an unstable region. For example, Ho and Leal [1974] pointed out the centerline is an unstable equilibrium position in a 2D Poiseuille flow. Our studies show that the domain from the wall to the centerline in a 2D Poiseuille flow can be divided into four regions with the following order: wall – stable – unstable – stable – unstable – centerline. The distribution of these regions is affected by shear thinning. Our results indicate that when shear thinning effects become stronger, the unstable region at the

centerline shrinks, indicating that the equilibrium position of a particle could be closer to the centerline.

The conclusion that the angular slip velocity discrepancy $\Omega_s - \Omega_{se}$ changes sign across an equilibrium position established by Joseph and Ocando [2002] in Newtonian fluids is confirmed in shear thinning fluids. Across a stable equilibrium position, $\Omega_s - \Omega_{se}$ has the same sign as the net lift force L_n ; across an unstable equilibrium position, $\Omega_s - \Omega_{se}$ has the opposite sign as the net lift force L_n .

Correlations for the lift force on a particle in terms of the slip velocity U_s and the angular slip velocity discrepancy $\Omega_s - \Omega_{se}$ are derived. The correlations are a power law near the wall and a linear relation (which can be taken as a power law with the power of one) near the centerline. The correlations apply to both neutrally buoyant and heavy particles and cover the whole channel except the unstable regions. Two regimes, one with no or weak shear thinning effects and the other with strong shear thinning effects, are identified for the power law correlation (B.13) whereas only one regime is found for the linear correlation (B.14). It is noted that particle lift in strong shear thinning flows is different with that in flows of Newtonian fluids at high Reynolds number.

We are able to obtain correlations between L and $U_s(\Omega_s - \Omega_{se})$ with coefficients expressed as functions of R ; these correlations cover the flows of Newtonian fluids with the Reynolds number in the range of 20 - 160. The correlation is compared to well known analytical expressions for lift force in shear flows and similarities between them are revealed. The major difference between them is that the angular slip velocity discrepancy $\Omega_s - \Omega_{se}$ is used in our correlations instead of the shear rate or Ω_s . We also demonstrate that correlations which relate U_s and Ω_s to prescribed parameters can be constructed and will make the correlations for L completely explicit. Thus the lift force in steady flows can be calculated using correlations at any value of y/d on stable branches from the prescribed parameters; the equilibrium position of a particle with a certain density can then be determined by the balance between the lift force and its buoyant weight.

E. Addendum to Chapter XI (Addendum E): Lift Force on a Sphere in tube flow

(from the paper: Migration of a sphere in tube flow B.H. Yang, J. Wang, D.D. Joseph, H.H. Hu, T-W. Pan and R. Glowinski, *J. Fluid Mech.*, 2005)

Abstract

The cross stream migration of a single neutrally buoyant rigid sphere in tube flow is simulated by two packages, one (ALE) based on a moving and adaptive grid and another (DLM) using distributed Lagrange multipliers on a fixed grid. The two packages give results in good agreement with each other and with experiments. A lift law $L = CU_s(\Omega_s - \Omega_{se})$ analogous to $L = \rho UT$ which was proposed and validated in two dimensions is validated in three dimensions here; C is a constant depending on material and geometric parameters, U_s is the slip velocity and it is positive, Ω_s is the slip angular velocity and Ω_{se} is the slip angular velocity when the sphere is in equilibrium at the Segrè-Silberberg radius. The slip angular velocity discrepancy $\Omega_s - \Omega_{se}$ is the circulation for the free particle and it changes sign with the lift. A method of constrained simulation is used to generate data which is processed for correlation formulas for the lift force, slip velocity, and equilibrium position. Our formulas predict the change of sign of the lift force which is necessary in the Segrè-Silberberg effect. Our correlation formula is compared with analytical lift formulas in the literature and with the results of two-dimensional simulations. Our work establishes a general procedure for obtaining correlation formulas from numerical experiments. This procedure forms a link between numerical simulation and engineering practice.

1. Introduction

Migration and equilibrium of solid particles in shear flows have always been of great interest for researchers. Segrè and Silberberg (1961, 1962) studied the migration of dilute suspensions of neutrally buoyant spheres in tube flows and found the particles migrate away from both the wall and the centerline and accumulate at a radial position of about 0.6 times the tube radius. This remarkable Segrè-Silberberg effect has been verified by many experimental works on the same kind of problems. For example, Goldsmith and Mason (1962) observed that a rigid particle stayed at the initial radial position at very small Reynolds numbers and migrated to intermediate positions at finite Reynolds numbers. Karnis, Goldsmith and Mason (1966) reported that neutrally buoyant particles stabilized midway between the centerline and the wall, closer to the wall for larger flow rates and closer to the center for larger particles.

In an attempt to explain the Segrè-Silberberg effect, different analytical expressions for the lift force which causes the particle to migrate transversely were obtained in the literature (Rubinow and Keller 1961, Bretherton 1962, Saffman 1965, 1968, McLaughlin 1991, and Auton 1987 among others). These analytical expressions are based on perturbing Stokes flow with inertia or on perturbing potential flow with a little vorticity. They are explicit and valuable; however, the restrictions on the perturbation analyses make it difficult to apply these expressions to practical problems where the Reynolds number is finite and viscosity is important.

Schonberg & Hinch (1989) analyzed the lift on a neutrally buoyant small sphere in a plane Poiseuille flow, with the channel Reynolds number $R_c = U'_m l / \nu$ less than approximately 100, using matched asymptotic methods. Here U'_m is the maximum velocity of a channel flow, and l is the channel width. The same problem for neutrally buoyant and non-neutrally buoyant small spheres has been studied by Asmolov (1999). He considered the Reynolds number based on the particle size to be asymptotically small while the channel Reynolds number is finite. He computed the lift force on a sphere as a function of the distance from the wall to the sphere center for flows with R_c up to 3000; the results show that the equilibrium position moves towards the wall as R_c increases. When the particle Reynolds number is small, the disturbance flow due to the particle is governed by creeping-flow equations to leading order; one can compute the transverse component of the velocity at the particle center and use the Stokes drag law to calculate the lift. The analysis takes the effect of inertia $(\mathbf{u} \cdot \nabla)\mathbf{u}$ into account only in an Oseen linear system. The analysis is heavy and explicit formulas for the lift are not obtained.

Feng, Hu and Joseph (1994) performed numerical simulations of the motion of a two-dimensional circular particle in Couette and Poiseuille flows. Patankar, Huang, Ko and Joseph (2001) and Joseph and Ocando (2002) simulated the motion of a two-dimensional circular particle in plane Poiseuille flows perpendicular to gravity in Newtonian and viscoelastic fluids. They showed that multiple equilibrium states exist for particles with intermediate densities; these equilibrium states can be stable or unstable.

Relative motions between the fluid and the particle, which may be characterized by slip velocities, are essential to understand the lift force on the particle. We use U_p and Ω_p to denote the translational and angular velocities of the particle at steady state and the slip velocities are defined as:

$$U_s = U_f - U_p, \text{ the slip velocity;} \quad (1.1)$$

$$\Omega_s = \Omega_p - \Omega_f = \Omega_p + \dot{\gamma}/2, \text{ the slip angular velocity,} \quad (1.2)$$

where U_f and $\dot{\gamma}$ are the fluid velocity and local shear rate evaluated at the location of the particle center in the undisturbed flow. Joseph and Ocando (2002) found that the discrepancy $\Omega_s - \Omega_{se}$, where Ω_{se} is the slip angular velocity at equilibrium, changes sign across the equilibrium position just as the lift force does. Thus, this discrepancy can be used to account for the migration toward the intermediate equilibrium position from the centerline and the wall (the Segrè-Silberberg effect).

Following Joseph and Ocando's analysis, Wang and Joseph (2003) constructed correlations for the lift force by analogy with the classical lift formula $L = \rho U \Gamma$ of aerodynamics; they showed that the proper analogs of U and Γ were U_s and $\Omega_s - \Omega_{se}$. Their correlations apply to a freely rotating two-dimensional circular particle without accelerations in a plane Poiseuille flow. They also demonstrated that the correlations for lift force could be made completely explicit provided that the correlations relating U_s and Ω_s to prescribed parameters were obtained.

The results from two-dimensional simulations presented by Feng, Hu and Joseph (1994), Patankar *et al.* (2001), Joseph and Ocando (2002) and Wang and Joseph (2003) are difficult to compare with experimental results because the majority of the experiments are for spherical particles in circular tube flows. The lift force correlations by Wang and Joseph are for circular particles and can not be rigorously compared to analytical lift expressions for spheres. All the above mentioned authors used a two-dimensional finite element scheme based on unstructured body-fitted moving grids first developed by Hu, Joseph and Crochet (1992). Recently, Hu and Zhu extended the two-dimensional scheme to three-dimensional and performed simulations of the migration of spheres in tube Poiseuille flows (see the PhD thesis of Zhu 2000). We call this scheme the ALE code because an arbitrary Lagrangian-Eulerian moving mesh technique has been adopted to deal with the motion of the particles. The three-dimensional ALE scheme is used in the current work to study the lift force on a neutrally buoyant sphere in tube Poiseuille flow.

Another approach to simulate the solid-liquid flow initiated by us is based on the principle of embedded or fictitious domains. In this approach, the Navier-Stokes equations are solved everywhere, including inside the particles. The flow inside the particles is forced to be a rigid body motion by a distribution of Lagrange multipliers – thus we call this scheme the DLM code. Detailed descriptions of the DLM method can be found in Glowinski, Pan, and Periaux (1998); Glowinski, Pan, Hesla, and Joseph (1999); Glowinski, Pan, Hesla, Joseph, and Periaux (1999, 2001); Singh, Joseph, Hesla, Glowinski and Pan (2000) and Glowinski (2003). The two quite different schemes, the DLM code and the ALE code, are both employed to simulate the motion of a neutrally buoyant sphere in tube Poiseuille flow in the current work. We shall show that the

results of the two codes are in good agreement, which provides strong support for the credibility of our numerical simulation.

The main goal of this work is to extend the correlation of the lift force in terms of U_s and the discrepancy $\Omega_s - \Omega_{se}$ to three-dimensional cases, which would give a more convincing explanation for the Segrè-Silberberg effect. The lift force correlations represent efforts to draw explicit formulas from numerical simulation data. There is no reason why “empirical” formulas of the type used in engineering which correlate experimental data cannot be generated from the data produced by numerical simulations. Correlations have already been obtained for single particle lift (Patankar *et al.* 2001, Wang and Joseph 2003) and for the bed expansion of many particles (Choi and Joseph 2001, Patankar, Ko, Choi and Joseph 2001) by processing numerical data. Our works have establish general rules for the interrogation of data from numerical simulation to be used in developing models for complex fluid dynamics problems such as the fluidization by lift or drag.

2. Governing equations and dimensionless parameters

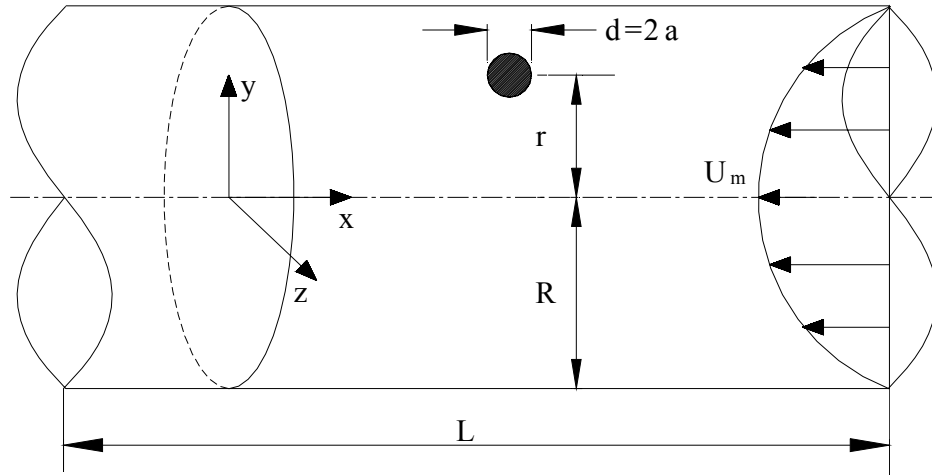


Figure E-1. Sketch for the problem of a rigid sphere in a tube Poiseuille flow. The sphere is neutrally buoyant and the orientation of the gravity is irrelevant.

The governing equations for the incompressible Newtonian fluid are

$$\nabla \cdot \mathbf{u} = 0 \text{ and } \rho_f \left(\frac{\partial \mathbf{u}}{\partial t} + (\mathbf{u} \cdot \nabla) \mathbf{u} \right) = -\nabla P + \rho_f \mathbf{g} + \mu \nabla^2 \mathbf{u} \quad (2.1)$$

where $\mathbf{u}(\mathbf{x}, t)$ is the fluid velocity, ρ_f is the fluid density, $P(\mathbf{x}, t)$ is the pressure, \mathbf{g} is the gravitational acceleration, and μ is the fluid viscosity. We can absorb the gravity term in the Navier-Stokes equations into the pressure by decomposing the pressure as

$$\mathbf{P} = p + \rho_f \mathbf{g} \cdot \mathbf{x}. \quad (2.2)$$

The equations of motion of the solid particles in a general three-dimensional case are

$$\begin{aligned} m \frac{d\mathbf{U}_p}{dt} &= m\mathbf{g} + \int [-\mathbf{P}\mathbf{1} + \boldsymbol{\tau}] \cdot \mathbf{n} d\Gamma, \\ \frac{d(\mathbf{I} \cdot \boldsymbol{\Omega}_p)}{dt} &= \int (\mathbf{x} - \mathbf{X}_p) \times ([-\mathbf{P}\mathbf{1} + \boldsymbol{\tau}] \cdot \mathbf{n}) d\Gamma, \end{aligned} \quad (2.3)$$

where m is the mass of the particle, \mathbf{U}_p is the translational velocity, $\boldsymbol{\Omega}_p$ is the angular velocity, \mathbf{I} is the moment of inertia tensor and \mathbf{X}_p is the coordinate of the center of mass of the particle. We consider a solid sphere with a radius a and $m = \rho_p 4\pi a^3 / 3$, $\mathbf{I} = \text{diag}(2ma^2/5)$. The no-slip condition is imposed on the particle boundaries

$$\mathbf{u} = \mathbf{U}_p + \boldsymbol{\Omega}_p \times (\mathbf{x} - \mathbf{X}_p) \quad (2.4)$$

and on the tube wall $\mathbf{u} = 0$. The velocity profile at the inlet of the tube is prescribed by

$$u = U_m (1 - r^2 / R^2), \quad (2.5)$$

where U_m is the maximum velocity at the centerline of the tube; r is the radial position and R is the radius of the tube. The traction-free boundary condition is imposed at the outlet of the tube:

$$f_n \equiv \mathbf{n} \cdot \mathbf{T} \cdot \mathbf{n} = 0; \quad u_y = 0; \quad u_z = 0, \quad (2.6)$$

where $\mathbf{T} = -\mathbf{P}\mathbf{1} + \boldsymbol{\tau}$ is the total stress tensor and \mathbf{n} is the norm at the outlet of the tube.

The undisturbed tube Poiseuille flow without particles is given by (2.5). The shear rate at the wall ($r = R$) is given by $\dot{\gamma}_w = 2U_m / R$. To non-dimensionalize the governing equations, we use the velocity $V = 2a\dot{\gamma}_w$ as the characteristic velocity, $2a$ for length, $2a/V$ for time, $\mu V / 2a$ for stress and pressure, and $\dot{\gamma}_w$ for angular velocity. The dimensionless equations are (we use the same symbols for dimensionless variables)

$$\nabla \cdot \mathbf{u} = 0, \quad (2.7)$$

$$R_e \left(\frac{\partial \mathbf{u}}{\partial t} + (\mathbf{u} \cdot \nabla) \mathbf{u} \right) = -\nabla p + \nabla^2 \mathbf{u}, \quad (2.8)$$

$$\begin{aligned} \frac{\rho_p}{\rho_f} R_e \frac{d\mathbf{U}_p}{dt} &= G \mathbf{e}_g + \frac{6}{\pi} \int [-p\mathbf{1} + \boldsymbol{\tau}] \cdot \mathbf{n} d\Gamma, \\ \frac{\rho_p}{\rho_f} R_e \frac{d\boldsymbol{\Omega}_p}{dt} &= \frac{60}{\pi} \int (\mathbf{x} - \mathbf{X}_p) \times ([-p\mathbf{1} + \boldsymbol{\tau}] \cdot \mathbf{n}) d\Gamma, \end{aligned} \quad (2.9)$$

where \mathbf{e}_g is the unit vector in the direction of the gravity. The dimensionless parameters are

$$R_e = \frac{\rho_f V(2a)}{\mu} = \frac{\rho_f \dot{\gamma}_w(2a)^2}{\mu} = \frac{8a^2 \rho_f U_m}{\mu R}, \text{ the Reynolds number;} \quad (2.10)$$

$$G = \frac{(\rho_p - \rho_f)g(2a)^2}{\mu V}, \text{ the gravity number;} \quad (2.11)$$

$$\rho_p / \rho_f, \text{ the density ratio.} \quad (2.12)$$

It is convenient to carry out the analysis of correlations in terms of dimensionless forms of correlating parameters. The ratio of the sphere radius a to pipe radius R and the dimensionless radial position \bar{r} are defined by

$$\bar{a} = a/R, \bar{r} = r/R. \quad (2.13)$$

The dimensionless lift is given by

$$\bar{L} = \frac{6\rho_f L}{\pi\mu^2}. \quad (2.14)$$

The flow quantities U_m , U_s , Ω_s , Ω_{se} are expressed in the form of dimensionless Reynolds numbers. A flow Reynolds number is given by

$$\bar{U}_m = \frac{\rho_f U_m R}{\mu} = \frac{R_e}{8\bar{a}^2} \quad (2.15)$$

Slip velocity Reynolds numbers are defined as

$$\begin{aligned} \bar{U}_s &= \rho_f U_s(2a) / \mu, \\ \bar{\Omega}_s &= \rho_f \Omega_s(2a)^2 / \mu, \\ \bar{\Omega}_{se} &= \rho_f \Omega_{se}(2a)^2 / \mu. \end{aligned} \quad (2.16)$$

A dimensionless form of the product $U_s(\Omega_s - \Omega_{se})$ which enters into our lift law is given as the product

$$\bar{U}_s(\bar{\Omega}_s - \bar{\Omega}_{se}). \quad (2.17)$$

We call the reader's attention to the fact that the flow is in the negative x direction in our simulation (see figure E-1). The symbol U_m in (2.10) and (2.15) should be understood as the magnitude of the fluid velocity at the tube centerline. Similarly, we use the magnitude of U_f and U_p to calculate the slip velocity U_s defined in (1.1).

We shall focus on the steady state flow of a neutrally buoyant sphere, in which the left side of (2.9) and the term $G\mathbf{e}_g$ in (2.9) vanish. Thus, R_e and \bar{a} are the two parameters at play.

3. Comparison of results

We study the behavior of a neutrally buoyant sphere suspended in tube Poiseuille flows. A comparison of the numerical results using the ALE code with the experiments by Karnis, Goldsmith and Mason (1966) was presented by Zhu (2000). Karnis *et al.* performed a large number of experiments on the migration of spheres, rods and disks in a Poiseuille flow in a capillary tube. Zhu (2000) compared the trajectories of spheres released at two radial positions $\bar{r} = 0.21$ and 0.68 to the trajectories measured by Karnis *et al.* Figure E-2 shows that the numerical results are in excellent agreement with the experimental ones.

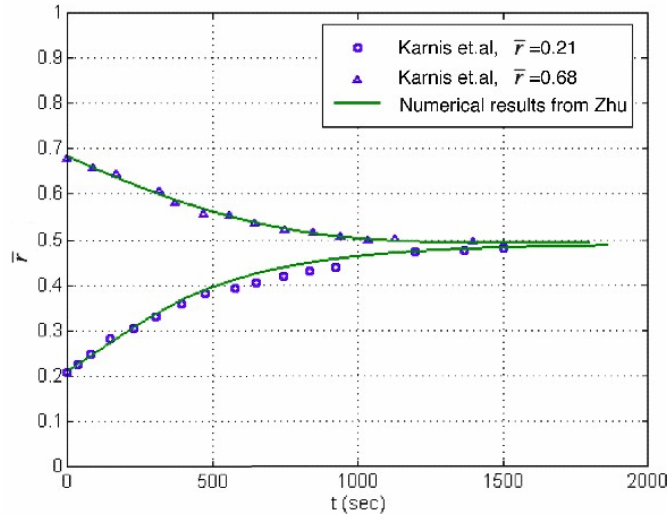


Figure E-2. Comparison of migration trajectories of a neutrally buoyant sphere calculated numerically with the ones measured in the experiments of Karnis, Goldsmith and Mason (1966). The fluid properties are $\rho_f = 1.05 \text{ g}\cdot\text{cm}^{-3}$ and $\mu = 1.2 \text{ poises}$, the flow rate is $Q = 7.11 \times 10^{-2} \text{ cm}^3/\text{sec}$, the tube diameter is $D = 0.4 \text{ cm}$, and the sphere diameter is $d = 0.122 \text{ cm}$.

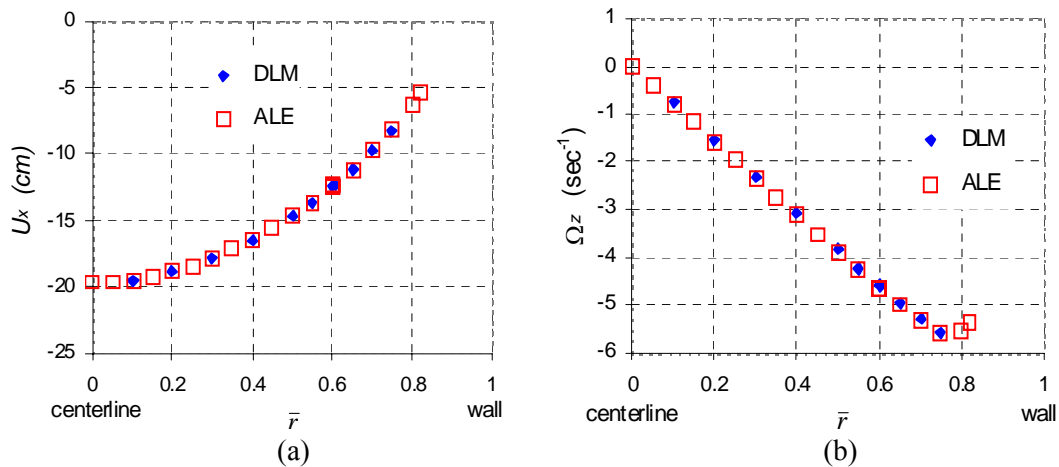
An equilibrium for a free neutrally buoyant particle is achieved when the particle migrates to a radial position \bar{r}_e of steady rectilinear motion in which the acceleration and angular acceleration vanish and the hydrodynamic lift force is zero. We perform two types of simulations, unconstrained and constrained simulations, to find the equilibrium position. In unconstrained simulation, the particle moves freely until it reaches its equilibrium position, just as it would do in experiments. In constrained simulation, the particle is only allowed to move along a line parallel to the axis of the tube and rotate freely; its lateral migration is suppressed and radial position is fixed. When such a constrained motion reaches steady state in which the particle accelerations vanish, a hydrodynamic lift force L in the radial direction can be calculated. This lift force L is a function of the radial position; the position where $L = 0$ is the equilibrium position \bar{r}_e . In our constrained simulation, we place the sphere center at $(y = r, z = 0)$ (see figure E-1), so that the lift

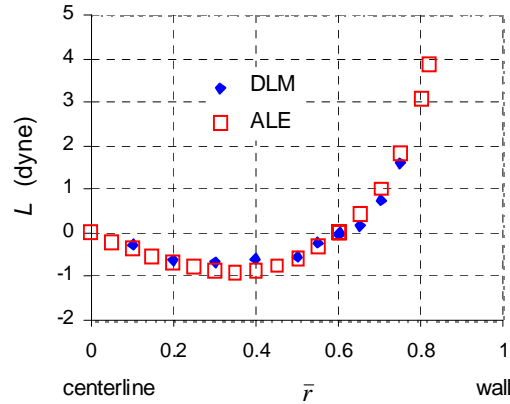
force at steady state is in y direction and z direction is the neutral direction. The only component of the particle translational velocity at steady state is U_x and Ω_z is the only component of the angular velocity.

We compare the results of the unconstrained and constrained simulations obtained using the ALE code and the DLM code. In the ALE code, the typical mesh used in most of our simulations consists of 1.05×10^5 elements, 1.46×10^5 nodes and 1.9×10^4 vertices. The number of nodes for velocity is about 2.22×10^6 in the DLM code. We consider a case in which the radii of the particle and the tube are 0.375 cm and 2.5 cm respectively (the radius ratio $\bar{a} = 0.15$), the density of the particle and the fluid is 1 g/cm^3 , the viscosity of the fluid is 1 poise, and $U_m = 20 \text{ cm/sec}$ ($Re = 9$). We compare the equilibrium position \bar{r}_e and velocities U_x and Ω_z at equilibrium calculated from the unconstrained simulation in table E-1. We compare the lift force $L(\bar{r})$, velocities $U_x(\bar{r})$ and $\Omega_z(\bar{r})$, calculated from the constrained simulation in figure E-3.

	\bar{r}_e	U_x (cm/sec)	Ω_z (sec $^{-1}$)
ALE	0.601	12.4	4.65
DLM	0.606	12.2	4.63

Table E-1. The equilibrium position \bar{r}_e and particle velocities U_x and Ω_z at equilibrium calculated from the unconstrained simulation. The results of the ALE and DLM codes are almost the same.





(c)

Figure E-3. The steady state values of the particle velocities U_x (a) and Ω_z (b) and the lift force L (c), from the constrained simulation at different radial positions. The ALE and DLM results are in good agreement.

Figures E-3.a and E-3.b show that the particle translational and angular velocities obtained from the DLM and ALE codes are almost the same. The agreement of the lift forces from the two codes in figure E-3.c is not as good as the velocities. The lift force curve from the DLM code is not quite smooth since this method was intended to simulate the dynamics of the interaction of fluid and many particles and not to compute the hydrodynamic forces explicitly. Nevertheless, we regard the agreement in figure E-3.c acceptable, considering the challenging nature of the three-dimensional simulation. Due to mesh adaptivity, the ALE code is more suited to accurate computation of lift. We will use the data from the ALE code to construct the lift correlations in the following section.

Our two different codes give results in good agreement with each other and with experiments, which demonstrates that our numerical simulation is credible.

4. Correlations from the numerical simulation

Numerical experiments using constrained simulation provide us with the distribution of the lift force and particle velocity in the tube and the position and velocity of the particle at equilibrium. We develop correlations for these quantities in this section. The key correlation is for the lift force, which shows the dependence of the lift force on the slip angular velocity discrepancy $\Omega_s - \Omega_{se}$. The lift force correlation predicts the change of sign of the lift force, which is necessary to explain the two-way migration in the Segrè-Silberberg effect. The correlations for the equilibrium state of the particle are also of interest, because they may be used to predict the position and the velocities of the particle at equilibrium.

4.1 Correlation for the lift force

The steady state values of the lift forces on a sphere at different radial positions computed in constrained simulation are plotted in figure 4 for a sphere with the radius ratio $\bar{a} = 0.15$. The positive direction of the lift force is in the negative \mathbf{e}_r direction. In other words, \bar{L} is positive when pointing to the centerline and negative when pointing away from the centerline.

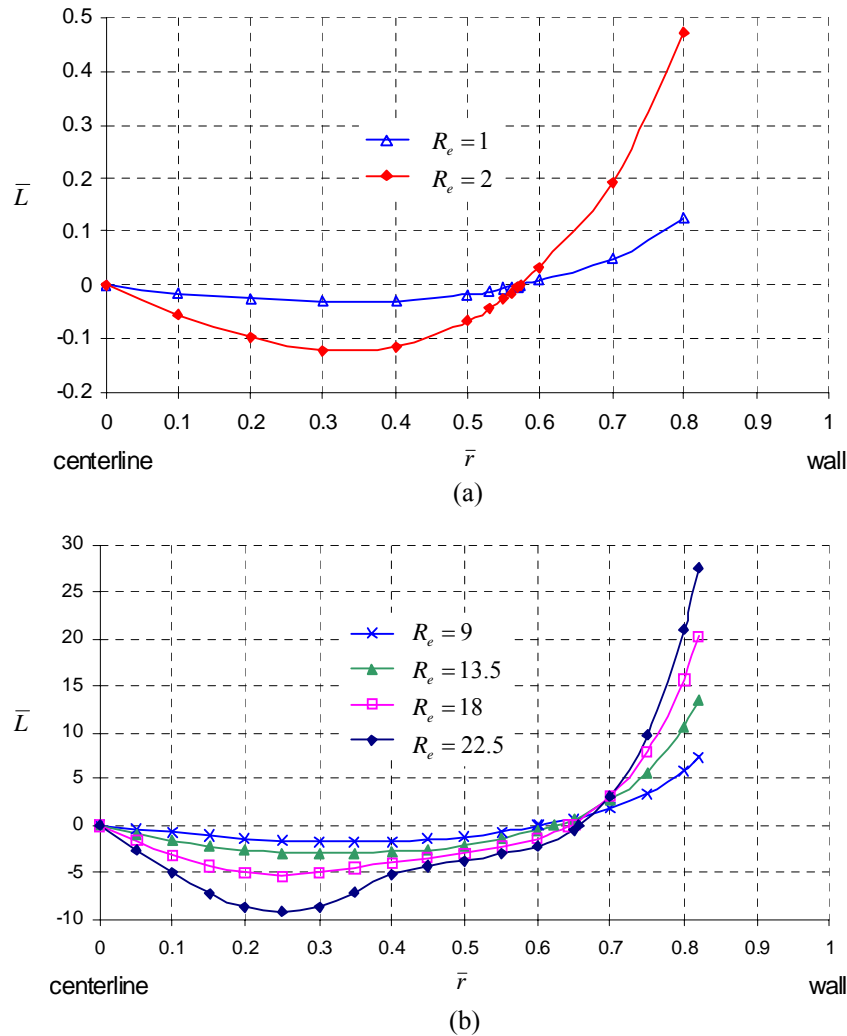


Figure E-4. The dimensionless lift force \bar{L} at different radial positions for a sphere with the radius ratio $\bar{a} = 0.15$. The two curves in (a) correspond to $R_e = 1$ and 2, and the four curves in (b) correspond to $R_e = 9, 13.5, 18$ and 22.5, respectively. The magnitude of the lift force increases with the Reynolds number.

The equilibrium positions of a neutrally buoyant sphere are the points where $\bar{L} = 0$. The stability of the equilibrium at a zero-lift point can be determined from the slope of the \bar{L} vs. \bar{r} curve. The centerline is on a negative-slope branch of the \bar{L} vs. \bar{r} curve. When a particle is disturbed away from the centerline, the lift force is negative and drives the particle further away

from the centerline. Therefore the centerline is an unstable equilibrium position. The other zero-lift point is between the centerline and the wall and it is on a positive-slope branch of the curve. When the particle is disturbed away from this point, the lift force tends to push the particle back. Thus the zero-lift point between the centerline and the wall is a stable equilibrium position. Figure E-4 shows that this stable equilibrium position \bar{r}_e moves towards the wall as the Reynolds number increases.

We seek expressions for the lift force in terms of the slip velocities. The slip velocity Reynolds numbers have been defined in (2.16). We plot $\bar{\Omega}_s - \bar{\Omega}_{se}$ at different radial positions in figure E-5 for a sphere with $\bar{a} = 0.15$. Comparison of figure E-4 and figure E-5 shows that the discrepancy $\bar{\Omega}_s - \bar{\Omega}_{se}$ changes sign across the equilibrium position, just like the lift force \bar{L} does.

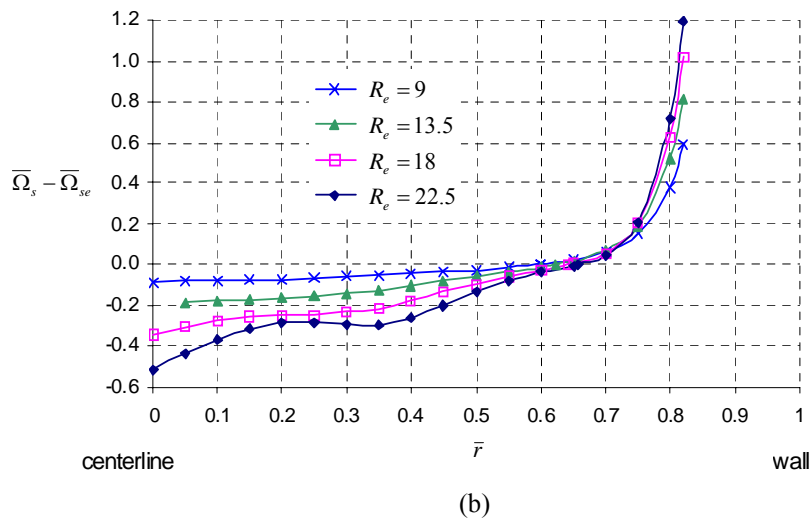
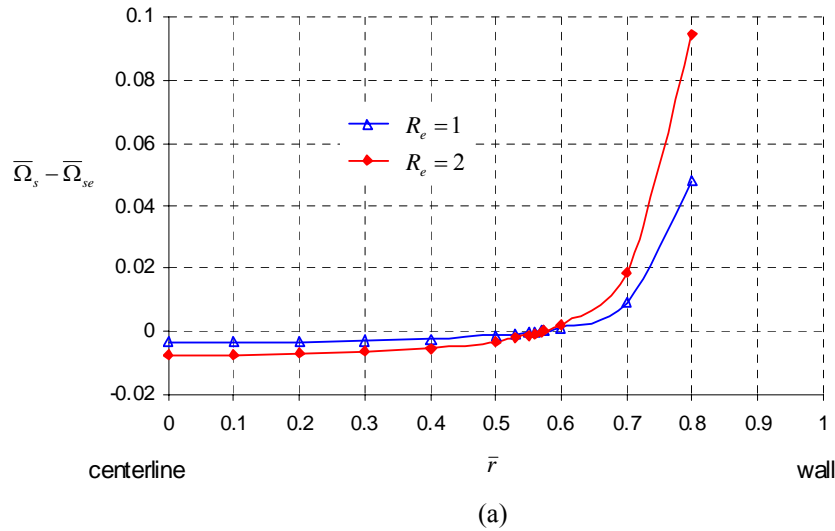


Figure E-5. The dimensionless slip angular velocity discrepancy at different radial positions for a sphere with $\bar{a} = 0.15$. The two curves in (a) correspond to $R_e = 1$ and 2, and the four curves in (b) correspond to $R_e = 9, 13.5, 18$ and 22.5, respectively.

If we fix the radius ratio $\bar{a} = 0.15$ and continue to increase the Reynolds number, the distribution of the lift force as a function of the radial position becomes more complicated. We plot the \bar{L} vs. \bar{r} curves for $R_e = 27, 36$ and 45 in figure E-6. There is a change of convexity in the curves and a local minimum of the lift force exists at approximately $\bar{r} = 0.55$. On each of the curves, there exist two branches on which the slope of the curve is negative. The first negative-slope branch is at the centerline; the second negative-slope branch is in the middle between the centerline and the wall. The second negative-slope branch does not exist when the Reynolds number is small ($R_e = 1, 2, 9, 13.5, 18$ or 22.5). The exact range of the second negative-slope branch varies with the Reynolds number; we may say that the range $0.5 \leq \bar{r} \leq 0.65$ covers the second negative-slope branches of the curves for $R_e = 27, 36$ and 45. We found that it was difficult for the constrained simulations in this range at high Reynolds numbers to converge to a steady state; a refined mesh was necessary to obtain converged results in these simulations. For example, when $R_e = 1$, the typical mesh used in our simulations consists of 9.09×10^4 elements, 1.28×10^5 nodes and 1.68×10^4 vertices; when $R_e = 45$, the typical mesh consists of 9.86×10^4 elements, 1.39×10^5 nodes and 1.82×10^4 vertices.

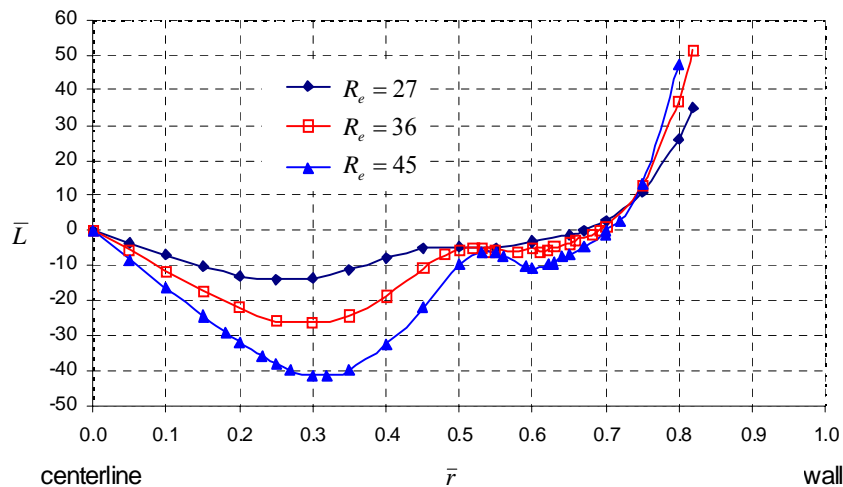


Figure E-6. The dimensionless lift force \bar{L} at different radial positions for a sphere with $\bar{a} = 0.15$. The three curves corresponds to $R_e = 27, 36$ and 45, respectively. On each of the curve, there exist two branches on which the slope of the curve is negative.

Similar complicated distributions of the lift force can be observed in Asmolov's (1999) calculation of the lift force on a small neutrally buoyant sphere in a plane Poiseuille flow. In his figure E-8, the lift is plotted as a function of d/l , where d is the distance from the wall to the particle center and l is the channel width. Five curves for five channel Reynolds numbers $R_c = 15, 100, 300, 1000$ and 3000 are plotted. There is only one negative-slope branch on the curves for $R_c = 15$ and 100 , which is at the centerline. There are two negative-slope branches on the curves for $R_c = 300, 1000$ and 3000 . One of the branches is at the centerline and the other is between the centerline and the wall. Both our numerical simulation and Asmolov's (1999) calculation using matched asymptotic methods show that at high R_e , there exists a local minimum of the lift force between the centerline and the stable equilibrium position. This observation prompts us to consider the possibility of multiple equilibrium positions for neutrally buoyant particles in Poiseuille flows.

Matas, Morris and Guazzelli (2004) measured lateral migration of dilute suspensions of neutrally buoyant spheres in pipe flows; they observed single equilibrium positions when \bar{U}_m is low (60, 350) and multiple equilibrium positions when \bar{U}_m is high (760). In their experiments using spheres with $\bar{a} = 0.06875$ in flows with $\bar{U}_m = 760$, they observed a first equilibrium position close to the wall and a second equilibrium position at $\bar{r} = 0.5 \pm 0.2$. They also reported that when \bar{U}_m is increased to 1500, the first equilibrium position close to the wall disappeared and the second equilibrium position became the only equilibrium position. Matas, Morris and Guazzelli proposed to explain the second equilibrium position using the change of convexity in the lift force profiles obtained from the matched asymptotic methods. They argued that the particles could accumulate in the region near the local minimum of the lift force.

In numerical simulations, Patankar, Huang, Ko and Joseph (2001) reported multiple equilibrium positions for particles heavier than the fluid in plane Poiseuille flows perpendicular to the gravity. We have not obtained multiple equilibrium positions in simulations for a neutrally buoyant sphere in pipe flows. We are not able to run simulations matching the experimental conditions under which multiple equilibrium positions were observed. From figure E-6, it seems possible that a second stable equilibrium position appears near $\bar{r} = 0.55$ at higher R_e . It is also possible that the second equilibrium position arises from particle interaction in the experiments. The existence of multiple equilibrium positions for a single neutrally buoyant particle in a pipe flow is still an open question.

The $\bar{\Omega}_s - \bar{\Omega}_{se}$ vs. \bar{r} curves for the cases with $\bar{a} = 0.15$ and $R_e = 27, 36$ or 45 are plotted in figure E-7. Our assertion that the lift force changes sign with the discrepancy $\bar{\Omega}_s - \bar{\Omega}_{se}$ remains true for $R_e = 27$ and 36 but not for $R_e = 45$. When $R_e = 45$, $\bar{\Omega}_s - \bar{\Omega}_{se}$ changes sign twice in the range $0 < \bar{r} < 0.5$ (figure E-7); however, the lift force remains negative in the same range (figure E-6). Our assertion is true in the vicinity of the stable equilibrium position at all the Reynolds numbers, which will be the region in which the lift correlation is developed.

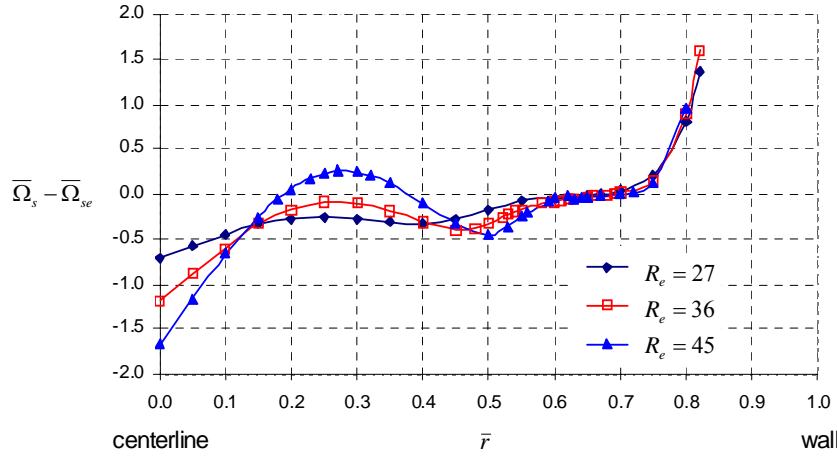


Figure E-7. The dimensionless slip angular velocity discrepancy at different radial positions for a sphere with $\bar{a} = 0.15$. The three curves correspond to $R_e = 27, 36$, and 45 , respectively.

We seek correlations between the lift force \bar{L} and the product

$$F = \bar{U}_s (\bar{\Omega}_s - \bar{\Omega}_{se}). \quad (4.1)$$

From our data, we noted that in the vicinity of the stable equilibrium position, the relation between \bar{L} and F may be represented by a linear correlation:

$$\bar{L}(\bar{r}, R_e, \bar{a}) = k(R_e, \bar{a})F(\bar{r}, R_e, \bar{a}), \quad (4.2)$$

where k is the proportionality coefficient which depends on the Reynolds number and the radius ratio \bar{a} . Some examples of the linear correlation between \bar{L} and F are plotted in figure E-8 and the values of k are listed in table E-2. The linear correlation (4.2) is not valid far away from the equilibrium position; we also list the range of the radial position in which the linear correlation is valid in table E-2.

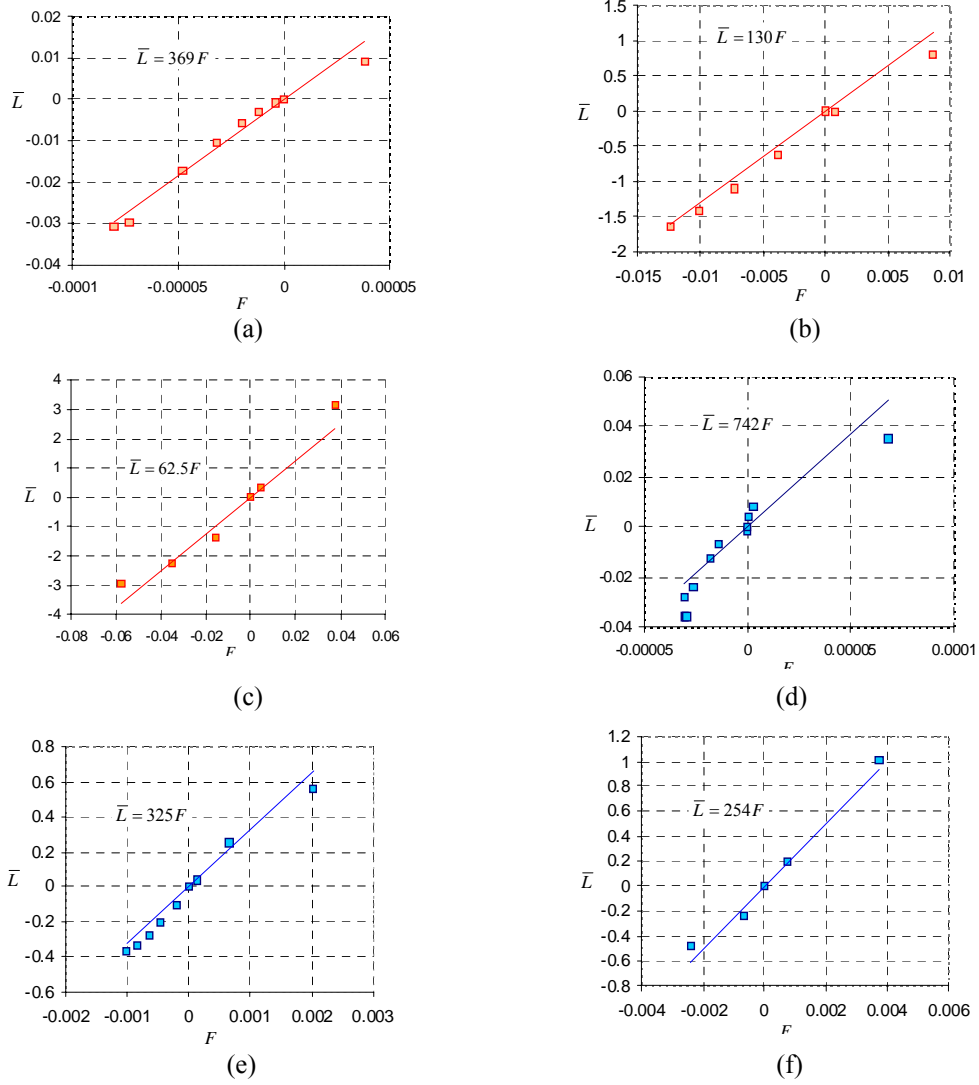


Figure E-8. The linear correlation between \bar{L} and F in the vicinity of the stable equilibrium position of a neutrally buoyant particle. (a) $R_e = 1$, $\bar{a} = 0.15$; (b) $R_e = 9$, $\bar{a} = 0.15$; (c) $R_e = 18$, $\bar{a} = 0.15$; (d) $R_e = 1$, $\bar{a} = 0.1$; (e) $R_e = 4$, $\bar{a} = 0.1$; (f) $R_e = 8$, $\bar{a} = 0.1$.

\bar{a}	R_e	k	equilibrium position \bar{r}_e	range of the linear correlation
0.1	1	742	0.603	$0.2 \leq \bar{r} \leq 0.7$
	2	620	0.608	$0.3 \leq \bar{r} \leq 0.7$
	4	325	0.638	$0.4 \leq \bar{r} \leq 0.75$
	6	268	0.661	$0.55 \leq \bar{r} \leq 0.75$
	8	254	0.674	$0.6 \leq \bar{r} \leq 0.75$
	10	201	0.684	$0.6 \leq \bar{r} \leq 0.75$
	12	169	0.708	$0.65 \leq \bar{r} \leq 0.8$
0.15	1	369	0.573	$0.3 \leq \bar{r} \leq 0.6$
	2	346	0.573	$0.3 \leq \bar{r} \leq 0.6$
	9	130	0.601	$0.4 \leq \bar{r} \leq 0.65$
	13.5	77.2	0.623	$0.45 \leq \bar{r} \leq 0.7$
	18	62.5	0.642	$0.5 \leq \bar{r} \leq 0.7$

	22.5	53.5	0.657	$0.55 \leq \bar{r} \leq 0.7$
	27	56.5	0.670	$0.6 \leq \bar{r} \leq 0.75$
	36	69.8	0.691	$0.65 \leq \bar{r} \leq 0.75$
	45	85.2	0.700	$0.67 \leq \bar{r} \leq 0.75$

Table E-2. The values of the proportionality coefficient k and the equilibrium position \bar{r}_e as functions of the radius ratio \bar{a} and R_e . The range of the radial position in which the linear correlation (4.2) is valid is also listed.

The value of k decreases as R_e increases when the Reynolds number is low. However, k increases as R_e increases when $R_e \geq 27$. This change is possibly related to the emergence of the second negative-slope branch on the \bar{L} vs. \bar{r} plot at high Reynolds numbers. We shall focus on the low Reynolds number cases and data fitting analyses lead to expressions for k in terms of the Reynolds number:

$$k = 809R_e^{-0.604}, \quad \text{for } \bar{a} = 0.1 \quad \text{and } 1 \leq R_e \leq 12; \quad (4.3)$$

$$k = 450R_e^{-0.658}, \quad \text{for } \bar{a} = 0.15 \quad \text{and } 1 \leq R_e \leq 22.5. \quad (4.4)$$

Inserting the expression of k into the linear correlation (4.2), we can obtain the correlations between \bar{L} and F . To reveal the dependence of the lift force on the slip velocities explicitly, we substitute the definitions of \bar{L} and F into the linear correlation and it follows that

$$L = 424R_e^{-0.604} \rho_f U_s (\Omega_s - \Omega_{se}) (2a)^3, \quad \text{for } \bar{a} = 0.1; \quad (4.5)$$

$$L = 236R_e^{-0.658} \rho_f U_s (\Omega_s - \Omega_{se}) (2a)^3, \quad \text{for } \bar{a} = 0.15. \quad (4.6)$$

Both of these two correlations are analogous to the lift correlation we obtained in the two-dimensional cases (Wang and Joseph 2003):

$$L = 182.6R_e^{-0.515} \rho_f U_s (\Omega_s - \Omega_{se}) (2a)^2, \quad (4.7)$$

which is for the lift force per unit length on a cylindrical particle whose diameter is 1/12 of the channel width. It is noted that the exponent of the Reynolds number is -0.604 in (4.5) and it is closer to the value -0.515 in (4.7).

The lift force in our correlation is on a freely rotating particle translating at steady velocity. Thus correlations (4.5) and (4.6) apply to particles with zero acceleration. For a migrating particle with substantial acceleration, correlations (4.5) and (4.6) may not be valid.

4.2 Correlations for the slip velocity U_s and slip angular velocity Ω_s

Besides the lift force on the particle, the translational and angular velocities of the particle at steady state are also of interest. We shall construct correlations for the slip velocity U_s and slip

angular velocity Ω_s from constrained simulations; the particle velocities can then be easily computed using (1.1) and (1.2). The correlations for U_s and Ω_s are necessary to compute the lift force, because they appear in the lift correlations (4.5) and (4.6).

We illustrate the correlation construction for a particle with the radius ratio $\bar{a} = 0.15$. We plot the Reynolds number $\bar{\Omega}_s$ on log-log plots versus R_e ; straight lines one for each value of \bar{r} are obtained. Similar straight lines on log-log plots are obtained when we plot \bar{U}_s versus R_e . Examples of such plots are shown in figure E-9.a and 9.b for $\bar{\Omega}_s$ vs. R_e and \bar{U}_s vs. R_e , respectively.

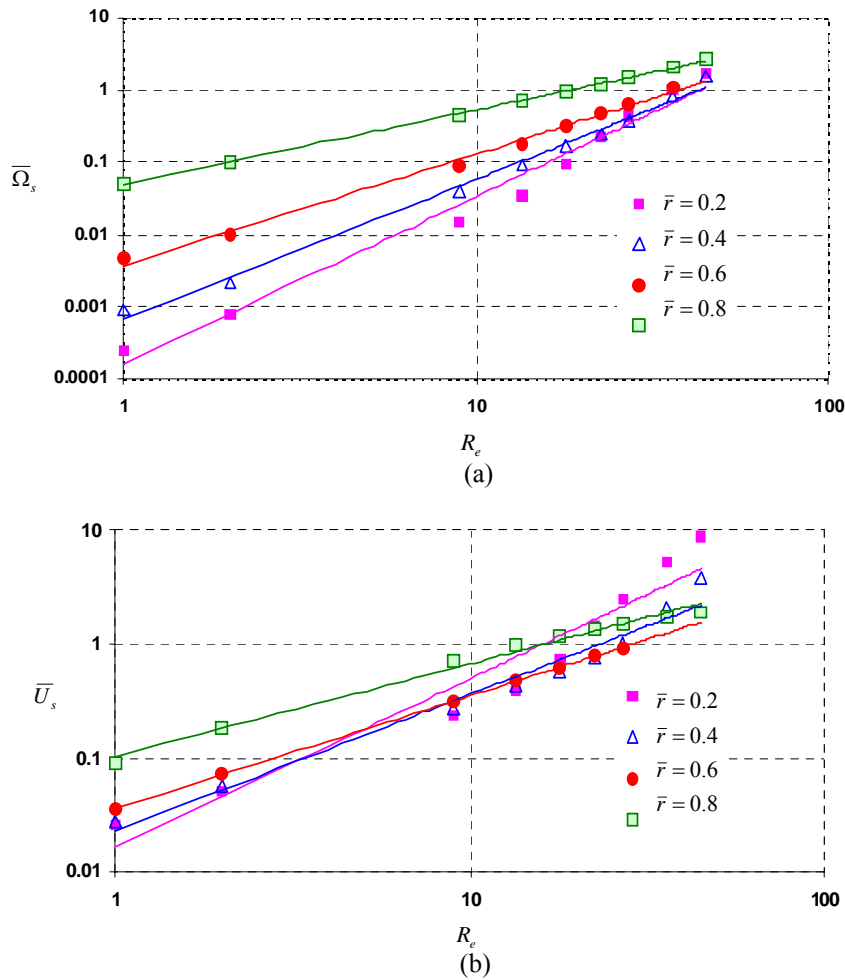


Figure E-9. Power law correlations of (a) $\bar{\Omega}_s$ vs. R_e and (b) \bar{U}_s vs. R_e at different values of \bar{r} for a sphere with $\bar{a} = 0.15$.

Power law correlations arise from the straight lines in log-log plots for $\bar{\Omega}_s$ and \bar{U}_s

$$\bar{U}_s(\bar{r}, R_e, \bar{a}) = b(\bar{r}, \bar{a}) R_e^{m(\bar{r}, \bar{a})}, \quad (4.8)$$

$$\overline{\Omega}_s(\bar{r}, R_e, \bar{a}) = c(\bar{r}, \bar{a}) R_e^{n(\bar{r}, \bar{a})}. \quad (4.9)$$

The coefficients b , m , c , and n are obtained for a particle with $\bar{a} = 0.15$ in the range $0.1 \leq \bar{r} \leq 0.8$ and plotted in figure E-10. Exponential fitting and linear fitting may give reasonable approximations to the prefactors b and c and exponents m and n , respectively:

$$b = 1.1 \times 10^{-2} \exp(2.2\bar{r}), \quad c = 2.3 \times 10^{-5} \exp(8.8\bar{r}); \quad (4.10)$$

$$m = -1.1\bar{r} + 1.6, \quad n = -2.1\bar{r} + 2.7. \quad (4.11)$$

Substitution of (4.10) and (4.11) into (4.8) and (4.9) leads to explicit expressions for \overline{U}_s and $\overline{\Omega}_s$

$$\overline{U}_s = 1.1 \times 10^{-2} \exp(2.2\bar{r}) R_e^{-1.1\bar{r}+1.6}, \quad (4.12)$$

$$\overline{\Omega}_s = 2.3 \times 10^{-5} \exp(8.8\bar{r}) R_e^{-2.1\bar{r}+2.7}, \quad (4.13)$$

which apply to a particle with $\bar{a} = 0.15$ in the range $0.1 \leq \bar{r} \leq 0.8$. Correlation (4.12) and (4.13) are generally valid in the range of $1 \leq R_e \leq 45$. However, correlation (4.12) is not in good agreement with the data for \overline{U}_s on the second negative-slope branch on the \overline{L} vs. \bar{r} curve ($0.5 \leq \bar{r} \leq 0.65$) at high Reynolds numbers ($R_e = 27, 36$ and 45). Thus correlation (4.12) in the range $0.5 \leq \bar{r} \leq 0.65$ is valid only for $1 \leq R_e \leq 22.5$.

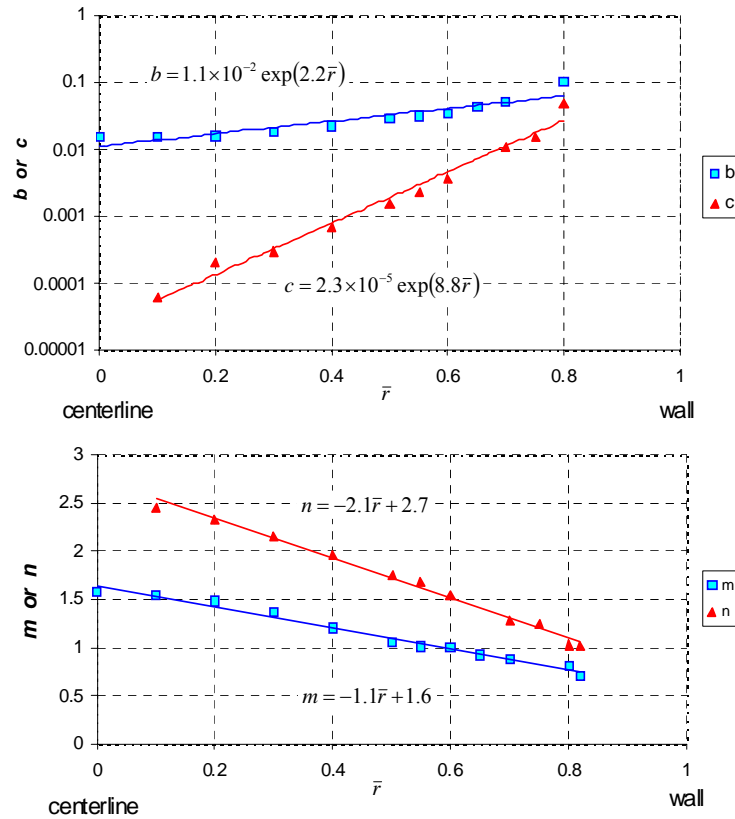


Figure E-10. The prefactors b and c and exponents m and n in correlations (4.8) and (4.9) for a particle with $\bar{a} = 0.15$ in the range $0.1 \leq \bar{r} \leq 0.8$.

Correlations for \bar{U}_s and $\bar{\Omega}_s$ for $\bar{a} = 0.1$ are developed using the same procedure as for $\bar{a} = 0.15$. We omit the details of derivation and only give the final formulas for \bar{U}_s and $\bar{\Omega}_s$

$$\bar{U}_s = 8.3 \times 10^{-3} \exp(1.8\bar{r}) R_e^{-1.4\bar{r}+1.9}, \quad (4.14)$$

$$\bar{\Omega}_s = 7.7 \times 10^{-6} \exp(9.0\bar{r}) R_e^{-3.3\bar{r}+3.8}, \quad (4.15)$$

which apply to a particle with $\bar{a} = 0.1$ in the range $0.05 \leq \bar{r} \leq 0.85$. The range of the Reynolds number in which (4.14) and (4.15) is valid is $1 \leq R_e \leq 12$.

4.3. Correlations for the particle parameters at equilibrium

The equilibrium state of a particle is always the focus of the study of particle migration. We obtain the particle parameters at stable equilibrium, such as the equilibrium position \bar{r}_e , the slip velocity U_{se} and the slip angular velocity Ω_{se} by unconstrained simulation and find that they may be correlated to the Reynolds number. We summarize the particle parameters at stable equilibrium in table E-3.

\bar{a}	R_e	\bar{U}_m	\bar{r}_e	$\bar{\Omega}_{se}$	\bar{U}_{se}
0.05	2	100	0.731	0.00710	0.0247
0.1	1	12.5	0.603	0.00188	0.0219
	2	25	0.608	0.00509	0.0444
	4	50	0.638	0.0209	0.0901
	6	75	0.661	0.0498	0.152
	8	100	0.674	0.0901	0.470
	10	125	0.684	0.139	0.712
	12	150	0.708	0.202	0.296
0.15	1	5.56	0.573	0.00354	0.0338
	2	11.1	0.573	0.00765	0.0675
	9	50	0.601	0.0861	0.306
	13.5	75	0.623	0.197	0.482
	18	100	0.642	0.342	0.730
	22.5	125	0.657	0.513	0.785
	27	150	0.670	0.705	1.07
	36	200	0.691	1.16	1.18
	45	250	0.700	1.67	1.74
0.2	32	100	0.598	0.793	1.74
0.25	50	100	0.567	1.49	2.84

Table E-3. Particle parameters at stable equilibrium: the equilibrium position \bar{r}_e , the dimensionless slip angular velocity $\bar{\Omega}_{se} = \rho_f \Omega_{se} (2a)^2 / \mu$ and the dimensionless slip velocity $\bar{U}_{se} = \rho_f U_{se} (2a) / \mu$.

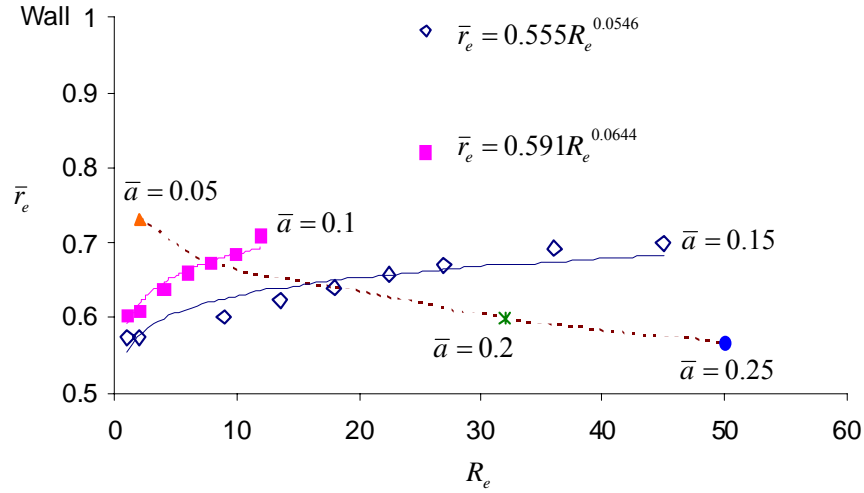


Figure E-11. The stable equilibrium position \bar{r}_e of a neutrally buoyant sphere as a function of the Reynolds number. The two power law curves are for spheres with $\bar{a} = 0.10$ and $\bar{a} = 0.15$ respectively. All the points on the dotted line are for the same flow Reynolds number $\bar{U}_m = 100$; the dotted line shows that when \bar{U}_m is fixed, the equilibrium position becomes closer to the centerline as \bar{a} increases.

We can correlate the stable equilibrium position of a neutrally buoyant sphere with the Reynolds number (see figure E-11):

$$\bar{r}_e = 0.591R_e^{0.0644} \quad \text{for } \bar{a} = 0.1; \quad (4.16)$$

$$\bar{r}_e = 0.555R_e^{0.0546} \quad \text{for } \bar{a} = 0.15. \quad (4.17)$$

The equilibrium position \bar{r}_e moves closer to the wall as the Reynolds number increases. We also observe that when the flow Reynolds number \bar{U}_m is fixed, the larger particle finds its equilibrium position closer to the centerline than the smaller particle. The above observations are in agreement with the experiments by Karnis, Goldsmith and Mason (1966), who reported that neutrally buoyant particles stabilized closer to the wall for larger flow rates and closer to the center for larger particles.

Matas, Morris and Guazzelli (2004) reported that for neutrally buoyant spheres with a diameter $d = 900 \mu\text{m}$ in the pipe of diameter $D = 8 \text{ mm}$, the equilibrium position is $\bar{r}_e = 0.64 \pm 0.04$ for $\bar{U}_m = 60$ and $\bar{r}_e = 0.78 \pm 0.04$ for $\bar{U}_m = 350$. The value of \bar{a} is close to 0.1 in these experiments, thus we can compare correlation (4.16) to the experimental results. Equations (4.16) and (2.15) predict $\bar{r}_e = 0.654, 0.732$ for $\bar{U}_m = 60, 350$ respectively, in good agreement

with the experimental results. Matas, Morris and Guazzeli (2004) stated that the matched asymptotic calculation (Schonberg & Hinch 1989, Asmolov 1999) predicts that $\bar{r}_e = 0.71, 0.85$ for $\bar{U}_m = 60, 350$ respectively, in both cases larger than the experimental value. They attributed this difference to the relatively large size of the particles. They reported that when smaller particles (200 μm) were used in the experiments, equilibrium positions were closer to the theoretical predictions. The actual values of \bar{r}_e for 200 μm particles are not reported in their paper, but we can infer that \bar{r}_e for 200 μm particles is larger than \bar{r}_e for 900 μm particles at the same \bar{U}_m . This agrees with our conclusion that the larger particle finds its equilibrium position closer to the centerline than the smaller particle at a fixed \bar{U}_m .

If we correlate the dimensionless slip angular velocity at equilibrium $\bar{\Omega}_{se}$ with the Reynolds number R_e , we obtain (see figure E-12)

$$\bar{\Omega}_{se} = 0.0023R_e^{1.72} \quad \text{i.e.} \quad \Omega_{se} = 0.0023R_e^{1.72} \mu / (\rho_f 4a^2). \quad (4.18)$$

This correlation appears to be applicable to a wide range of the radius ratio: $0.05 \leq \bar{a} \leq 0.25$. Correlation (4.18) is important because it gives explicitly the slip angular velocity when the particle is at stable equilibrium.

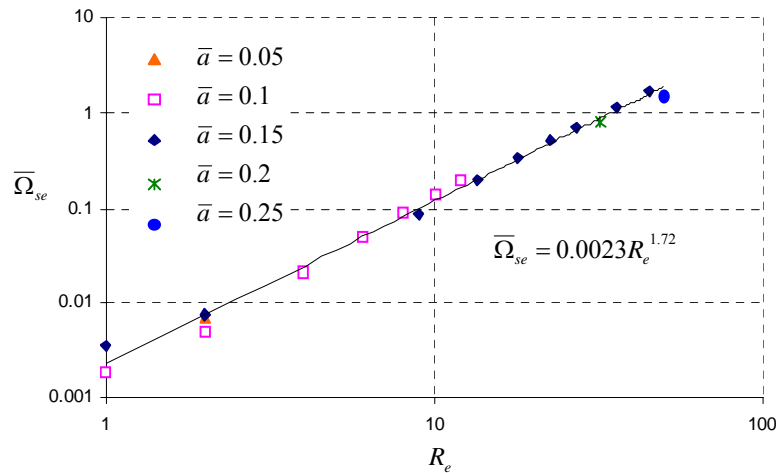


Figure E-12. The correlation between $\bar{\Omega}_{se}$ and the Reynolds number R_e .

Now with all the correlations for k , \bar{U}_s , $\bar{\Omega}_s$, and $\bar{\Omega}_{se}$ available, we are at a position to make the lift correlation (4.2) completely explicit. Take a particle with $\bar{a} = 0.15$ for example,

$$\bar{L} = k\bar{U}_s(\bar{\Omega}_s - \bar{\Omega}_{se}), \quad (4.19)$$

where k , \bar{U}_s , $\bar{\Omega}_s$, and $\bar{\Omega}_{se}$ are given in (4.4), (4.12), (4.13) and (4.18) respectively. Therefore, we are able to compute the lift force on a particle at different radial positions from the Reynolds number and radius ratio. It should be noted that the lift force applies to a freely rotating particle translating at a steady speed.

If we set \bar{L} in (4.19) to zero, we can solve for the equilibrium position \bar{r}_e . The value $\bar{L} = 0$ is given by $\bar{\Omega}_s = \bar{\Omega}_{se}$; this leads to a formula for the equilibrium position

$$\bar{r}_e = \frac{4.6 - 0.98 \ln R_e}{8.8 - 2.1 \ln R_e}, \tag{4.20}$$

for a particle with $\bar{a} = 0.15$ which can be compared to correlation (4.17). Formula (4.17) and (4.20) give rise to similar values for \bar{r}_e in the range $1 \leq R_e \leq 22.5$ (see figure E-13); (4.17) gives a better approximation to the simulation results because it is directly developed for \bar{r}_e . When $R_e > 22.5$, the agreement is not good between (4.17) and (4.20).

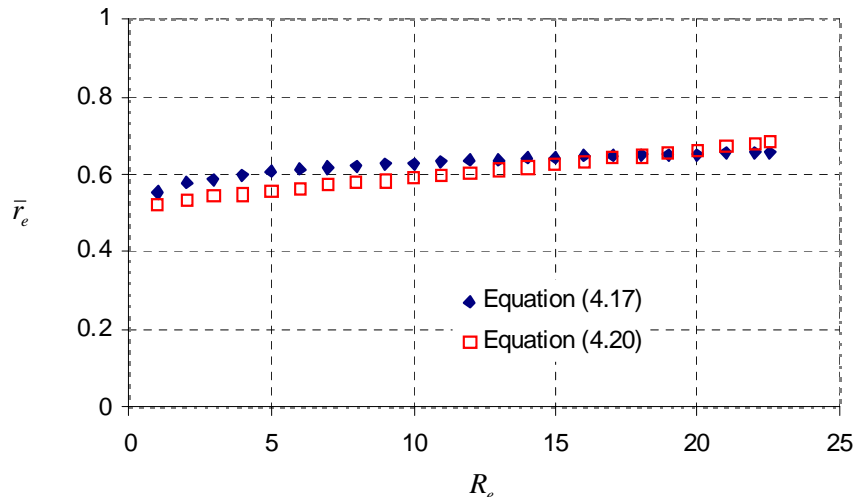


Figure E-13. The values of \bar{r}_e computed by equations (4.17) and (4.20) in the range $1 \leq R_e \leq 22.5$ for $\bar{a} = 0.15$.

A summary of our correlations is presented in Table E-4 below. Correlation formula exhibiting the dependence of prefactors and exponents on \bar{a} requires more computation.

$\bar{L}(\bar{r}; \bar{a}, R_e) = k(\bar{a}, R_e) \bar{U}_s (\bar{\Omega}_s - \bar{\Omega}_{se})$	Lift Law		
Find k			
$k(\bar{a}, R_e) = g(\bar{a}) R_e^{-h(\bar{a})}$	\bar{a}	$g(\bar{a})$	$h(\bar{a})$
	0.1	809	0.604
	0.15	450	0.658

$\bar{U}_s = b(\bar{r}; \bar{a}) R_e^{m(\bar{r}; \bar{a})}$			
$\bar{U}_s = 1.1 \times 10^{-2} \exp(2.2\bar{r}) R_e^{-1.1\bar{r}+1.6}$		for $\bar{a} = 0.15$	
$\bar{U}_s = 8.3 \times 10^{-3} \exp(1.8\bar{r}) R_e^{-1.4\bar{r}+1.9}$		for $\bar{a} = 0.1$	
$\bar{\Omega}_{se} = 0.0023 R_e^{1.72}$		$0.05 \leq \bar{a} \leq 0.25$	
applicable to a wide range of \bar{a}			
$\bar{r}_e = f(\bar{a}) R_e^{q(\bar{a})}$	\bar{a}	$f(\bar{a})$	$q(\bar{a})$
	0.1	0.591	0.0644
	0.15	0.555	0.0546

Table E-4. Structure of the correlations for the lift law

5. Comparison of lift expressions

Wang and Joseph (2003) compared the lift correlation (4.7) with analytical lift expressions in the literature. Their comparison was limited because the correlation (4.7) is for a two-dimensional cylindrical particle whereas the lift expressions of Saffman (1965, 1968) and Auton (1987) are for a sphere. A comparison between correlations (4.5) and (4.6) with the aforementioned analytical lift expressions is more sensible; though the comparison is still tentative because the analytical lift expressions are for a particle in a linear shear flow on an unbounded domain whereas our 3D simulation is in a tube Poiseuille flow. We will compare the correlation (4.5) to the analytical lift expressions with these caveats in mind.

Auton (1987) derived a lift expression for a fixed sphere in an inviscid fluid in which uniform motion is perturbed by a weak shear:

$$\mathbf{L} = \frac{2}{3} \pi a^3 \rho \boldsymbol{\omega} \times (\mathbf{u} - \mathbf{U}). \quad (5.1)$$

In the case under consideration, $\boldsymbol{\omega} = \mathbf{e}_z \dot{\gamma}$ and $\mathbf{u} - \mathbf{U} = \mathbf{e}_x U_s$; the lift force in y direction is

$$L = \frac{2}{3} \pi a^3 \rho U_s \dot{\gamma}, \quad (5.2)$$

which is similar to our correlation (4.5) but differs from them in several ways: (5.2) has a constant prefactor for inviscid fluids whereas viscous effects enter into (4.5) through R_e ; the lift force depends on $\dot{\gamma}$ in (5.2) but on the discrepancy $\Omega_s - \Omega_{se}$ in (4.5); (5.2) is for a fixed 3D sphere while (4.5) is for a freely rotating sphere with zero acceleration.

Saffman 1965, 1968 obtained an expression for the lift force on a rotating sphere in an unbounded linear shear flow at indefinitely small Reynolds number:

$$L = 6.46 \rho_f^{0.5} \mu^{0.5} U_s \dot{\gamma}^{0.5} a^2 + \text{lower order terms} . \quad (5.3)$$

If we make following changes in equation (4.5): $R_e = \rho_f \dot{\gamma}_w (2a)^2 / \mu$, the power of R_e (-0.604) \rightarrow (-0.5), then equation (4.5) becomes:

$$L = 1696 \rho_f^{0.5} \mu^{0.5} U_s \dot{\gamma}_w^{-0.5} (\Omega_s - \Omega_{se}) a^2 . \quad (5.4)$$

Comparing (5.4) and the leading term in (5.3), we note that both expressions are linear in U_s ; both have a similar dependence on ρ_f , μ , and a . However, the dependence on $\dot{\gamma}$ and $\Omega_s - \Omega_{se}$ is greatly different.

For a neutrally buoyant particle at equilibrium, $L = 0$ and equations (5.2) and (5.3) imply $U_s = 0$. The Auton and Saffman formulas thus predict that the slip velocity is zero for a neutrally buoyant sphere at equilibrium.

McLaughlin (1991) generalized Saffman's analysis to remove the restriction that the Reynolds number \bar{U}_s based on slip velocity U_s is much smaller than the square root of the Reynolds number R_e based on the shear rate and derived an expression for the lift force:

$$L = \frac{6.46}{2.255} \rho_f^{0.5} \mu^{0.5} U_s \dot{\gamma}^{0.5} a^2 J(\varepsilon), \quad (5.5)$$

where

$$\varepsilon = \frac{\sqrt{R_e}}{\bar{U}_s}, R_e = \frac{\rho_f \dot{\gamma} (2a)^2}{\mu}, \bar{U}_s = \frac{\rho_f U_s 2a}{\mu}$$

and J is a function of ε only and has a value of 2.255 as $\varepsilon \rightarrow \infty$ (the Saffman limit). Equation (5.5) shows that zero lift force is obtained when $U_s = 0$ or $J(\varepsilon) = 0$. The solution provided by McLaughlin gives $J(\varepsilon) = 0$ at $\varepsilon = 0.215$, i.e., $\bar{U}_s = \sqrt{R_e} / 0.215$. Hence, U_s is not single valued for $L = 0$.

In the lift expressions given by Auton, Saffman, and McLaughlin, zero lift force is determined by the slip velocity U_s . This is not the case in our simulation for a sphere in tube Poiseuille flows; our results show that $\Omega_s = \Omega_{se}$ gives rise to zero lift. The difference may be due to the fact that linear shear flow has a zero shear gradient whereas the shear gradient in Poiseuille flow is a constant and not small.

6. Conclusion and discussion

- The motion of a single neutrally buoyant rigid sphere in tube Poiseuille flow is simulated by two methods: (1) an ALE arbitrary Lagrangian-Eulerian scheme with a moving adaptive mesh and (2) a DLM distributed Lagrange multiplier / fictitious domain method. The two methods give the same results, and the simulation agrees with experiments.
- A lift law $L = CU_s(\Omega_s - \Omega_{se})$ analogous to $L = \rho U \Gamma$ of classical aerodynamics which was proposed and validated in two dimensions is validated in three dimensions here; U_s is the slip velocity and it is positive, Ω_s is the slip angular velocity and Ω_{se} is the slip angular velocity when the sphere is in equilibrium at the Segré-Silberberg radius.
- The slip angular velocity discrepancy $\Omega_s - \Omega_{se}$ is the circulation for the free particle and it is shown to change sign with the lift.
- Numerical experiments using the method of constrained simulation generated data for the lift force and velocities of a freely rotating sphere in steady flows arising from initial value problems in which the sphere is constrained to move at a fixed radius.
- Constrained simulations are very efficient. The lift and all velocities are obtained for different radii at each specified Reynolds number and radius ratio $\bar{a} = a/R$.
- Equilibrium may be identified at the Segré-Silberberg radius at which the lift vanishes (for a neutrally buoyant particle). The equilibrium slip angular velocity is the slip angular velocity at this equilibrium radius.
- Data generated by constrained simulations are processed for straight lines in log-log plots and give rise to get explicit power-law formula for all the quantities in the lift law as a function of R_e and \bar{a} . We go from data to formulas.
- The equilibrium position (the Segré-Silberberg radius) moves towards the wall as R_e increases at each fixed \bar{a} ; it moves towards the centerline as \bar{a} increases at a fixed flow Reynolds number \bar{U}_m .

- Our correlations are compared with analytical lift formulas in the literature. None of the analytic formulas for lift change sign at Segré-Silberberg radius. These formulas also leave the form of the slip velocity U_s obscure.

The lift law we have proposed for free circular and spherical particles is analogous to the aerodynamic lift law $\rho U \Gamma$ in the case of a rotating circle for which $\Gamma = 2\pi a^2 \Omega$. It is probable that the lift law for free bodies of more general shape is in the form $L = C U_s \Gamma_s$ where C depends on fluid properties and geometric parameters and Γ_s is unknown. The determination of Γ even in aerodynamic theory is a complicated problem. In airfoil theory, Γ is strongly coordinated with the attack angle of the airfoil. A similar coordination of the circulation with the attack angle is apparently generated by the motion of a free ellipse in a plane Poiseuille flow (Feng, Huang and Joseph, 1995). This problem could be framed in terms of the equilibrium position and orientation of an ellipse in a plane Poiseuille flow. As in the case of circular particles, the equilibrium position is decided by a balance of buoyant weight and lift, where the lift arises as a competition of forces arising from shear gradients and wall effects. This problem ought to be studied by the technique of constrained simulation discussed here. At each fixed y , the motion of the ellipse would evolve to a steady state with a fixed angle of attack. This lift on the ellipse at this y could be computed and, of course, as in the case of circular and spherical particles, this lift would balance the buoyant weight, zero for neutrally buoyant particles, at equilibrium, with a certain equilibrium attack angle. The lift must change sign with the attack angle discrepancy.

This paper aims at presenting a general procedure and data structure for the interrogation of numerical simulation data. Our goal is to draw explicit formulas from numerical data, which may be used to model complex problems, obviating further expensive computation. The procedure involves identifying controlling dimensionless groups and data fitting analyses which lead to expressions for the quantities of interest in terms of prescribed parameters. We believe when properly used, this procedure may help to reveal the underlying physics of the problem and generate practically useful formulas at the same time.

Acknowledgement

This work was partially supported by the National Science Foundation KDI/New Computational Challenge grant (NSF/CTS-98-73236); by the DOE, Department of Basic Energy Sciences; by a grant from the Schlumberger foundation; from STIM-LAB Inc.; and by the Minnesota Supercomputer Institute.

References

- Asmolov, E. S. 1999 The inertial lift on a spherical particle in a plane Poiseuille flow at large channel Reynolds number. *J. Fluid Mech.* **381**, 63 – 87.
- Auton, T.R. 1987 The lift force on a spherical body in a rotational flow, *J. Fluid Mech.* **183**, 199 - 218.
- Bretherton, F.P. 1962 Slow viscous motion round a cylinder in a simple shear, *J. Fluid Mech.* **12**, 591 - 613.
- Choi, H.G. and Joseph, D.D. 2001 Fluidization by lift of 300 circular particles in plane Poiseuille flow by direct numerical simulation, *J. Fluid Mech.* **438**, 101 - 128.
- Feng, J., Hu, H.H. and Joseph, D.D. 1994 Direct simulation of initial value problems for the motion of solid bodies in a Newtonian fluid. Part 2: Couette and Poiseuille flows, *J. Fluid Mech.* **277**, 271 - 301.
- Feng, J., Huang, P.Y. and Joseph, D.D. 1995. Dynamic simulation of the motion of capsules in pipelines, *J. Fluid Mech.* **286**, 201-227.
- Glowinski, R. 2003 Chapters 8 and 9 of *Finite element methods for incompressible viscous flow*. In *Handbook of Numerical Analysis*, Vol. IX, P.G. Ciarlet and J.L. Lions, eds., North-Holland, Amsterdam, pp. 3-1176.
- Glowinski, R., Pan, T-W., Hesla, T.I. and Joseph, D.D. 1999 A distributed Lagrange multiplier/fictitious domain method for particulate flows. *Int. J. Multiphase Flow*, **25**, 755-794.
- Glowinski, R., Pan, T-W., Hesla, T.I, Joseph, D.D, and Periaux, J. 1999 A distributed Lagrange multiplier/fictitious domain method for flow around moving rigid bodies: Application to particulate flow, *Int. J. Numer. Meth. Fluids*, **30**, 1043-1066.
- Glowinski, R., Pan, T-W., Hesla, T.I, Joseph, D.D, and Periaux, J., 2001 A fictitious domain approach to the direct numerical simulation of incompressible fluid flow past moving rigid bodies: Application to particulate flow, *J. Comp. Phys.*, **162**, 363-426.
- Glowinski, R., Pan, T-W. and Periaux, J. 1998 Distributed Lagrange multiplier methods for incompressible viscous flow around moving rigid bodies. *Comp. Math. Appl. Mech. Eng.* **151**, 181-194.
- Goldsmith, H.L. and Mason, S.G. 1967 "Chapter 4. The Microrheology of Dispersions," in F.R. Eirich, ed., *Rheology: Theory and Applications*, Volume IV, *Academic Press*, NY, pp. 87-205.
- Hu, H.H., Joseph, D.D. and Crochet, M.J. 1992 Direct simulation of fluid particle motions. *Theor. Comput. Fluid Dyn.* **3**, 285 - 306.
- Joseph, D.D. and Ocando, D. 2002 Slip Velocity and Lift, *J. Fluid Mech.* **454**, 263 - 286.
- Karnis, A., Goldsmith, H.L. and Mason, S.G. 1966 The flow of suspensions through tubes. Part 5: Inertial effects. *Can. J. Chem. Engng.* **44**, 181.
- Matas, J. P., Morris, J. F. and Guazzelli, E. 2004 Lateral forces on a sphere. *Oil & Gas Science and Technology – Rev.* **59(1)**, 59 – 70.
- McLaughlin, J.B. 1991 Inertial migration of a small sphere in linear shear flows, *J. Fluid Mech.* **224**, 261 - 274.
- Patankar, N.A., Huang, P.Y., Ko, T. and Joseph, D.D. 2001 Lift-off of a single particle in Newtonian and viscoelastic fluids by direct numerical simulation, *J. Fluid Mech.* **438**, 67 - 100.
- Patankar, N.A., Ko, T., Choi, H.G. and Joseph, D.D. 2001 A correlation for the lift-off of many particles in plane Poiseuille of Newtonian fluids, *J. Fluid Mech.* **445**, 55 - 76.

- Rubinow, S.I. and Keller, J.B. 1961 The transverse force on a spinning sphere moving in a viscous fluid. *J. Fluid Mech.* **11**, 447 - 459.
- Saffman, P.G. 1965 The lift on a small sphere in a slow shear flow, *J. Fluid Mech.* **22**, 385 - 400; and Corrigendum, 1968 *J. Fluid Mech.* **31**, 624.
- Schonberg, J. A. & Hinch, E. J. 1989 Inertial migration of a sphere in Poiseuille flow. *J. Fluid Mech.* **203**, 517 – 524.
- Segrè G. and Silberberg, A. 1961 Radial Poiseuille flow of suspensions, *Nature*, **189**, 209.
- Segrè G. and Silberberg, A. 1962 Behavior of macroscopic rigid spheres in Poiseuille flow: Part I, *J. Fluid Mech.* **14**, 136 - 157.
- Singh, P., Joseph, D.D., Hesla, T.I., Glowinski, R. and Pan, T-W. 2000 A distributed Lagrange multiplier/fictitious domain method for viscoelastic particulate flows. *J. Non-Newtonian Fluid Mech.* **91**, 165-188.
- Wang, J. and Joseph, D.D. 2003 Lift forces on a cylindrical particle in plane Poiseuille flow of shear thinning fluids. *Physics Fluids.* **15**, 2267-2278.
- Zhu, M-Y. 2000 Direct numerical simulation of the solid-liquid flows of Newtonian and viscoelastic fluids. Ph.D. thesis, University of Pennsylvania.

E. Addendum to Chapter XI (Addendum E): Lift Force on a Sphere in tube flow

(from the paper: Migration of a sphere in tube flow B.H. Yang, J. Wang, D.D. Joseph, H.H. Hu, T-W. Pan and R. Glowinski, *J. Fluid Mech.*, 2005)

Abstract

The cross stream migration of a single neutrally buoyant rigid sphere in tube flow is simulated by two packages, one (ALE) based on a moving and adaptive grid and another (DLM) using distributed Lagrange multipliers on a fixed grid. The two packages give results in good agreement with each other and with experiments. A lift law $L = CU_s(\Omega_s - \Omega_{se})$ analogous to $L = \rho UT$ which was proposed and validated in two dimensions is validated in three dimensions here; C is a constant depending on material and geometric parameters, U_s is the slip velocity and it is positive, Ω_s is the slip angular velocity and Ω_{se} is the slip angular velocity when the sphere is in equilibrium at the Segrè-Silberberg radius. The slip angular velocity discrepancy $\Omega_s - \Omega_{se}$ is the circulation for the free particle and it changes sign with the lift. A method of constrained simulation is used to generate data which is processed for correlation formulas for the lift force, slip velocity, and equilibrium position. Our formulas predict the change of sign of the lift force which is necessary in the Segrè-Silberberg effect. Our correlation formula is compared with analytical lift formulas in the literature and with the results of two-dimensional simulations. Our work establishes a general procedure for obtaining correlation formulas from numerical experiments. This procedure forms a link between numerical simulation and engineering practice.

1. Introduction

Migration and equilibrium of solid particles in shear flows have always been of great interest for researchers. Segrè and Silberberg (1961, 1962) studied the migration of dilute suspensions of neutrally buoyant spheres in tube flows and found the particles migrate away from both the wall and the centerline and accumulate at a radial position of about 0.6 times the tube radius. This remarkable Segrè-Silberberg effect has been verified by many experimental works on the same kind of problems. For example, Goldsmith and Mason (1962) observed that a rigid particle stayed at the initial radial position at very small Reynolds numbers and migrated to intermediate positions at finite Reynolds numbers. Karnis, Goldsmith and Mason (1966) reported that neutrally buoyant particles stabilized midway between the centerline and the wall, closer to the wall for larger flow rates and closer to the center for larger particles.

In an attempt to explain the Segrè-Silberberg effect, different analytical expressions for the lift force which causes the particle to migrate transversely were obtained in the literature (Rubinow and Keller 1961, Bretherton 1962, Saffman 1965, 1968, McLaughlin 1991, and Auton 1987 among others). These analytical expressions are based on perturbing Stokes flow with inertia or on perturbing potential flow with a little vorticity. They are explicit and valuable; however, the restrictions on the perturbation analyses make it difficult to apply these expressions to practical problems where the Reynolds number is finite and viscosity is important.

Schonberg & Hinch (1989) analyzed the lift on a neutrally buoyant small sphere in a plane Poiseuille flow, with the channel Reynolds number $R_c = U'_m l / \nu$ less than approximately 100, using matched asymptotic methods. Here U'_m is the maximum velocity of a channel flow, and l is the channel width. The same problem for neutrally buoyant and non-neutrally buoyant small spheres has been studied by Asmolov (1999). He considered the Reynolds number based on the particle size to be asymptotically small while the channel Reynolds number is finite. He computed the lift force on a sphere as a function of the distance from the wall to the sphere center for flows with R_c up to 3000; the results show that the equilibrium position moves towards the wall as R_c increases. When the particle Reynolds number is small, the disturbance flow due to the particle is governed by creeping-flow equations to leading order; one can compute the transverse component of the velocity at the particle center and use the Stokes drag law to calculate the lift. The analysis takes the effect of inertia $(\mathbf{u} \cdot \nabla)\mathbf{u}$ into account only in an Oseen linear system. The analysis is heavy and explicit formulas for the lift are not obtained.

Feng, Hu and Joseph (1994) performed numerical simulations of the motion of a two-dimensional circular particle in Couette and Poiseuille flows. Patankar, Huang, Ko and Joseph (2001) and Joseph and Ocando (2002) simulated the motion of a two-dimensional circular particle in plane Poiseuille flows perpendicular to gravity in Newtonian and viscoelastic fluids. They showed that multiple equilibrium states exist for particles with intermediate densities; these equilibrium states can be stable or unstable.

Relative motions between the fluid and the particle, which may be characterized by slip velocities, are essential to understand the lift force on the particle. We use U_p and Ω_p to denote the translational and angular velocities of the particle at steady state and the slip velocities are defined as:

$$U_s = U_f - U_p, \text{ the slip velocity;} \quad (1.1)$$

$$\Omega_s = \Omega_p - \Omega_f = \Omega_p + \dot{\gamma}/2, \text{ the slip angular velocity,} \quad (1.2)$$

where U_f and $\dot{\gamma}$ are the fluid velocity and local shear rate evaluated at the location of the particle center in the undisturbed flow. Joseph and Ocando (2002) found that the discrepancy $\Omega_s - \Omega_{se}$, where Ω_{se} is the slip angular velocity at equilibrium, changes sign across the equilibrium position just as the lift force does. Thus, this discrepancy can be used to account for the migration toward the intermediate equilibrium position from the centerline and the wall (the Segrè-Silberberg effect).

Following Joseph and Ocando's analysis, Wang and Joseph (2003) constructed correlations for the lift force by analogy with the classical lift formula $L = \rho U \Gamma$ of aerodynamics; they showed that the proper analogs of U and Γ were U_s and $\Omega_s - \Omega_{se}$. Their correlations apply to a freely rotating two-dimensional circular particle without accelerations in a plane Poiseuille flow. They also demonstrated that the correlations for lift force could be made completely explicit provided that the correlations relating U_s and Ω_s to prescribed parameters were obtained.

The results from two-dimensional simulations presented by Feng, Hu and Joseph (1994), Patankar *et al.* (2001), Joseph and Ocando (2002) and Wang and Joseph (2003) are difficult to compare with experimental results because the majority of the experiments are for spherical particles in circular tube flows. The lift force correlations by Wang and Joseph are for circular particles and can not be rigorously compared to analytical lift expressions for spheres. All the above mentioned authors used a two-dimensional finite element scheme based on unstructured body-fitted moving grids first developed by Hu, Joseph and Crochet (1992). Recently, Hu and Zhu extended the two-dimensional scheme to three-dimensional and performed simulations of the migration of spheres in tube Poiseuille flows (see the PhD thesis of Zhu 2000). We call this scheme the ALE code because an arbitrary Lagrangian-Eulerian moving mesh technique has been adopted to deal with the motion of the particles. The three-dimensional ALE scheme is used in the current work to study the lift force on a neutrally buoyant sphere in tube Poiseuille flow.

Another approach to simulate the solid-liquid flow initiated by us is based on the principle of embedded or fictitious domains. In this approach, the Navier-Stokes equations are solved everywhere, including inside the particles. The flow inside the particles is forced to be a rigid body motion by a distribution of Lagrange multipliers – thus we call this scheme the DLM code. Detailed descriptions of the DLM method can be found in Glowinski, Pan, and Periaux (1998); Glowinski, Pan, Hesla, and Joseph (1999); Glowinski, Pan, Hesla, Joseph, and Periaux (1999, 2001); Singh, Joseph, Hesla, Glowinski and Pan (2000) and Glowinski (2003). The two quite different schemes, the DLM code and the ALE code, are both employed to simulate the motion of a neutrally buoyant sphere in tube Poiseuille flow in the current work. We shall show that the

results of the two codes are in good agreement, which provides strong support for the credibility of our numerical simulation.

The main goal of this work is to extend the correlation of the lift force in terms of U_s and the discrepancy $\Omega_s - \Omega_{se}$ to three-dimensional cases, which would give a more convincing explanation for the Segrè-Silberberg effect. The lift force correlations represent efforts to draw explicit formulas from numerical simulation data. There is no reason why “empirical” formulas of the type used in engineering which correlate experimental data cannot be generated from the data produced by numerical simulations. Correlations have already been obtained for single particle lift (Patankar *et al.* 2001, Wang and Joseph 2003) and for the bed expansion of many particles (Choi and Joseph 2001, Patankar, Ko, Choi and Joseph 2001) by processing numerical data. Our works have establish general rules for the interrogation of data from numerical simulation to be used in developing models for complex fluid dynamics problems such as the fluidization by lift or drag.

2. Governing equations and dimensionless parameters

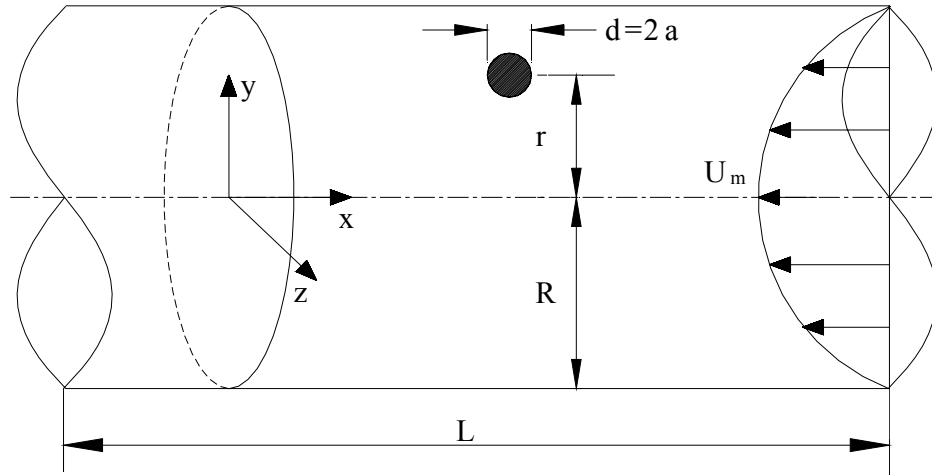


Figure E-1. Sketch for the problem of a rigid sphere in a tube Poiseuille flow. The sphere is neutrally buoyant and the orientation of the gravity is irrelevant.

The governing equations for the incompressible Newtonian fluid are

$$\nabla \cdot \mathbf{u} = 0 \text{ and } \rho_f \left(\frac{\partial \mathbf{u}}{\partial t} + (\mathbf{u} \cdot \nabla) \mathbf{u} \right) = -\nabla P + \rho_f \mathbf{g} + \mu \nabla^2 \mathbf{u} \quad (2.1)$$

where $\mathbf{u}(\mathbf{x}, t)$ is the fluid velocity, ρ_f is the fluid density, $P(\mathbf{x}, t)$ is the pressure, \mathbf{g} is the gravitational acceleration, and μ is the fluid viscosity. We can absorb the gravity term in the Navier-Stokes equations into the pressure by decomposing the pressure as

$$\mathbf{P} = p + \rho_f \mathbf{g} \cdot \mathbf{x}. \quad (2.2)$$

The equations of motion of the solid particles in a general three-dimensional case are

$$\begin{aligned} m \frac{d\mathbf{U}_p}{dt} &= m\mathbf{g} + \int [-\mathbf{P}\mathbf{1} + \boldsymbol{\tau}] \cdot \mathbf{n} d\Gamma, \\ \frac{d(\mathbf{I} \cdot \boldsymbol{\Omega}_p)}{dt} &= \int (\mathbf{x} - \mathbf{X}_p) \times ([-\mathbf{P}\mathbf{1} + \boldsymbol{\tau}] \cdot \mathbf{n}) d\Gamma, \end{aligned} \quad (2.3)$$

where m is the mass of the particle, \mathbf{U}_p is the translational velocity, $\boldsymbol{\Omega}_p$ is the angular velocity, \mathbf{I} is the moment of inertia tensor and \mathbf{X}_p is the coordinate of the center of mass of the particle. We consider a solid sphere with a radius a and $m = \rho_p 4\pi a^3 / 3$, $\mathbf{I} = \text{diag}(2ma^2/5)$. The no-slip condition is imposed on the particle boundaries

$$\mathbf{u} = \mathbf{U}_p + \boldsymbol{\Omega}_p \times (\mathbf{x} - \mathbf{X}_p) \quad (2.4)$$

and on the tube wall $\mathbf{u} = 0$. The velocity profile at the inlet of the tube is prescribed by

$$u = U_m (1 - r^2 / R^2), \quad (2.5)$$

where U_m is the maximum velocity at the centerline of the tube; r is the radial position and R is the radius of the tube. The traction-free boundary condition is imposed at the outlet of the tube:

$$f_n \equiv \mathbf{n} \cdot \mathbf{T} \cdot \mathbf{n} = 0; \quad u_y = 0; \quad u_z = 0, \quad (2.6)$$

where $\mathbf{T} = -\mathbf{P}\mathbf{1} + \boldsymbol{\tau}$ is the total stress tensor and \mathbf{n} is the norm at the outlet of the tube.

The undisturbed tube Poiseuille flow without particles is given by (2.5). The shear rate at the wall ($r = R$) is given by $\dot{\gamma}_w = 2U_m / R$. To non-dimensionalize the governing equations, we use the velocity $V = 2a\dot{\gamma}_w$ as the characteristic velocity, $2a$ for length, $2a/V$ for time, $\mu V / 2a$ for stress and pressure, and $\dot{\gamma}_w$ for angular velocity. The dimensionless equations are (we use the same symbols for dimensionless variables)

$$\nabla \cdot \mathbf{u} = 0, \quad (2.7)$$

$$R_e \left(\frac{\partial \mathbf{u}}{\partial t} + (\mathbf{u} \cdot \nabla) \mathbf{u} \right) = -\nabla p + \nabla^2 \mathbf{u}, \quad (2.8)$$

$$\begin{aligned} \frac{\rho_p}{\rho_f} R_e \frac{d\mathbf{U}_p}{dt} &= G \mathbf{e}_g + \frac{6}{\pi} \int [-p\mathbf{1} + \boldsymbol{\tau}] \cdot \mathbf{n} d\Gamma, \\ \frac{\rho_p}{\rho_f} R_e \frac{d\boldsymbol{\Omega}_p}{dt} &= \frac{60}{\pi} \int (\mathbf{x} - \mathbf{X}_p) \times ([-p\mathbf{1} + \boldsymbol{\tau}] \cdot \mathbf{n}) d\Gamma, \end{aligned} \quad (2.9)$$

where \mathbf{e}_g is the unit vector in the direction of the gravity. The dimensionless parameters are

$$R_e = \frac{\rho_f V(2a)}{\mu} = \frac{\rho_f \dot{\gamma}_w(2a)^2}{\mu} = \frac{8a^2 \rho_f U_m}{\mu R}, \text{ the Reynolds number;} \quad (2.10)$$

$$G = \frac{(\rho_p - \rho_f)g(2a)^2}{\mu V}, \text{ the gravity number;} \quad (2.11)$$

$$\rho_p / \rho_f, \text{ the density ratio.} \quad (2.12)$$

It is convenient to carry out the analysis of correlations in terms of dimensionless forms of correlating parameters. The ratio of the sphere radius a to pipe radius R and the dimensionless radial position \bar{r} are defined by

$$\bar{a} = a/R, \bar{r} = r/R. \quad (2.13)$$

The dimensionless lift is given by

$$\bar{L} = \frac{6\rho_f L}{\pi\mu^2}. \quad (2.14)$$

The flow quantities U_m , U_s , Ω_s , Ω_{se} are expressed in the form of dimensionless Reynolds numbers. A flow Reynolds number is given by

$$\bar{U}_m = \frac{\rho_f U_m R}{\mu} = \frac{R_e}{8\bar{a}^2} \quad (2.15)$$

Slip velocity Reynolds numbers are defined as

$$\begin{aligned} \bar{U}_s &= \rho_f U_s(2a) / \mu, \\ \bar{\Omega}_s &= \rho_f \Omega_s(2a)^2 / \mu, \\ \bar{\Omega}_{se} &= \rho_f \Omega_{se}(2a)^2 / \mu. \end{aligned} \quad (2.16)$$

A dimensionless form of the product $U_s(\Omega_s - \Omega_{se})$ which enters into our lift law is given as the product

$$\bar{U}_s(\bar{\Omega}_s - \bar{\Omega}_{se}). \quad (2.17)$$

We call the reader's attention to the fact that the flow is in the negative x direction in our simulation (see figure E-1). The symbol U_m in (2.10) and (2.15) should be understood as the magnitude of the fluid velocity at the tube centerline. Similarly, we use the magnitude of U_f and U_p to calculate the slip velocity U_s defined in (1.1).

We shall focus on the steady state flow of a neutrally buoyant sphere, in which the left side of (2.9) and the term $G\mathbf{e}_g$ in (2.9) vanish. Thus, R_e and \bar{a} are the two parameters at play.

3. Comparison of results

We study the behavior of a neutrally buoyant sphere suspended in tube Poiseuille flows. A comparison of the numerical results using the ALE code with the experiments by Karnis, Goldsmith and Mason (1966) was presented by Zhu (2000). Karnis *et al.* performed a large number of experiments on the migration of spheres, rods and disks in a Poiseuille flow in a capillary tube. Zhu (2000) compared the trajectories of spheres released at two radial positions $\bar{r} = 0.21$ and 0.68 to the trajectories measured by Karnis *et al.* Figure E-2 shows that the numerical results are in excellent agreement with the experimental ones.

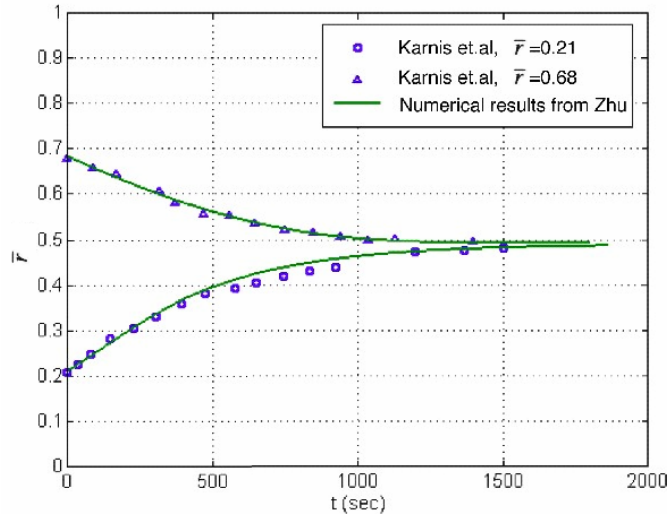


Figure E-2. Comparison of migration trajectories of a neutrally buoyant sphere calculated numerically with the ones measured in the experiments of Karnis, Goldsmith and Mason (1966). The fluid properties are $\rho_f = 1.05 \text{ g}\cdot\text{cm}^{-3}$ and $\mu = 1.2 \text{ poises}$, the flow rate is $Q = 7.11 \times 10^{-2} \text{ cm}^3/\text{sec}$, the tube diameter is $D = 0.4 \text{ cm}$, and the sphere diameter is $d = 0.122 \text{ cm}$.

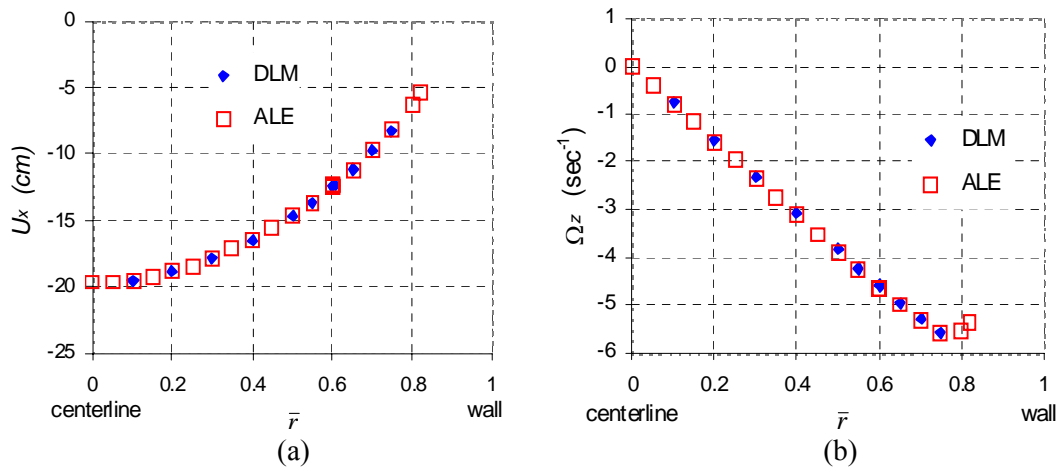
An equilibrium for a free neutrally buoyant particle is achieved when the particle migrates to a radial position \bar{r}_e of steady rectilinear motion in which the acceleration and angular acceleration vanish and the hydrodynamic lift force is zero. We perform two types of simulations, unconstrained and constrained simulations, to find the equilibrium position. In unconstrained simulation, the particle moves freely until it reaches its equilibrium position, just as it would do in experiments. In constrained simulation, the particle is only allowed to move along a line parallel to the axis of the tube and rotate freely; its lateral migration is suppressed and radial position is fixed. When such a constrained motion reaches steady state in which the particle accelerations vanish, a hydrodynamic lift force L in the radial direction can be calculated. This lift force L is a function of the radial position; the position where $L = 0$ is the equilibrium position \bar{r}_e . In our constrained simulation, we place the sphere center at $(y = r, z = 0)$ (see figure E-1), so that the lift

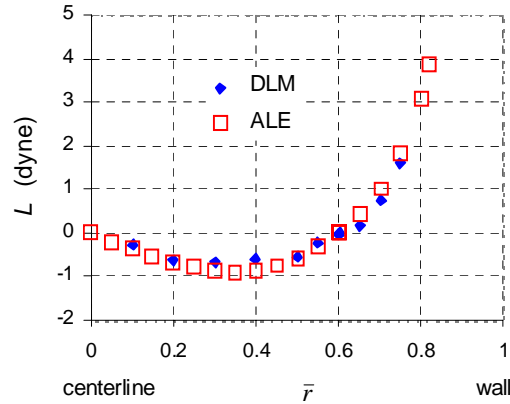
force at steady state is in y direction and z direction is the neutral direction. The only component of the particle translational velocity at steady state is U_x and Ω_z is the only component of the angular velocity.

We compare the results of the unconstrained and constrained simulations obtained using the ALE code and the DLM code. In the ALE code, the typical mesh used in most of our simulations consists of 1.05×10^5 elements, 1.46×10^5 nodes and 1.9×10^4 vertices. The number of nodes for velocity is about 2.22×10^6 in the DLM code. We consider a case in which the radii of the particle and the tube are 0.375 cm and 2.5 cm respectively (the radius ratio $\bar{a} = 0.15$), the density of the particle and the fluid is 1 g/cm^3 , the viscosity of the fluid is 1 poise, and $U_m = 20 \text{ cm/sec}$ ($Re = 9$). We compare the equilibrium position \bar{r}_e and velocities U_x and Ω_z at equilibrium calculated from the unconstrained simulation in table E-1. We compare the lift force $L(\bar{r})$, velocities $U_x(\bar{r})$ and $\Omega_z(\bar{r})$, calculated from the constrained simulation in figure E-3.

	\bar{r}_e	U_x (cm/sec)	Ω_z (sec $^{-1}$)
ALE	0.601	12.4	4.65
DLM	0.606	12.2	4.63

Table E-1. The equilibrium position \bar{r}_e and particle velocities U_x and Ω_z at equilibrium calculated from the unconstrained simulation. The results of the ALE and DLM codes are almost the same.





(c)

Figure E-3. The steady state values of the particle velocities U_x (a) and Ω_z (b) and the lift force L (c), from the constrained simulation at different radial positions. The ALE and DLM results are in good agreement.

Figures E-3.a and E-3.b show that the particle translational and angular velocities obtained from the DLM and ALE codes are almost the same. The agreement of the lift forces from the two codes in figure E-3.c is not as good as the velocities. The lift force curve from the DLM code is not quite smooth since this method was intended to simulate the dynamics of the interaction of fluid and many particles and not to compute the hydrodynamic forces explicitly. Nevertheless, we regard the agreement in figure E-3.c acceptable, considering the challenging nature of the three-dimensional simulation. Due to mesh adaptivity, the ALE code is more suited to accurate computation of lift. We will use the data from the ALE code to construct the lift correlations in the following section.

Our two different codes give results in good agreement with each other and with experiments, which demonstrates that our numerical simulation is credible.

4. Correlations from the numerical simulation

Numerical experiments using constrained simulation provide us with the distribution of the lift force and particle velocity in the tube and the position and velocity of the particle at equilibrium. We develop correlations for these quantities in this section. The key correlation is for the lift force, which shows the dependence of the lift force on the slip angular velocity discrepancy $\Omega_s - \Omega_{se}$. The lift force correlation predicts the change of sign of the lift force, which is necessary to explain the two-way migration in the Segrè-Silberberg effect. The correlations for the equilibrium state of the particle are also of interest, because they may be used to predict the position and the velocities of the particle at equilibrium.

4.1 Correlation for the lift force

The steady state values of the lift forces on a sphere at different radial positions computed in constrained simulation are plotted in figure 4 for a sphere with the radius ratio $\bar{a} = 0.15$. The positive direction of the lift force is in the negative \mathbf{e}_r direction. In other words, \bar{L} is positive when pointing to the centerline and negative when pointing away from the centerline.

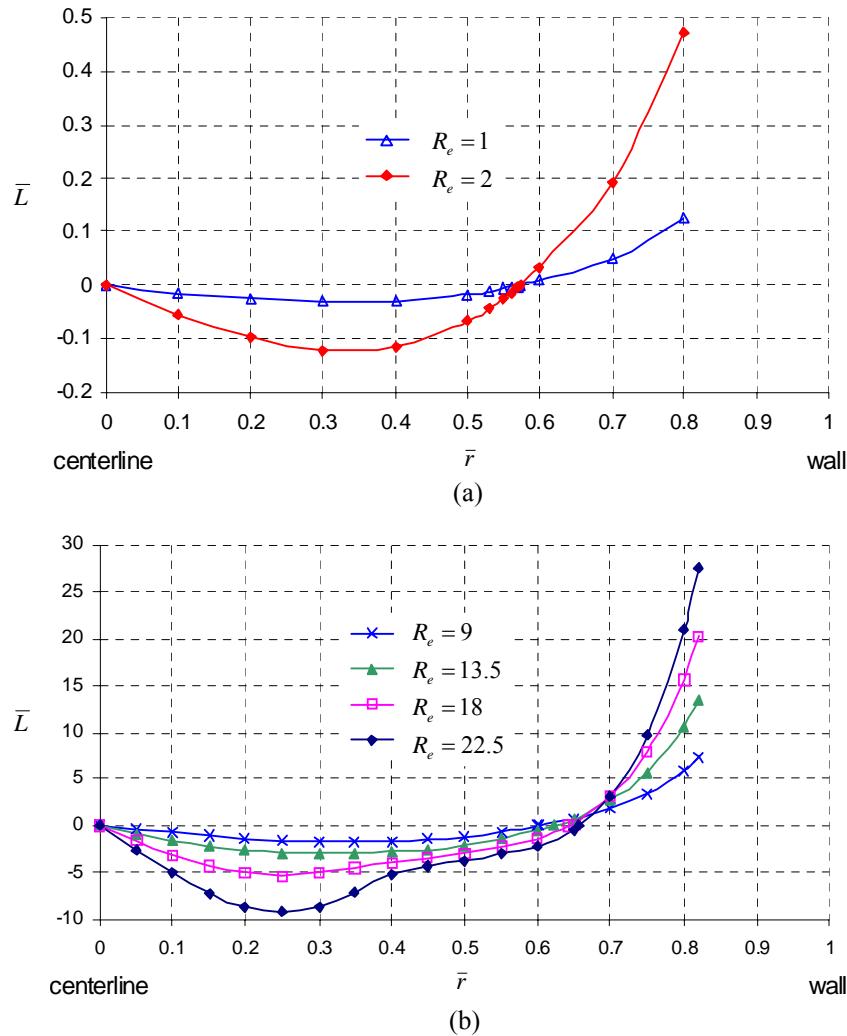


Figure E-4. The dimensionless lift force \bar{L} at different radial positions for a sphere with the radius ratio $\bar{a} = 0.15$. The two curves in (a) correspond to $R_e = 1$ and 2, and the four curves in (b) correspond to $R_e = 9, 13.5, 18$ and 22.5, respectively. The magnitude of the lift force increases with the Reynolds number.

The equilibrium positions of a neutrally buoyant sphere are the points where $\bar{L} = 0$. The stability of the equilibrium at a zero-lift point can be determined from the slope of the \bar{L} vs. \bar{r} curve. The centerline is on a negative-slope branch of the \bar{L} vs. \bar{r} curve. When a particle is disturbed away from the centerline, the lift force is negative and drives the particle further away

from the centerline. Therefore the centerline is an unstable equilibrium position. The other zero-lift point is between the centerline and the wall and it is on a positive-slope branch of the curve. When the particle is disturbed away from this point, the lift force tends to push the particle back. Thus the zero-lift point between the centerline and the wall is a stable equilibrium position. Figure E-4 shows that this stable equilibrium position \bar{r}_e moves towards the wall as the Reynolds number increases.

We seek expressions for the lift force in terms of the slip velocities. The slip velocity Reynolds numbers have been defined in (2.16). We plot $\bar{\Omega}_s - \bar{\Omega}_{se}$ at different radial positions in figure E-5 for a sphere with $\bar{a} = 0.15$. Comparison of figure E-4 and figure E-5 shows that the discrepancy $\bar{\Omega}_s - \bar{\Omega}_{se}$ changes sign across the equilibrium position, just like the lift force \bar{L} does.

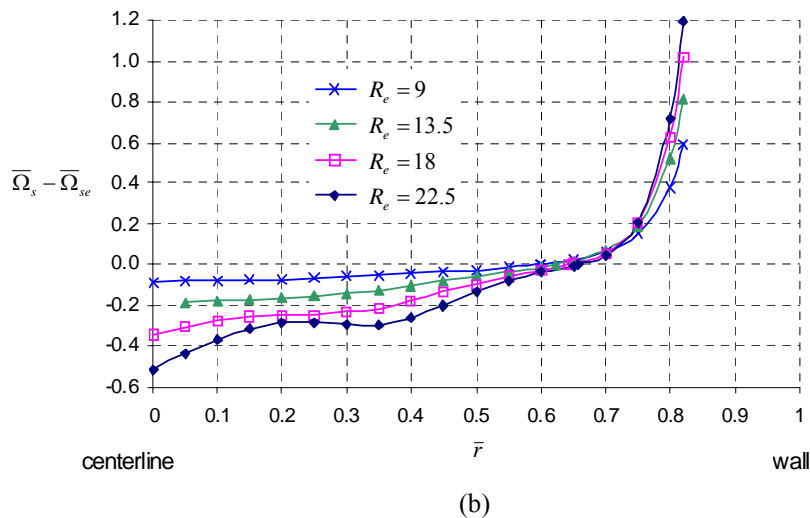
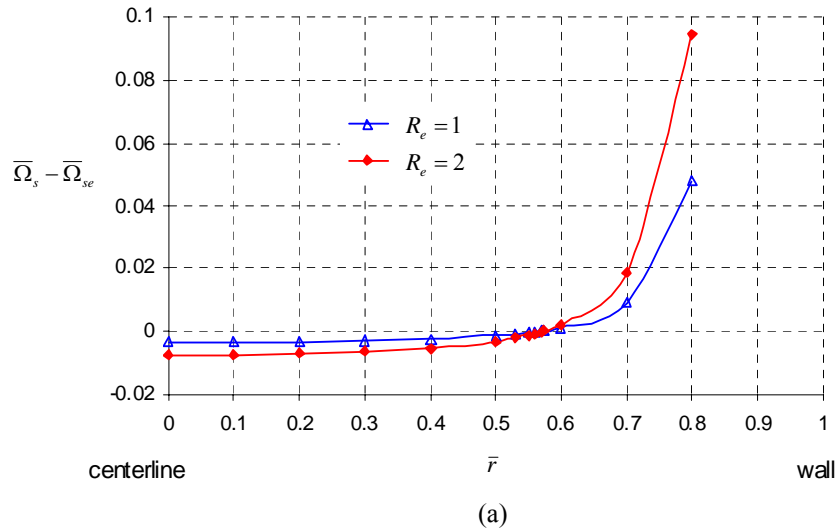


Figure E-5. The dimensionless slip angular velocity discrepancy at different radial positions for a sphere with $\bar{a} = 0.15$. The two curves in (a) correspond to $R_e = 1$ and 2, and the four curves in (b) correspond to $R_e = 9, 13.5, 18$ and 22.5, respectively.

If we fix the radius ratio $\bar{a} = 0.15$ and continue to increase the Reynolds number, the distribution of the lift force as a function of the radial position becomes more complicated. We plot the \bar{L} vs. \bar{r} curves for $R_e = 27, 36$ and 45 in figure E-6. There is a change of convexity in the curves and a local minimum of the lift force exists at approximately $\bar{r} = 0.55$. On each of the curves, there exist two branches on which the slope of the curve is negative. The first negative-slope branch is at the centerline; the second negative-slope branch is in the middle between the centerline and the wall. The second negative-slope branch does not exist when the Reynolds number is small ($R_e = 1, 2, 9, 13.5, 18$ or 22.5). The exact range of the second negative-slope branch varies with the Reynolds number; we may say that the range $0.5 \leq \bar{r} \leq 0.65$ covers the second negative-slope branches of the curves for $R_e = 27, 36$ and 45. We found that it was difficult for the constrained simulations in this range at high Reynolds numbers to converge to a steady state; a refined mesh was necessary to obtain converged results in these simulations. For example, when $R_e = 1$, the typical mesh used in our simulations consists of 9.09×10^4 elements, 1.28×10^5 nodes and 1.68×10^4 vertices; when $R_e = 45$, the typical mesh consists of 9.86×10^4 elements, 1.39×10^5 nodes and 1.82×10^4 vertices.

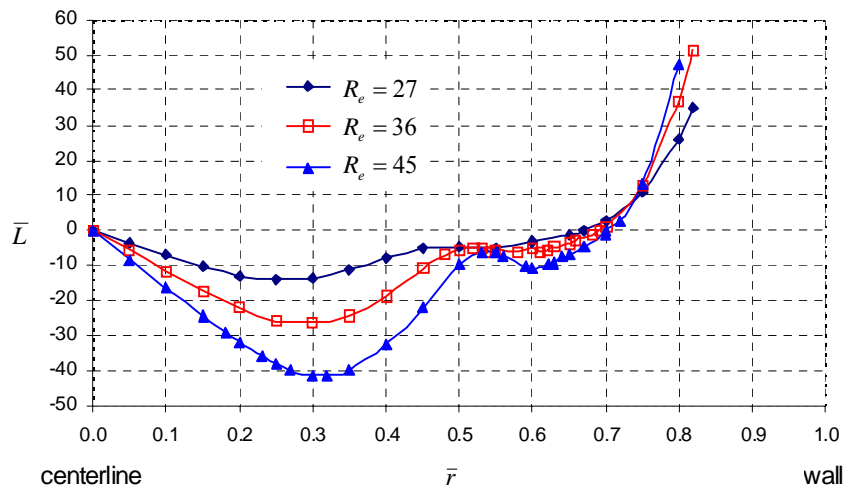


Figure E-6. The dimensionless lift force \bar{L} at different radial positions for a sphere with $\bar{a} = 0.15$. The three curves corresponds to $R_e = 27, 36$ and 45, respectively. On each of the curve, there exist two branches on which the slope of the curve is negative.

Similar complicated distributions of the lift force can be observed in Asmolov's (1999) calculation of the lift force on a small neutrally buoyant sphere in a plane Poiseuille flow. In his figure E-8, the lift is plotted as a function of d/l , where d is the distance from the wall to the particle center and l is the channel width. Five curves for five channel Reynolds numbers $R_c = 15, 100, 300, 1000$ and 3000 are plotted. There is only one negative-slope branch on the curves for $R_c = 15$ and 100 , which is at the centerline. There are two negative-slope branches on the curves for $R_c = 300, 1000$ and 3000 . One of the branches is at the centerline and the other is between the centerline and the wall. Both our numerical simulation and Asmolov's (1999) calculation using matched asymptotic methods show that at high R_e , there exists a local minimum of the lift force between the centerline and the stable equilibrium position. This observation prompts us to consider the possibility of multiple equilibrium positions for neutrally buoyant particles in Poiseuille flows.

Matas, Morris and Guazzelli (2004) measured lateral migration of dilute suspensions of neutrally buoyant spheres in pipe flows; they observed single equilibrium positions when \bar{U}_m is low (60, 350) and multiple equilibrium positions when \bar{U}_m is high (760). In their experiments using spheres with $\bar{a} = 0.06875$ in flows with $\bar{U}_m = 760$, they observed a first equilibrium position close to the wall and a second equilibrium position at $\bar{r} = 0.5 \pm 0.2$. They also reported that when \bar{U}_m is increased to 1500, the first equilibrium position close to the wall disappeared and the second equilibrium position became the only equilibrium position. Matas, Morris and Guazzelli proposed to explain the second equilibrium position using the change of convexity in the lift force profiles obtained from the matched asymptotic methods. They argued that the particles could accumulate in the region near the local minimum of the lift force.

In numerical simulations, Patankar, Huang, Ko and Joseph (2001) reported multiple equilibrium positions for particles heavier than the fluid in plane Poiseuille flows perpendicular to the gravity. We have not obtained multiple equilibrium positions in simulations for a neutrally buoyant sphere in pipe flows. We are not able to run simulations matching the experimental conditions under which multiple equilibrium positions were observed. From figure E-6, it seems possible that a second stable equilibrium position appears near $\bar{r} = 0.55$ at higher R_e . It is also possible that the second equilibrium position arises from particle interaction in the experiments. The existence of multiple equilibrium positions for a single neutrally buoyant particle in a pipe flow is still an open question.

The $\overline{\Omega}_s - \overline{\Omega}_{se}$ vs. \bar{r} curves for the cases with $\bar{a} = 0.15$ and $R_e = 27, 36$ or 45 are plotted in figure E-7. Our assertion that the lift force changes sign with the discrepancy $\overline{\Omega}_s - \overline{\Omega}_{se}$ remains true for $R_e = 27$ and 36 but not for $R_e = 45$. When $R_e = 45$, $\overline{\Omega}_s - \overline{\Omega}_{se}$ changes sign twice in the range $0 < \bar{r} < 0.5$ (figure E-7); however, the lift force remains negative in the same range (figure E-6). Our assertion is true in the vicinity of the stable equilibrium position at all the Reynolds numbers, which will be the region in which the lift correlation is developed.

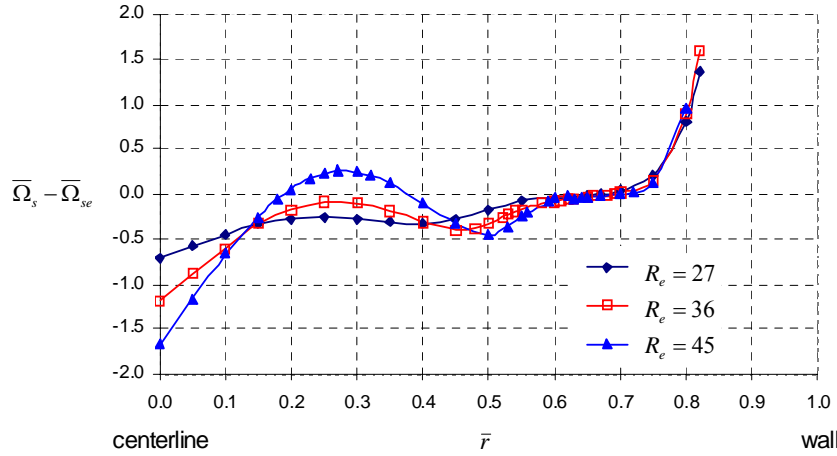


Figure E-7. The dimensionless slip angular velocity discrepancy at different radial positions for a sphere with $\bar{a} = 0.15$. The three curves correspond to $R_e = 27, 36$, and 45 , respectively.

We seek correlations between the lift force \bar{L} and the product

$$F = \bar{U}_s (\overline{\Omega}_s - \overline{\Omega}_{se}). \quad (4.1)$$

From our data, we noted that in the vicinity of the stable equilibrium position, the relation between \bar{L} and F may be represented by a linear correlation:

$$\bar{L}(\bar{r}, R_e, \bar{a}) = k(R_e, \bar{a})F(\bar{r}, R_e, \bar{a}), \quad (4.2)$$

where k is the proportionality coefficient which depends on the Reynolds number and the radius ratio \bar{a} . Some examples of the linear correlation between \bar{L} and F are plotted in figure E-8 and the values of k are listed in table E-2. The linear correlation (4.2) is not valid far away from the equilibrium position; we also list the range of the radial position in which the linear correlation is valid in table E-2.

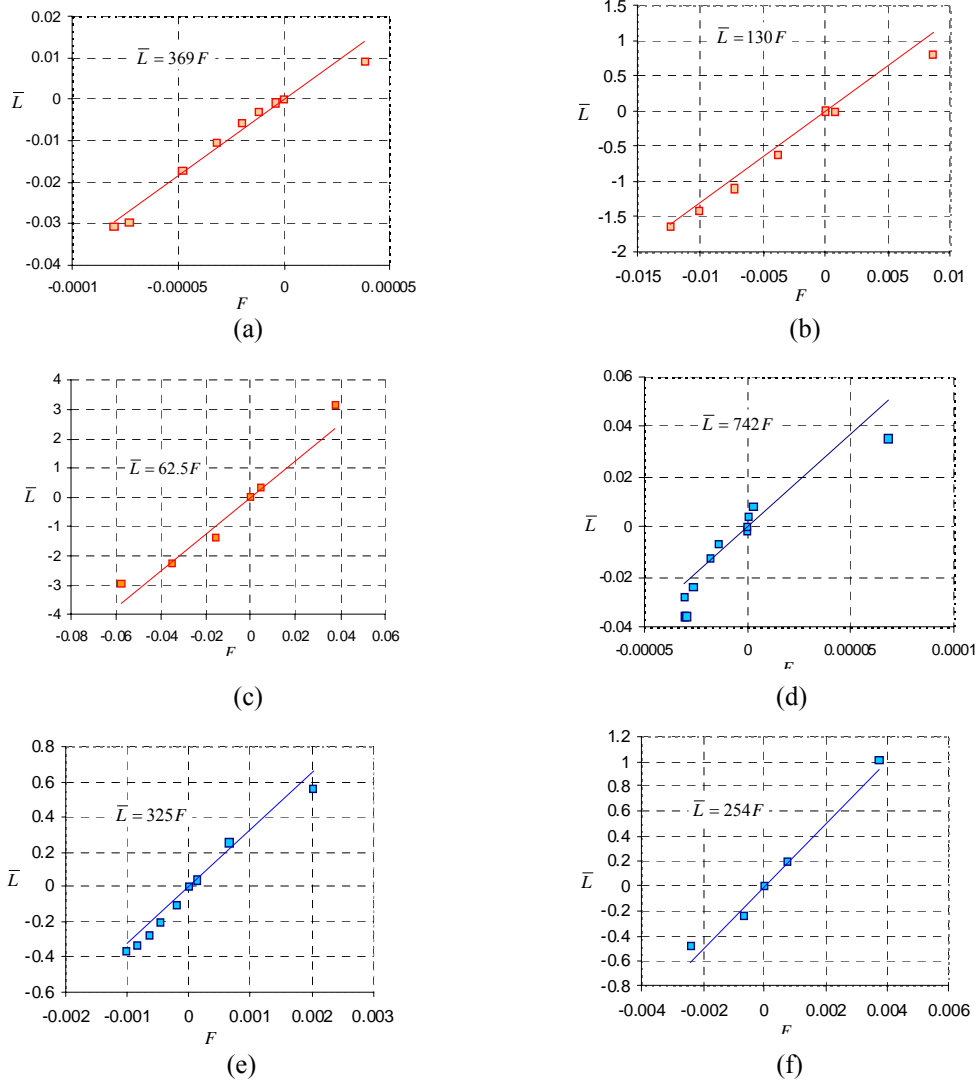


Figure E-8. The linear correlation between \bar{L} and F in the vicinity of the stable equilibrium position of a neutrally buoyant particle. (a) $R_e = 1$, $\bar{a} = 0.15$; (b) $R_e = 9$, $\bar{a} = 0.15$; (c) $R_e = 18$, $\bar{a} = 0.15$; (d) $R_e = 1$, $\bar{a} = 0.1$; (e) $R_e = 4$, $\bar{a} = 0.1$; (f) $R_e = 8$, $\bar{a} = 0.1$.

\bar{a}	R_e	k	equilibrium position \bar{r}_e	range of the linear correlation
0.1	1	742	0.603	$0.2 \leq \bar{r} \leq 0.7$
	2	620	0.608	$0.3 \leq \bar{r} \leq 0.7$
	4	325	0.638	$0.4 \leq \bar{r} \leq 0.75$
	6	268	0.661	$0.55 \leq \bar{r} \leq 0.75$
	8	254	0.674	$0.6 \leq \bar{r} \leq 0.75$
	10	201	0.684	$0.6 \leq \bar{r} \leq 0.75$
	12	169	0.708	$0.65 \leq \bar{r} \leq 0.8$
0.15	1	369	0.573	$0.3 \leq \bar{r} \leq 0.6$
	2	346	0.573	$0.3 \leq \bar{r} \leq 0.6$
	9	130	0.601	$0.4 \leq \bar{r} \leq 0.65$
	13.5	77.2	0.623	$0.45 \leq \bar{r} \leq 0.7$
	18	62.5	0.642	$0.5 \leq \bar{r} \leq 0.7$

	22.5	53.5	0.657	$0.55 \leq \bar{r} \leq 0.7$
	27	56.5	0.670	$0.6 \leq \bar{r} \leq 0.75$
	36	69.8	0.691	$0.65 \leq \bar{r} \leq 0.75$
	45	85.2	0.700	$0.67 \leq \bar{r} \leq 0.75$

Table E-2. The values of the proportionality coefficient k and the equilibrium position \bar{r}_e as functions of the radius ratio \bar{a} and R_e . The range of the radial position in which the linear correlation (4.2) is valid is also listed.

The value of k decreases as R_e increases when the Reynolds number is low. However, k increases as R_e increases when $R_e \geq 27$. This change is possibly related to the emergence of the second negative-slope branch on the \bar{L} vs. \bar{r} plot at high Reynolds numbers. We shall focus on the low Reynolds number cases and data fitting analyses lead to expressions for k in terms of the Reynolds number:

$$k = 809R_e^{-0.604}, \quad \text{for } \bar{a} = 0.1 \quad \text{and } 1 \leq R_e \leq 12; \quad (4.3)$$

$$k = 450R_e^{-0.658}, \quad \text{for } \bar{a} = 0.15 \quad \text{and } 1 \leq R_e \leq 22.5. \quad (4.4)$$

Inserting the expression of k into the linear correlation (4.2), we can obtain the correlations between \bar{L} and F . To reveal the dependence of the lift force on the slip velocities explicitly, we substitute the definitions of \bar{L} and F into the linear correlation and it follows that

$$L = 424R_e^{-0.604} \rho_f U_s (\Omega_s - \Omega_{se}) (2a)^3, \quad \text{for } \bar{a} = 0.1; \quad (4.5)$$

$$L = 236R_e^{-0.658} \rho_f U_s (\Omega_s - \Omega_{se}) (2a)^3, \quad \text{for } \bar{a} = 0.15. \quad (4.6)$$

Both of these two correlations are analogous to the lift correlation we obtained in the two-dimensional cases (Wang and Joseph 2003):

$$L = 182.6R_e^{-0.515} \rho_f U_s (\Omega_s - \Omega_{se}) (2a)^2, \quad (4.7)$$

which is for the lift force per unit length on a cylindrical particle whose diameter is 1/12 of the channel width. It is noted that the exponent of the Reynolds number is -0.604 in (4.5) and it is closer to the value -0.515 in (4.7).

The lift force in our correlation is on a freely rotating particle translating at steady velocity. Thus correlations (4.5) and (4.6) apply to particles with zero acceleration. For a migrating particle with substantial acceleration, correlations (4.5) and (4.6) may not be valid.

4.2 Correlations for the slip velocity U_s and slip angular velocity Ω_s

Besides the lift force on the particle, the translational and angular velocities of the particle at steady state are also of interest. We shall construct correlations for the slip velocity U_s and slip

angular velocity Ω_s from constrained simulations; the particle velocities can then be easily computed using (1.1) and (1.2). The correlations for U_s and Ω_s are necessary to compute the lift force, because they appear in the lift correlations (4.5) and (4.6).

We illustrate the correlation construction for a particle with the radius ratio $\bar{a} = 0.15$. We plot the Reynolds number $\bar{\Omega}_s$ on log-log plots versus R_e ; straight lines one for each value of \bar{r} are obtained. Similar straight lines on log-log plots are obtained when we plot \bar{U}_s versus R_e . Examples of such plots are shown in figure E-9.a and 9.b for $\bar{\Omega}_s$ vs. R_e and \bar{U}_s vs. R_e , respectively.

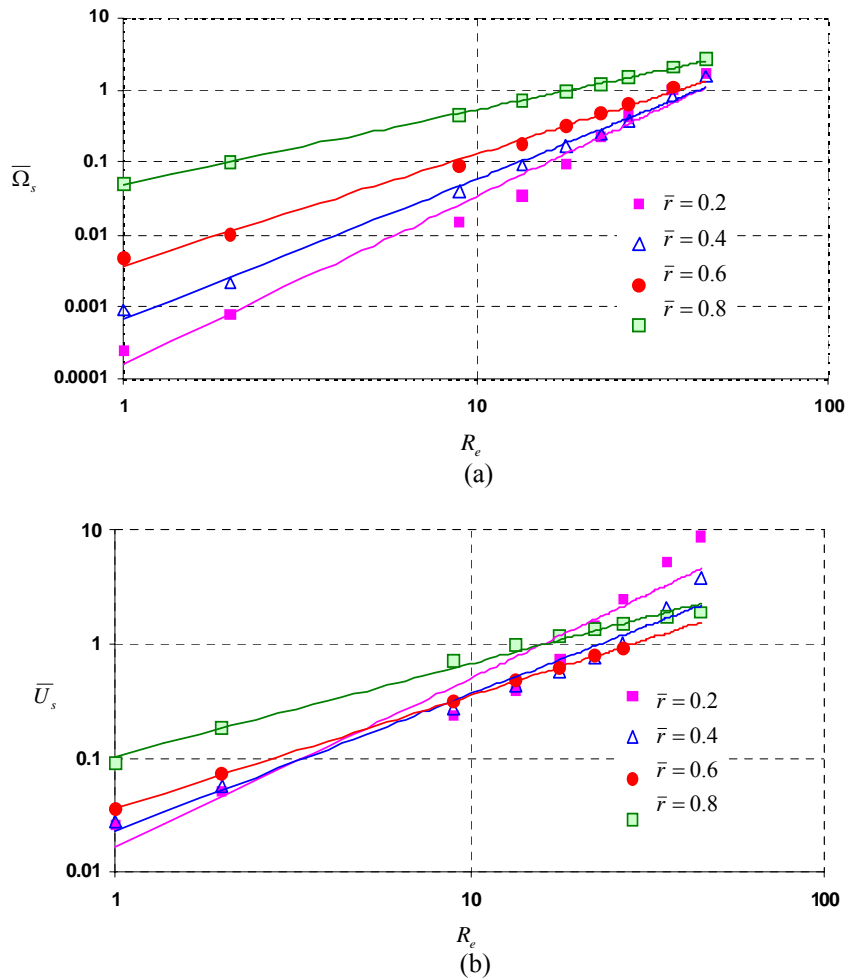


Figure E-9. Power law correlations of (a) $\bar{\Omega}_s$ vs. R_e and (b) \bar{U}_s vs. R_e at different values of \bar{r} for a sphere with $\bar{a} = 0.15$.

Power law correlations arise from the straight lines in log-log plots for $\bar{\Omega}_s$ and \bar{U}_s

$$\bar{U}_s(\bar{r}, R_e, \bar{a}) = b(\bar{r}, \bar{a}) R_e^{m(\bar{r}, \bar{a})}, \quad (4.8)$$

$$\overline{\Omega}_s(\bar{r}, R_e, \bar{a}) = c(\bar{r}, \bar{a}) R_e^{n(\bar{r}, \bar{a})}. \quad (4.9)$$

The coefficients b , m , c , and n are obtained for a particle with $\bar{a} = 0.15$ in the range $0.1 \leq \bar{r} \leq 0.8$ and plotted in figure E-10. Exponential fitting and linear fitting may give reasonable approximations to the prefactors b and c and exponents m and n , respectively:

$$b = 1.1 \times 10^{-2} \exp(2.2\bar{r}), \quad c = 2.3 \times 10^{-5} \exp(8.8\bar{r}); \quad (4.10)$$

$$m = -1.1\bar{r} + 1.6, \quad n = -2.1\bar{r} + 2.7. \quad (4.11)$$

Substitution of (4.10) and (4.11) into (4.8) and (4.9) leads to explicit expressions for \overline{U}_s and $\overline{\Omega}_s$

$$\overline{U}_s = 1.1 \times 10^{-2} \exp(2.2\bar{r}) R_e^{-1.1\bar{r}+1.6}, \quad (4.12)$$

$$\overline{\Omega}_s = 2.3 \times 10^{-5} \exp(8.8\bar{r}) R_e^{-2.1\bar{r}+2.7}, \quad (4.13)$$

which apply to a particle with $\bar{a} = 0.15$ in the range $0.1 \leq \bar{r} \leq 0.8$. Correlation (4.12) and (4.13) are generally valid in the range of $1 \leq R_e \leq 45$. However, correlation (4.12) is not in good agreement with the data for \overline{U}_s on the second negative-slope branch on the \overline{L} vs. \bar{r} curve ($0.5 \leq \bar{r} \leq 0.65$) at high Reynolds numbers ($R_e = 27, 36$ and 45). Thus correlation (4.12) in the range $0.5 \leq \bar{r} \leq 0.65$ is valid only for $1 \leq R_e \leq 22.5$.

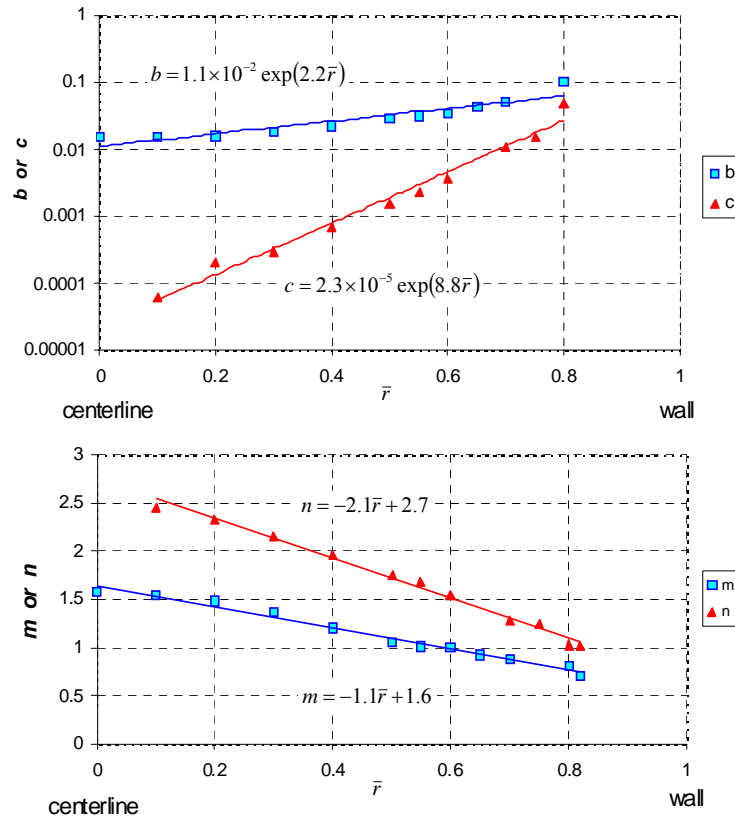


Figure E-10. The prefactors b and c and exponents m and n in correlations (4.8) and (4.9) for a particle with $\bar{a} = 0.15$ in the range $0.1 \leq \bar{r} \leq 0.8$.

Correlations for \bar{U}_s and $\bar{\Omega}_s$ for $\bar{a} = 0.1$ are developed using the same procedure as for $\bar{a} = 0.15$. We omit the details of derivation and only give the final formulas for \bar{U}_s and $\bar{\Omega}_s$

$$\bar{U}_s = 8.3 \times 10^{-3} \exp(1.8\bar{r}) R_e^{-1.4\bar{r}+1.9}, \quad (4.14)$$

$$\bar{\Omega}_s = 7.7 \times 10^{-6} \exp(9.0\bar{r}) R_e^{-3.3\bar{r}+3.8}, \quad (4.15)$$

which apply to a particle with $\bar{a} = 0.1$ in the range $0.05 \leq \bar{r} \leq 0.85$. The range of the Reynolds number in which (4.14) and (4.15) is valid is $1 \leq R_e \leq 12$.

4.3. Correlations for the particle parameters at equilibrium

The equilibrium state of a particle is always the focus of the study of particle migration. We obtain the particle parameters at stable equilibrium, such as the equilibrium position \bar{r}_e , the slip velocity U_{se} and the slip angular velocity Ω_{se} by unconstrained simulation and find that they may be correlated to the Reynolds number. We summarize the particle parameters at stable equilibrium in table E-3.

\bar{a}	R_e	\bar{U}_m	\bar{r}_e	$\bar{\Omega}_{se}$	\bar{U}_{se}
0.05	2	100	0.731	0.00710	0.0247
0.1	1	12.5	0.603	0.00188	0.0219
	2	25	0.608	0.00509	0.0444
	4	50	0.638	0.0209	0.0901
	6	75	0.661	0.0498	0.152
	8	100	0.674	0.0901	0.470
	10	125	0.684	0.139	0.712
	12	150	0.708	0.202	0.296
0.15	1	5.56	0.573	0.00354	0.0338
	2	11.1	0.573	0.00765	0.0675
	9	50	0.601	0.0861	0.306
	13.5	75	0.623	0.197	0.482
	18	100	0.642	0.342	0.730
	22.5	125	0.657	0.513	0.785
	27	150	0.670	0.705	1.07
	36	200	0.691	1.16	1.18
	45	250	0.700	1.67	1.74
0.2	32	100	0.598	0.793	1.74
0.25	50	100	0.567	1.49	2.84

Table E-3. Particle parameters at stable equilibrium: the equilibrium position \bar{r}_e , the dimensionless slip angular velocity $\bar{\Omega}_{se} = \rho_f \Omega_{se} (2a)^2 / \mu$ and the dimensionless slip velocity $\bar{U}_{se} = \rho_f U_{se} (2a) / \mu$.

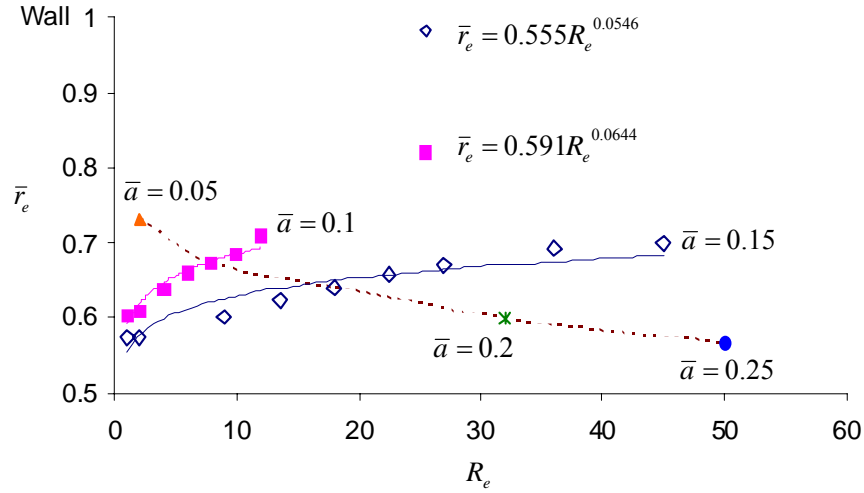


Figure E-11. The stable equilibrium position \bar{r}_e of a neutrally buoyant sphere as a function of the Reynolds number. The two power law curves are for spheres with $\bar{a} = 0.10$ and $\bar{a} = 0.15$ respectively. All the points on the dotted line are for the same flow Reynolds number $\bar{U}_m = 100$; the dotted line shows that when \bar{U}_m is fixed, the equilibrium position becomes closer to the centerline as \bar{a} increases.

We can correlate the stable equilibrium position of a neutrally buoyant sphere with the Reynolds number (see figure E-11):

$$\bar{r}_e = 0.591R_e^{0.0644} \quad \text{for } \bar{a} = 0.1; \quad (4.16)$$

$$\bar{r}_e = 0.555R_e^{0.0546} \quad \text{for } \bar{a} = 0.15. \quad (4.17)$$

The equilibrium position \bar{r}_e moves closer to the wall as the Reynolds number increases. We also observe that when the flow Reynolds number \bar{U}_m is fixed, the larger particle finds its equilibrium position closer to the centerline than the smaller particle. The above observations are in agreement with the experiments by Karnis, Goldsmith and Mason (1966), who reported that neutrally buoyant particles stabilized closer to the wall for larger flow rates and closer to the center for larger particles.

Matas, Morris and Guazzelli (2004) reported that for neutrally buoyant spheres with a diameter $d = 900 \mu\text{m}$ in the pipe of diameter $D = 8 \text{ mm}$, the equilibrium position is $\bar{r}_e = 0.64 \pm 0.04$ for $\bar{U}_m = 60$ and $\bar{r}_e = 0.78 \pm 0.04$ for $\bar{U}_m = 350$. The value of \bar{a} is close to 0.1 in these experiments, thus we can compare correlation (4.16) to the experimental results. Equations (4.16) and (2.15) predict $\bar{r}_e = 0.654, 0.732$ for $\bar{U}_m = 60, 350$ respectively, in good agreement

with the experimental results. Matas, Morris and Guazzeli (2004) stated that the matched asymptotic calculation (Schonberg & Hinch 1989, Asmolov 1999) predicts that $\bar{r}_e = 0.71, 0.85$ for $\bar{U}_m = 60, 350$ respectively, in both cases larger than the experimental value. They attributed this difference to the relatively large size of the particles. They reported that when smaller particles (200 μm) were used in the experiments, equilibrium positions were closer to the theoretical predictions. The actual values of \bar{r}_e for 200 μm particles are not reported in their paper, but we can infer that \bar{r}_e for 200 μm particles is larger than \bar{r}_e for 900 μm particles at the same \bar{U}_m . This agrees with our conclusion that the larger particle finds its equilibrium position closer to the centerline than the smaller particle at a fixed \bar{U}_m .

If we correlate the dimensionless slip angular velocity at equilibrium $\bar{\Omega}_{se}$ with the Reynolds number R_e , we obtain (see figure E-12)

$$\bar{\Omega}_{se} = 0.0023R_e^{1.72} \quad \text{i.e.} \quad \Omega_{se} = 0.0023R_e^{1.72} \mu / (\rho_f 4a^2). \quad (4.18)$$

This correlation appears to be applicable to a wide range of the radius ratio: $0.05 \leq \bar{a} \leq 0.25$. Correlation (4.18) is important because it gives explicitly the slip angular velocity when the particle is at stable equilibrium.

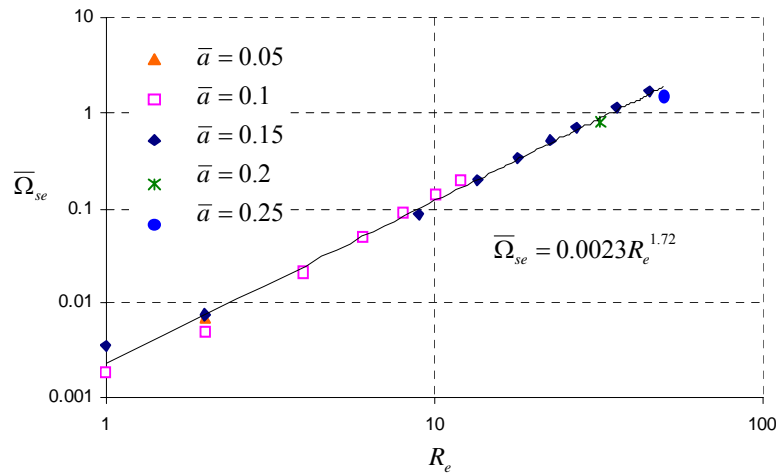


Figure E-12. The correlation between $\bar{\Omega}_{se}$ and the Reynolds number R_e .

Now with all the correlations for k , \bar{U}_s , $\bar{\Omega}_s$, and $\bar{\Omega}_{se}$ available, we are at a position to make the lift correlation (4.2) completely explicit. Take a particle with $\bar{a} = 0.15$ for example,

$$\bar{L} = k\bar{U}_s(\bar{\Omega}_s - \bar{\Omega}_{se}), \quad (4.19)$$

where k , \bar{U}_s , $\bar{\Omega}_s$, and $\bar{\Omega}_{se}$ are given in (4.4), (4.12), (4.13) and (4.18) respectively. Therefore, we are able to compute the lift force on a particle at different radial positions from the Reynolds number and radius ratio. It should be noted that the lift force applies to a freely rotating particle translating at a steady speed.

If we set \bar{L} in (4.19) to zero, we can solve for the equilibrium position \bar{r}_e . The value $\bar{L} = 0$ is given by $\bar{\Omega}_s = \bar{\Omega}_{se}$; this leads to a formula for the equilibrium position

$$\bar{r}_e = \frac{4.6 - 0.98 \ln R_e}{8.8 - 2.1 \ln R_e}, \tag{4.20}$$

for a particle with $\bar{a} = 0.15$ which can be compared to correlation (4.17). Formula (4.17) and (4.20) give rise to similar values for \bar{r}_e in the range $1 \leq R_e \leq 22.5$ (see figure E-13); (4.17) gives a better approximation to the simulation results because it is directly developed for \bar{r}_e . When $R_e > 22.5$, the agreement is not good between (4.17) and (4.20).

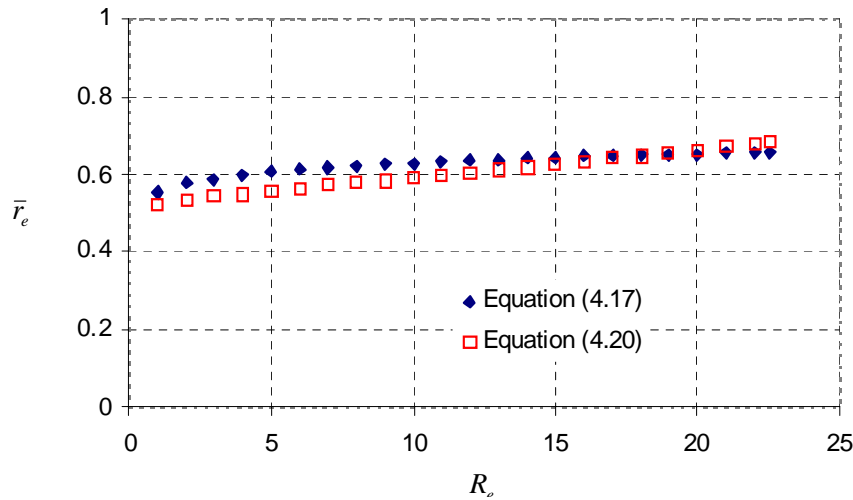


Figure E-13. The values of \bar{r}_e computed by equations (4.17) and (4.20) in the range $1 \leq R_e \leq 22.5$ for $\bar{a} = 0.15$.

A summary of our correlations is presented in Table E-4 below. Correlation formula exhibiting the dependence of prefactors and exponents on \bar{a} requires more computation.

$\bar{L}(\bar{r}; \bar{a}, R_e) = k(\bar{a}, R_e) \bar{U}_s (\bar{\Omega}_s - \bar{\Omega}_{se})$	Lift Law		
Find k			
$k(\bar{a}, R_e) = g(\bar{a}) R_e^{-h(\bar{a})}$	\bar{a}	$g(\bar{a})$	$h(\bar{a})$
	0.1	809	0.604
	0.15	450	0.658

$\bar{U}_s = b(\bar{r}; \bar{a}) R_e^{m(\bar{r}; \bar{a})}$			
$\bar{U}_s = 1.1 \times 10^{-2} \exp(2.2\bar{r}) R_e^{-1.1\bar{r}+1.6}$		for $\bar{a} = 0.15$	
$\bar{U}_s = 8.3 \times 10^{-3} \exp(1.8\bar{r}) R_e^{-1.4\bar{r}+1.9}$		for $\bar{a} = 0.1$	
$\bar{\Omega}_{se} = 0.0023 R_e^{1.72}$		0.05 \leq \bar{a} \leq 0.25	
applicable to a wide range of \bar{a}			
$\bar{r}_e = f(\bar{a}) R_e^{q(\bar{a})}$	\bar{a}	$f(\bar{a})$	$q(\bar{a})$
	0.1	0.591	0.0644
	0.15	0.555	0.0546

Table E-4. Structure of the correlations for the lift law

5. Comparison of lift expressions

Wang and Joseph (2003) compared the lift correlation (4.7) with analytical lift expressions in the literature. Their comparison was limited because the correlation (4.7) is for a two-dimensional cylindrical particle whereas the lift expressions of Saffman (1965, 1968) and Auton (1987) are for a sphere. A comparison between correlations (4.5) and (4.6) with the aforementioned analytical lift expressions is more sensible; though the comparison is still tentative because the analytical lift expressions are for a particle in a linear shear flow on an unbounded domain whereas our 3D simulation is in a tube Poiseuille flow. We will compare the correlation (4.5) to the analytical lift expressions with these caveats in mind.

Auton (1987) derived a lift expression for a fixed sphere in an inviscid fluid in which uniform motion is perturbed by a weak shear:

$$\mathbf{L} = \frac{2}{3} \pi a^3 \rho \boldsymbol{\omega} \times (\mathbf{u} - \mathbf{U}). \quad (5.1)$$

In the case under consideration, $\boldsymbol{\omega} = \mathbf{e}_z \dot{\gamma}$ and $\mathbf{u} - \mathbf{U} = \mathbf{e}_x U_s$; the lift force in y direction is

$$L = \frac{2}{3} \pi a^3 \rho U_s \dot{\gamma}, \quad (5.2)$$

which is similar to our correlation (4.5) but differs from them in several ways: (5.2) has a constant prefactor for inviscid fluids whereas viscous effects enter into (4.5) through R_e ; the lift force depends on $\dot{\gamma}$ in (5.2) but on the discrepancy $\Omega_s - \Omega_{se}$ in (4.5); (5.2) is for a fixed 3D sphere while (4.5) is for a freely rotating sphere with zero acceleration.

Saffman 1965, 1968 obtained an expression for the lift force on a rotating sphere in an unbounded linear shear flow at indefinitely small Reynolds number:

$$L = 6.46 \rho_f^{0.5} \mu^{0.5} U_s \dot{\gamma}^{0.5} a^2 + \text{lower order terms} . \quad (5.3)$$

If we make following changes in equation (4.5): $R_e = \rho_f \dot{\gamma}_w (2a)^2 / \mu$, the power of R_e (-0.604) \rightarrow (-0.5), then equation (4.5) becomes:

$$L = 1696 \rho_f^{0.5} \mu^{0.5} U_s \dot{\gamma}_w^{-0.5} (\Omega_s - \Omega_{se}) a^2 . \quad (5.4)$$

Comparing (5.4) and the leading term in (5.3), we note that both expressions are linear in U_s ; both have a similar dependence on ρ_f , μ , and a . However, the dependence on $\dot{\gamma}$ and $\Omega_s - \Omega_{se}$ is greatly different.

For a neutrally buoyant particle at equilibrium, $L = 0$ and equations (5.2) and (5.3) imply $U_s = 0$. The Auton and Saffman formulas thus predict that the slip velocity is zero for a neutrally buoyant sphere at equilibrium.

McLaughlin (1991) generalized Saffman's analysis to remove the restriction that the Reynolds number \bar{U}_s based on slip velocity U_s is much smaller than the square root of the Reynolds number R_e based on the shear rate and derived an expression for the lift force:

$$L = \frac{6.46}{2.255} \rho_f^{0.5} \mu^{0.5} U_s \dot{\gamma}^{0.5} a^2 J(\varepsilon), \quad (5.5)$$

where

$$\varepsilon = \frac{\sqrt{R_e}}{\bar{U}_s}, R_e = \frac{\rho_f \dot{\gamma} (2a)^2}{\mu}, \bar{U}_s = \frac{\rho_f U_s 2a}{\mu}$$

and J is a function of ε only and has a value of 2.255 as $\varepsilon \rightarrow \infty$ (the Saffman limit). Equation (5.5) shows that zero lift force is obtained when $U_s = 0$ or $J(\varepsilon) = 0$. The solution provided by McLaughlin gives $J(\varepsilon) = 0$ at $\varepsilon = 0.215$, i.e., $\bar{U}_s = \sqrt{R_e} / 0.215$. Hence, U_s is not single valued for $L = 0$.

In the lift expressions given by Auton, Saffman, and McLaughlin, zero lift force is determined by the slip velocity U_s . This is not the case in our simulation for a sphere in tube Poiseuille flows; our results show that $\Omega_s = \Omega_{se}$ gives rise to zero lift. The difference may be due to the fact that linear shear flow has a zero shear gradient whereas the shear gradient in Poiseuille flow is a constant and not small.

6. Conclusion and discussion

- The motion of a single neutrally buoyant rigid sphere in tube Poiseuille flow is simulated by two methods: (1) an ALE arbitrary Lagrangian-Eulerian scheme with a moving adaptive mesh and (2) a DLM distributed Lagrange multiplier / fictitious domain method. The two methods give the same results, and the simulation agrees with experiments.
- A lift law $L = CU_s(\Omega_s - \Omega_{se})$ analogous to $L = \rho U \Gamma$ of classical aerodynamics which was proposed and validated in two dimensions is validated in three dimensions here; U_s is the slip velocity and it is positive, Ω_s is the slip angular velocity and Ω_{se} is the slip angular velocity when the sphere is in equilibrium at the Segré-Silberberg radius.
- The slip angular velocity discrepancy $\Omega_s - \Omega_{se}$ is the circulation for the free particle and it is shown to change sign with the lift.
- Numerical experiments using the method of constrained simulation generated data for the lift force and velocities of a freely rotating sphere in steady flows arising from initial value problems in which the sphere is constrained to move at a fixed radius.
- Constrained simulations are very efficient. The lift and all velocities are obtained for different radii at each specified Reynolds number and radius ratio $\bar{a} = a/R$.
- Equilibrium may be identified at the Segré-Silberberg radius at which the lift vanishes (for a neutrally buoyant particle). The equilibrium slip angular velocity is the slip angular velocity at this equilibrium radius.
- Data generated by constrained simulations are processed for straight lines in log-log plots and give rise to get explicit power-law formula for all the quantities in the lift law as a function of R_e and \bar{a} . We go from data to formulas.
- The equilibrium position (the Segré-Silberberg radius) moves towards the wall as R_e increases at each fixed \bar{a} ; it moves towards the centerline as \bar{a} increases at a fixed flow Reynolds number \bar{U}_m .

- Our correlations are compared with analytical lift formulas in the literature. None of the analytic formulas for lift change sign at Segré-Silberberg radius. These formulas also leave the form of the slip velocity U_s obscure.

The lift law we have proposed for free circular and spherical particles is analogous to the aerodynamic lift law $\rho U \Gamma$ in the case of a rotating circle for which $\Gamma = 2\pi a^2 \Omega$. It is probable that the lift law for free bodies of more general shape is in the form $L = C U_s \Gamma_s$ where C depends on fluid properties and geometric parameters and Γ_s is unknown. The determination of Γ even in aerodynamic theory is a complicated problem. In airfoil theory, Γ is strongly coordinated with the attack angle of the airfoil. A similar coordination of the circulation with the attack angle is apparently generated by the motion of a free ellipse in a plane Poiseuille flow (Feng, Huang and Joseph, 1995). This problem could be framed in terms of the equilibrium position and orientation of an ellipse in a plane Poiseuille flow. As in the case of circular particles, the equilibrium position is decided by a balance of buoyant weight and lift, where the lift arises as a competition of forces arising from shear gradients and wall effects. This problem ought to be studied by the technique of constrained simulation discussed here. At each fixed y , the motion of the ellipse would evolve to a steady state with a fixed angle of attack. This lift on the ellipse at this y could be computed and, of course, as in the case of circular and spherical particles, this lift would balance the buoyant weight, zero for neutrally buoyant particles, at equilibrium, with a certain equilibrium attack angle. The lift must change sign with the attack angle discrepancy.

This paper aims at presenting a general procedure and data structure for the interrogation of numerical simulation data. Our goal is to draw explicit formulas from numerical data, which may be used to model complex problems, obviating further expensive computation. The procedure involves identifying controlling dimensionless groups and data fitting analyses which lead to expressions for the quantities of interest in terms of prescribed parameters. We believe when properly used, this procedure may help to reveal the underlying physics of the problem and generate practically useful formulas at the same time.

Acknowledgement

This work was partially supported by the National Science Foundation KDI/New Computational Challenge grant (NSF/CTS-98-73236); by the DOE, Department of Basic Energy Sciences; by a grant from the Schlumberger foundation; from STIM-LAB Inc.; and by the Minnesota Supercomputer Institute.

References

- Asmolov, E. S. 1999 The inertial lift on a spherical particle in a plane Poiseuille flow at large channel Reynolds number. *J. Fluid Mech.* **381**, 63 – 87.
- Auton, T.R. 1987 The lift force on a spherical body in a rotational flow, *J. Fluid Mech.* **183**, 199 - 218.
- Bretherton, F.P. 1962 Slow viscous motion round a cylinder in a simple shear, *J. Fluid Mech.* **12**, 591 - 613.
- Choi, H.G. and Joseph, D.D. 2001 Fluidization by lift of 300 circular particles in plane Poiseuille flow by direct numerical simulation, *J. Fluid Mech.* **438**, 101 - 128.
- Feng, J., Hu, H.H. and Joseph, D.D. 1994 Direct simulation of initial value problems for the motion of solid bodies in a Newtonian fluid. Part 2: Couette and Poiseuille flows, *J. Fluid Mech.* **277**, 271 - 301.
- Feng, J., Huang, P.Y. and Joseph, D.D. 1995. Dynamic simulation of the motion of capsules in pipelines, *J. Fluid Mech.* **286**, 201-227.
- Glowinski, R. 2003 Chapters 8 and 9 of *Finite element methods for incompressible viscous flow*. In *Handbook of Numerical Analysis*, Vol. IX, P.G. Ciarlet and J.L. Lions, eds., North-Holland, Amsterdam, pp. 3-1176.
- Glowinski, R., Pan, T-W., Hesla, T.I. and Joseph, D.D. 1999 A distributed Lagrange multiplier/fictitious domain method for particulate flows. *Int. J. Multiphase Flow*, **25**, 755-794.
- Glowinski, R., Pan, T-W., Hesla, T.I, Joseph, D.D, and Periaux, J. 1999 A distributed Lagrange multiplier/fictitious domain method for flow around moving rigid bodies: Application to particulate flow, *Int. J. Numer. Meth. Fluids*, **30**, 1043-1066.
- Glowinski, R., Pan, T-W., Hesla, T.I, Joseph, D.D, and Periaux, J., 2001 A fictitious domain approach to the direct numerical simulation of incompressible fluid flow past moving rigid bodies: Application to particulate flow, *J. Comp. Phys.*, **162**, 363-426.
- Glowinski, R., Pan, T-W. and Periaux, J. 1998 Distributed Lagrange multiplier methods for incompressible viscous flow around moving rigid bodies. *Comp. Math. Appl. Mech. Eng.* **151**, 181-194.
- Goldsmith, H.L. and Mason, S.G. 1967 "Chapter 4. The Microrheology of Dispersions," in F.R. Eirich, ed., *Rheology: Theory and Applications*, Volume IV, *Academic Press*, NY, pp. 87-205.
- Hu, H.H., Joseph, D.D. and Crochet, M.J. 1992 Direct simulation of fluid particle motions. *Theor. Comput. Fluid Dyn.* **3**, 285 - 306.
- Joseph, D.D. and Ocando, D. 2002 Slip Velocity and Lift, *J. Fluid Mech.* **454**, 263 - 286.
- Karnis, A., Goldsmith, H.L. and Mason, S.G. 1966 The flow of suspensions through tubes. Part 5: Inertial effects. *Can. J. Chem. Engng.* **44**, 181.
- Matas, J. P., Morris, J. F. and Guazzelli, E. 2004 Lateral forces on a sphere. *Oil & Gas Science and Technology – Rev.* **59(1)**, 59 – 70.
- McLaughlin, J.B. 1991 Inertial migration of a small sphere in linear shear flows, *J. Fluid Mech.* **224**, 261 - 274.
- Patankar, N.A., Huang, P.Y., Ko, T. and Joseph, D.D. 2001 Lift-off of a single particle in Newtonian and viscoelastic fluids by direct numerical simulation, *J. Fluid Mech.* **438**, 67 - 100.
- Patankar, N.A., Ko, T., Choi, H.G. and Joseph, D.D. 2001 A correlation for the lift-off of many particles in plane Poiseuille of Newtonian fluids, *J. Fluid Mech.* **445**, 55 - 76.

- Rubinow, S.I. and Keller, J.B. 1961 The transverse force on a spinning sphere moving in a viscous fluid. *J. Fluid Mech.* **11**, 447 - 459.
- Saffman, P.G. 1965 The lift on a small sphere in a slow shear flow, *J. Fluid Mech.* **22**, 385 - 400; and Corrigendum, 1968 *J. Fluid Mech.* **31**, 624.
- Schonberg, J. A. & Hinch, E. J. 1989 Inertial migration of a sphere in Poiseuille flow. *J. Fluid Mech.* **203**, 517 – 524.
- Segrè G. and Silberberg, A. 1961 Radial Poiseuille flow of suspensions, *Nature*, **189**, 209.
- Segrè G. and Silberberg, A. 1962 Behavior of macroscopic rigid spheres in Poiseuille flow: Part I, *J. Fluid Mech.* **14**, 136 - 157.
- Singh, P., Joseph, D.D., Hesla, T.I., Glowinski, R. and Pan, T-W. 2000 A distributed Lagrange multiplier/fictitious domain method for viscoelastic particulate flows. *J. Non-Newtonian Fluid Mech.* **91**, 165-188.
- Wang, J. and Joseph, D.D. 2003 Lift forces on a cylindrical particle in plane Poiseuille flow of shear thinning fluids. *Physics Fluids.* **15**, 2267-2278.
- Zhu, M-Y. 2000 Direct numerical simulation of the solid-liquid flows of Newtonian and viscoelastic fluids. Ph.D. thesis, University of Pennsylvania.